N° d'ordre : 3305

THESE

En vue de l'obtention du : **DOCTORAT**

Structure de Recherche : **Equipe de Physique des Hautes Energies-Modélisation et Simulation**
Discipline : **Physique**
Spécialité : **Physique Médicale**

Présentée et soutenue le **11/03/2020** *par :*

Hicham ASMI

Single Photon Emission Computed Tomography (SPECT) imaging systems optimization in nuclear medicine: Monte Carlo study

JURY

El Hassan SAIDI,	PES, Faculté des Sciences, Université Mohammed V–Rabat	Président
Mohammed AGGOUR,	PES, Faculté des Sciences, Université Ibn Tofail-Kénitra	Rapporteur / Examinateur
Mohammed CHERRAJ,	PH, Faculté des Sciences, Université Mohammed V–Rabat	Rapporteur / Examinateur
Farida BENTAYEB,	PES, Faculté des Sciences, Université Mohammed V– Rabat	Directeur de thèse
Lalla Btissam DRISSI,	PH, Faculté des Sciences, Université Mohammed V– Rabat	Rapporteur / Examinateur

Année Universitaire : 2019-2020

Acknowledgment

This thesis took place within the Laboratory of Physics of High Energy Physics-Modeling and Simulation, Faculty of Sciences of Rabat, University Mohammed V, under the direction of Mrs. Farida BENTAYEB, Professor of Higher Education at the Faculty of Sciences of Rabat.

I would like to express my deep gratitude to my thesis director Mrs. Farida BENTAYEB, Professor of Higher Education at the Faculty of Sciences in Rabat. Thank you for his confidence, his regular follow-up, his pertinent remarks, his constructive criticisms. I also thank her for her support and the constructive contact so generous on the human level as a scientist throughout this thesis.

I extend my sincere thanks to Mr El Hassan SAIDI, Professor of Higher Education at the Faculty of Sciences, Rabat, who did me the honor of accepting the presidency of the jury.

I address my sincere thanks to Mr. Mohammed AGGOR, Professor of Higher Education at the Faculty of Sciences of Kenitra, for having accepted to judge this work as an reporter and examiner.

I warmly thank Mr. Mohammed CHERRAJ, Professor of Higher Education at the faculty of sciences of Rabat, for agreeing to judge this work as reporter and examiner.

I would like to thank especially Mrs Lalla Btissam DRISSI, Proficiency Professor at the Faculty of Sciences of Rabat, who accepted to be part of my jury as reporter and examiner.

Résumé

Les simulations de Monte Carlo sont actuellement considérées en imagerie de médecine nucléaire comme un outil pour concevoir et optimiser la caméra à scintillation et les systèmes SPECT, ainsi que pour évaluer algorithmes de reconstruction et méthodes de correction pour dégrader les effets physiques. Parmi les de nombreux simulateurs disponibles, aucun d'entre eux n'est considéré comme un standard en imagerie médicale nucléaire. Dans cette thèse, nous avons utilisé le code de simulation de Monte Carlo, SIMIND, qui décrit une caméra SPECT standard et peut facilement être modifié pour presque n'importe quel type de calcul rencontré en imagerie SPECT. SIMIND a été validé dans SPECT en modélisant des gamma caméras, en comparant les résultats obtenus avec des simulations SIMIND avec des données expérimentales. SIMIND comprend une modélisation complète des interactions des collimateurs, ce qui est essentiel lorsque des émetteurs de photons de plus haute énergie sont simulés. Notre objectif dans ce travail de thèse était d'évaluer et de déterminer les paramètres d'imagerie optimaux en imagerie SPECT, et également d'évaluer la méthode TEW, au moyen de la simulation de Monte Carlo. Une méthode largement utilisée pour la correction de la diffusion est la soustraction d'images formées à l'aide de fenêtres d'énergie dans la région des photopointes. Les paramètres utilisés pour la comparaison des différents paramètres de fenêtre et collimateurs incluent; résolution spatiale, sensibilité, contraste de l'image, rapports diffusion / total (STR). Nous avons évalué les paramètres d'imagerie pour l'I-131 en utilisant la simulation de Monte Carlo. Nous avons démontré que, dans I-131 SPECT, la diffusion et la pénétration du collimateur sont significatives et nos résultats montrent que, le petit angle d'acceptation a un effet majeur sur la qualité de l'image en imagerie I-131 SPECT. En outre, un certain nombre de paramètres de fenêtre d'énergie et de collimateur différents pour les isotopes I-131, Lu-177, Y-90 sont étudiés en utilisant des simulations de Monte Carlo avec le code SIMIND. De plus, nous évaluons les fractions de photons diffusés et déterminons les fenêtres optimales de sous-énergie et d'énergie principale pour la mise en uvre de la méthode de correction TEW en imagerie Sm-153.

Mots-clés tomographie par émission monophotonique (SPECT), imagerie nucléaire, Monte Simulation de Carlo, SIMIND, sensibilité, résolution spatiale, photon diffusé

Summary

Monte Carlo simulations are currently considered in nuclear medicine imaging as a powerful tool to design and optimize the scintillation camera and SPECT systems, and also to assess reconstruction algorithms and correction methods for degrading physical effects. Among the many simulators available, none of them is considered as a standard in nuclear medical imaging. In this thesis we have used the Monte Carlo simulation code, SIMIND, which describes a standard SPECT camera and can easily be modified for almost any type of calculation encountered in SPECT imaging. SIMIND was validated in SPECT by modeling gamma cameras, by comparing the results obtained with SIMIND simulations with experimental data. SIMIND includes complete modeling of collimator interactions, which is essential when higher energy photon emitters are simulated. Our objective in this thesis work was to evaluate and determine the optimal imaging parameters in SPECT imaging, and also evaluate of TEW method, by the means of Monte Carlo simulation. A widely used method for scatter correction is subtraction of images formed using energy windows in the region of the photopeaks. Parameters used for comparison of the different window settings and collimators include; spatial resolution, sensitivity, image contrast, scatter to total ratios (STR). We have evaluated the imaging parameters for I-131 using Monte Carlo simulation. We demonstrated that, in I-131 SPECT, the collimator scatter and penetration are significant and our results show that, the small acceptance angle has a major effect on the image quality in I-131 SPECT imaging. In addition, a number of different energy window settings and collimator for the isotopes I-131, Lu-177, Y-90 are investigated using Monte Carlo simulations with the code SIMIND. Also, we assess the scattered photon fractions and determined the optimal sub- and main-energy windows for the implementation of TEW correction method in Sm-153 imaging.

Keywords *single-photon emission computed tomography (SPECT), nuclear imaging, Monte Carlo simulation, SIMIND, sensitivity, spatial resolution, scattered photon*

Résumé détaillé

La tomodensitométrie à émission monophotonique (SPECT Scan) est une technique d'imagerie tomographique de médecine nucléaire utilisant des rayons gamma. Elle est très similaire à l'imagerie planaire de médecine nucléaire conventionnelle utilisant une caméra gamma. Cependant, il peut fournir des informations en 3D sous la forme d'images en coupe transversale du patient, par exemple l'imagerie cérébrale. Les systèmes d'imagerie informatique peuvent transformer ces informations pour produire l'image requise. Dans l'ensemble, la technique nécessite l'administration d'un radionucléide émetteur gamma au patient, normalement par injection dans la circulation sanguine. Depuis le développement de la tomodensitométrie dans les années 1970, le radioisotope de l'organe et / ou du tissu peut être cartographié par imagerie SPECT. Tous les rayonnements gamma émis par les produits radiopharmaceutiques SPECT sont détectés par l'utilisation d'une caméra gamma rotative autour du patient pour produire une imagerie 3D. Les images subissent diverses transformations électroniques en tenant compte de la distribution du radiotraceur, du processus de rétroprojection filtrée et d'autres techniques tomographiques. Les simulations de Monte Carlo sont actuellement considérées en imagerie de médecine nucléaire comme un outil puissant pour concevoir et optimiser la caméra à scintillation et les systèmes SPECT, ainsi que pour évaluer les algorithmes de reconstruction et les méthodes de correction des effets physiques dégradants. Parmi les nombreux simulateurs disponibles, aucun d'entre eux n'est considéré comme un standard en imagerie médicale nucléaire. Dans cette thèse, nous avons utilisé le code de simulation de Monte Carlo, SIMIND, qui décrit une caméra SPECT standard et peut facilement être modifié pour presque n'importe quel type de calcul rencontré en imagerie SPECT. SIMIND a été validé dans SPECT en modélisant des gamma caméras, en comparant les résultats obtenus avec des simulations SIMIND avec des données expérimentales. SIMIND comprend une modélisation complète des interactions des collimateurs, ce qui est essentiel lorsque des émetteurs de photons de plus haute énergie sont simulés. Notre objectif dans ce travail de thèse était d'évaluer et de déterminer les paramètres d'imagerie optimaux en imagerie SPECT, et également d'évaluer la méthode TEW, au moyen de la simulation de Monte Carlo. Une méthode largement utilisée pour la correction de la diffusion est la soustraction d'images formées à l'aide de fenêtres d'énergie dans la région des photopointes. Les paramètres utilisés pour la comparaison des différents paramètres de fenêtre et collimateurs incluent; résolution spatiale, sensibilité, contraste de l'image, rapports diffusion / total (STR). Nous avons évalué les paramètres d'imagerie pour l'I-131 en utilisant la simulation de Monte Carlo. Nous avons démontré que, dans I-131 SPECT, la diffusion et la pénétration du collimateur sont significatives et nos résultats montrent que, le petit angle d'acceptation a un effet majeur sur la qualité de l'image en imagerie I-131 SPECT. En outre, un certain nombre de paramètres de fenêtre d'énergie et de collimateur différents pour les isotopes I-131, Lu-177, Y-90 sont étudiés en utilisant des simulations de Monte Carlo avec le code SIMIND. De plus, nous évaluons les fractions de photons diffusés et déterminons les fenêtres

optimales de sous-énergie et d'énergie principale pour la mise en uvre de la méthode de correction TEW en imagerie Sm-153. The Monte-Carlo simulations are a widely and effective tool for different areas of diagnostic nuclear imaging, such as, the optimization of detector components (collimator, scintillator, photomultiplier ...), the design of new detectors . The method is useful for solving complex problems when experimental measurements may be impracticable. The design of SPECT and PET (Positron emission tomography) imaging systems using the Monte Carlo technique has received considerable attention, and a large number of applications were the result of such investigations. Another promising application of Monte Carlo calculations is the development and evaluation of reconstruction algorithms and correction technique for attenuation and scattered photons which degrade contrast, spatial resolution, and quantification, since with Monte Carlo Simulation, it is possible to track and record the life history of the individual photon originating from the source that ultimately deposits its complete energy inside the crystal. Therefore, unscattered and scattered photons can be tracked separately. Monte Carlo simulation thus allows a detailed evaluation of the energy and spatial distribution of scattered photon, which would be difficult to perform using experimental study . Many simulators are currently available, but none of them has yet become a standard in nuclear imaging because each has its own specificities and also its own shortcomings. In this work we use the SIMIND Monte Carlo code , which is well established for SPECT with low-energy photons. Because of the interest in simulating higher energy photon emitters, this code was recently combined with the collimator routine that accounts for scatter and penetration. The SIMIND code is designed such that the parameters to be calculated in a particular simulation can be easily changed. This is achieved through a user-written scoring subroutine that is linked to the code. A call to the routine is made at different stages during a photons history. Several scoring routines were used to generate the images and spectra that were specific to this work. In, SPECT imaging, the quantification is difficult for common nuclear medicine isotopes because of the higher energy of the photopeak and the multiple γ-ray emissions . Therefore, the inclusion of scattered photons in SPECT images degrades spatial resolution, and contrast . In the case of higher energy photon emitters such as I-131, both septal penetration and scatter in the collimator are significant . The SIMIND Monte Carlo code [5] used in this work includes complete modeling of collimator interactions, which is essential when higher energy photon emitters are simulated . Our objective in this thesis work was to evaluate and determine the optimal imaging parameters in SPECT imaging by the means of Monte Carlo simulation . Le chapitre I rappelle le principe général de l'imagerie gamma, décrivant les radiotraceurs, la chaîne de détection et les types d'acquisition de gamma caméra. Les limites du SPECT, résultant principalement de facteurs technologiques et physiques, sont enfin abordées: les phénomènes majeurs perturbant la formation d'images tels que l'atténuation et la diffusion sont décrits. Ce chapitre présente également le rayonnement électromagnétique, la spectrométrie du rayonnement électromagnétique et les méthodes de correction SPECT développées pour corriger les phénomènes de dégradation de l'image et empêcher une quantification précise et fiable des coupes reconstruites. Le chapitre II est consacré au problème de la reconstruction tomographique et décrit les principaux algorithmes de reconstruction utilisés dans SPECT. Le chapitre III rappelle les rôles principaux de la simulation de Monte Carlo en imagerie de médecine nucléaire, puis décrit le programme SIMIND Monte Carlo et les différentes étapes à suivre pour effectuer une simulation sont exposées. Dans le chapitre IV, nous évaluons les fractions de photons pénétrés et diffusés dans la fenêtre d'énergie de photopics pour l'I-131 en utilisant le code de simulation de Monte Carlo. Chapitre V Ce chapitre propose d'évaluer la distribution de dispersion du Lu-177

afin de déterminer la situation optimale pour la qualité d'image. La tomodensitométrie à émission monophotonique (SPECT Scan) est une technique d'imagerie tomographique de médecine nucléaire utilisant des rayons gamma. Elle est très similaire à l'imagerie planaire de médecine nucléaire conventionnelle utilisant une caméra gamma. Cependant, il peut fournir des informations en 3D sous la forme d'images en coupe transversale du patient, par exemple l'imagerie cérébrale. Les systèmes d'imagerie informatique peuvent transformer ces informations pour produire l'image requise. Dans l'ensemble, la technique nécessite l'administration d'un radionucléide émetteur gamma au patient, normalement par injection dans la circulation sanguine. Depuis le développement de la tomodensitométrie dans les années 1970, le radioisotope de l'organe et / ou du tissu peut être cartographié par imagerie SPECT. Tous les rayonnements gamma émis par les produits radiopharmaceutiques SPECT sont détectés par l'utilisation d'une caméra gamma rotative autour du patient pour produire une imagerie 3D. Les images subissent diverses transformations électroniques en tenant compte de la distribution du radiotraceur, du processus de rétroprojection filtrée et d'autres techniques tomographiques.

List of Figures

List of Tables

List of Abbreviations

SPECT	Single Photon Emission Computed Tomography
PET	Positron Emission Tomography
SIMIND	SIMulation of Imaging Nuclear Detectors
Lu-177	Lutetium-177
I-131	Iodine-131
TEW	Triple Energy Window
DEW	Double Energy Window
DPW	Dual Photopeak Window
MRI	Magnitic Resonanc Imagings
DS	Downscatter
FBP	Filtered backprojetion
MLEM	Maximum Likelihood Expectation-Maximization
OSEM	Ordered Subsets Expectation Maximization
MC	Monte Carlo
S/T	Scatter to Total
LEHR	Low Energy High Resolution
HE	High Energy
ME	Midium Energy
HE	High Energy
FWHM	Full width at Half Maximum
FWtM	Full width at Ten Maximum
PSF	Point Spread Function

Contents

Contents

General introduction

Nuclear medicine imaging is the use of radioactive substances in medicine for diagnose, evaluate or treat a variety of diseases. These include many types of cancers, heart disease, gastrointestinal, neurological disorders and other abnormalities. It is also used in the basic sciences, such as biology, in drug discovery and in pre-clinical medicine. Nuclear imaging is an emission imaging used in nuclear medicine for diagnostic purposes. In single photon emission computed tomography or less commonly, (SPECT), the patient is administered with a radiotracer which emits radiation in the form of gamma rays or X-rays, which are detected by a gamma camera. The most common radiotracer is technetium, which emits gamma photons of energy 140 keV. In clinical routine, the gamma cameras used are still based on the principle of gamma cameras developed by H. Anger in the 1960s. These cameras consist of one or more detection heads, and each detection head is composed of a conventional collimation system and a scintillator-based detection module. They make it possible to obtain the images, called scintigraphic images, in planar acquisition or in tomographic acquisition [1].

SPECT imaging is performed by using a gamma camera to acquire multiple two dimensional images, from multiple angles. Then, a tomographic reconstruction algorithm is applied to the multiple projections, yielding a three dimensional data set. Precise measurement of radioactivity contained in reconstructed images, called quantification, is affected by many phenomena during the formation of images that alter the information extracted from these images. Nuclear imaging provides non-invasive access to information about the functioning of organs and to study physiological and metabolic processes. The reliability of the quantification of the images obtained is affected both by the limits of the performance of the collimators and detectors (spatial and energy resolution, sensitivity, septal penetration ...), by physical effects such as diffusion and attenuation, which disturb the reconstruction of images, by physiological effects (movements of the patient) and effects related to tomographic reconstruction. These effects must therefore be corrected by specific correction methods in order to extract reliable quantitative parameters. The most commonly used in clinical routine collimator is a parallel hole collimator. Its dimensioning is optimized to ensure the best compromise between the spatial resolution and the efficiency of the camera. However, this compromise may limit the quality of the scintigraphic images, thus making the diagnostic interpretation of the images difficult. The Monte-Carlo simulations are a widely and effective tool for different areas of diagnostic nuclear imaging, such as, the optimization of detector components (collimator, scintillator, photomultiplier ...), the design of new detectors . The method is useful for solving complex problems when experimental measurements may be impracticable [2]. The design of SPECT and PET (Positron emission tomography) imaging systems using the Monte Carlo technique has received considerable attention, and a large number of applications were the result of such investigations. Another promising application of Monte Carlo calculations is the development and evaluation of reconstruction algorithms and correction technique for attenuation

and scattered photons which degrade contrast, spatial resolution, and quantification, since with Monte Carlo Simulation, it is possible to track and record the life history of the individual photon originating from the source that ultimately deposits its complete energy inside the crystal. Therefore, unscattered and scattered photons can be tracked separately. Monte Carlo simulation thus allows a detailed evaluation of the energy and spatial distribution of scattered photon, which would be difficult to perform using experimental study . Many simulators are currently available, but none of them has yet become a standard in nuclear imaging because each has its own specificities and also its own shortcomings. In this work we use the SIMIND Monte Carlo code , which is well established for SPECT with low-energy photons. Because of the interest in simulating higher energy photon emitters, this code was recently combined with the collimator routine that accounts for scatter and penetration. The SIMIND code is designed such that the parameters to be calculated in a particular simulation can be easily changed. This is achieved through a user-written scoring subroutine that is linked to the code. A call to the routine is made at different stages during a photons history. Several scoring routines were used to generate the images and spectra that were specific to this work. In, SPECT imaging, the quantification is difficult for common nuclear medicine isotopes because of the higher energy of the photopeak and the multiple γ-ray emissions [3]. Therefore, the inclusion of scattered photons in SPECT images degrades spatial resolution, and contrast . In the case of higher energy photon emitters such as I-131, both septal penetration and scatter in the collimator are significant [4]. The SIMIND Monte Carlo code [5] used in this work includes complete modeling of collimator interactions, which is essential when higher energy photon emitters are simulated . Our objective in this thesis work was to evaluate and determine the optimal imaging parameters in SPECT imaging by the means of Monte Carlo simulation [6, 12]. Chapter I recalls the general principle of gamma imaging, describing the radiotracers, the detection chain, and the types of acquisition of gamma camera. The limits of the SPECT, resulting mainly from technological and physical factors, are finally addressed: the major phenomena disrupting the formation of images such as attenuation and diffusion are described. Also this chapter presents the electromagnetic radiation, spectrometry of electromagnetic radiation and SPECT correction methods developed to correct image-degrading phenomena and prevent precise and reliable quantification of reconstructed sections. Chapter II is devoted to the problem of tomographic reconstruction and describes the main reconstruction algorithms used in SPECT. Chapter III recalls the principles roles of Monte Carlo simulation in nuclear medicine imaging and then describes the SIMIND Monte Carlo program and the different steps to follow to perform a simulation are exposed. Chapter IV we evaluate the penetrated and the scattered photon fractions in the photopeak energy window for I-131 using Monte Carlo Simulation code. Chapter V this chapter proposes to evaluate the scatter distribution for Lu-177 in order to determine the optimal situation for image quality.

Chapter 1

Single Photon Emission Computed Tomography

Single-photon emission computed tomography (SPECT Scan) is a nuclear medicine tomographic imaging technique using gamma rays. It is very similar to conventional nuclear medicine planar imaging using a gamma camera. However, it can provide 3-D information in the form of cross-sectional slice images of the patient for example brain imaging. Computer imaging systems can transform this information to produce the required image. The technique overall requires delivery of a gamma-emitting radionuclide into the patient, normally through injection into the bloodstream. Since the development of computed tomography in the 1970s, the radioisotope in the organ and/or tissue can be mapped by SPECT imaging. All gamma radiation emitted from SPECT radiopharmaceuticals are detected by the usage of a rotating gamma camera around the patient to produce 3-D imaging. The images undergo various electronic transformations by taking into account the distribution of the radiotracer, the process of filtered back projection and other tomographic techniques.

The radioisotopes used in SPECT scanning have relatively long half-lives, for example, technetium-99m ($t_{1/2}$= 6 hours), indium-111 ($t_{1/2}$ days), iodine-123 ($t_{1/2}$= 13.22 hours) and thallium-201 ($t_{1/2}$ = 73 hours). The radionuclide technetium-99m prepared from molybdenum-99 by using the technetium-99m generator and used for a variety of nuclear medicine diagnostic procedures. These technetium-99m based imaging agents are relatively cheap compared to PET and MRI imaging. The problem with SPECT scanning is the absence of good spatial resolution.

1.1   Radiotracers

The Radiotracers, or radiopharmaceuticals, are radioisotopes bound to vector molecules able to target specific organs, tissues or cells within the human body. These radioactive drugs can be used for the diagnosis and for the therapy of diseases. The vector molecule is localized on the structures that interest us. Radioisotopes are atoms whose nucleus is unstable and therefore radioactive. It chosen according to its chemical properties: its addition on a vector molecule must not modify the properties of this molecule and the link between marker and carrier molecule must be strong to prevent the marker from becoming detached. It may also comprise only the radioisotope itself if it shows suitable biological properties. The radioactive isotope is also selected according to the following physical characteristics: - the nature of its radiation: gamma-emitting radioisotopes are favored because they lend themselves to external detection

and minimize the radiation dose to the patient. These gamma rays must have enough energy to get out of the body and low enough to allow effective detection by the detector. -the physical half-life of the isotope must be long enough to allow the physiological process to be followed, and sufficiently short for avoid unnecessary irradiation; Radiopharmaceuticals are used to produce images of organs of interest, a process that is called scintigraphy. A type of medical device known as gamma camera is able to detect the gamma rays or x-rays emitted by the radioisotope. They are used for flow visualisation through different technologies, such as Single Photon Emission Computed Tomography (SPECT), Positon Emission Tomography (PET). The most widely used radioisotope in diagnostic nuclear medicine is technetium-99m. Since it has almost ideal physical characteristics (half-life of 6 hours, average gamma energy of 14.5keV (very good for crossing tissues and very good for easy detection), abundance of photons gamma (98%) make it possible to minimize the dose delivered to the patient. Tc-99m can be attached to several specific molecules, allowing the diagnosis of many diseases, including certain types of cancers. Tc-99m-MDP (methylene diphosphonate) is widely used to detect bone metastasis associated with cancer [13]. Tc-99m is produced from the decay of its radioactive precursor, molybdenum 99 (Mo-99) and can be delivered on demand from a portable generator, making it very easy to access clinically and inexpensively. These advantages have made Tc-99m the most commonly used radionuclide for SPECT imaging. Other radioisotopes are also frequently used, among which I-123(Iodine), I-131(Iodine), In-111 (Indium), Ga-67(Gallium), Tl-201 (Thallium), Sm-153 (Samarium), Lu-177 and Lu-177(Lutetium). The physical characteristics of these radioisotopes, as well as their mode of production, are recalled in Table 1.

Isotopes	Gamma emission energy(keV)	Physical period	Production mode	Application
Tc-99m	140,5(90%)	6.02h	IT	
I-123	159	13h	PBR : Te-124(p,2n) → I-123 : I- 127(p,5n) Xe-123 → I-123	The metabolism of the thyroid
I-131	364	8.05d	NF	-
In-111	171, 245	67.9h	PBR: Cd-112(p,2n) →In-111	Imaging the production, migration and reabsorption of cerebrospinal fluid.
Ga-67	93, 184, 300	78.3h	PBR: Zn-68(p,2n) →Ga-67	Image the function of the bone marrow
Tl-201	63, 80.3	73h	PBR: Tl-203 (p,3n)Pb-201→Tl-201	Evaluate myocardial blood perfusion
Sm-153	103	46.7h	NC: Sm-152+n→ Sm-153 + γ	Treatment of bone metastases
Lu-177	113 (6.4%) 208 (11.0%)	6.647 d	NBR: Lu-176(n,γ) → Lu-177	Treatment of neuroendocrine tumors and prostate cancer

Table 1.1: Properties and production of the main isotopes used in SPECT.

The radioisotope is often administered intravenously, sometimes by inhalation to study pulmonary ventilation. It can be administered in a suitable chemical form (eg 131I administered

in the form of 131 I a sodium iodide) or in combination with a molecule: many molecules can be labeled, including the substrates of a metabolic pathway, antibodies, hormones , peptides, drugs, groups of molecules.

1.2   Gamma camera

The gamma camera (Figure 1.1) [14], also called a scintillation camera or Anger camera, was invented by the American physicist Hal Oscar Anger in 1957. Then, it widely imposed and has been marketed and used in clinical routine from the 60s. The camera gamma itself does not emit any radiation, but it detects radioactive energy that is emitted from a radiotracer distributed in the body and converts it into an image, a technique known as scintigraphy. The role of the scintigraphy is to visualize and analyze images of the human body or the distribution of injected, inhaled or ingested medical radionuclide, emitting gamma- or x-rays. The camera consists of a lead collimator that allows photons traveling in given directions to pass through a large diameter scintillator (commonly NaI(Tl) scintillation crystal) that converts the energy of γ-ray or x-rays photons to burst of light which is in turn converted to electric signals by detectors (photomultiplier tubes) located behind the crystal. Electrical output from detectors is fed to computer to produce information about the position at which a photon interacts with the crystal. The gamma camera produces a 2D image of the 3D representation of activity distribution within the patient's body. The modern gamma camera is under computer, allowing the physician to select the study the number of counts to be acquired, control the detector and patient bed positions and whole body procedures, and visualize the image. A gamma camera consists of one or more detection heads, which are encased in metal and plastic, an analog circuit providing the location of the gamma photons in the crystal and performing spectrometry, and processors ensuring the acquisition of data, storage and their treatment: online corrections, reconstruction, manipulation and display of images. The detection head is protected by a lead shielding of sufficient thickness to minimize the background noise introduced by the radioactive sources outside the field of view of the camera. The patient lies on the examination table which slides in between two parallel gamma camera heads that are positioned above the patient. The individual elements of the gamma camera will now be considered in more detail.

A gamma camera consists of one or more detection heads, which are encased in metal and plastic, an analog circuit providing the location of the gamma photons in the crystal and performing spectrometry, and processors ensuring the acquisition of data, storage and their treatment: online corrections, reconstruction, manipulation and display of images. The detection head is protected by a lead shielding of sufficient thickness to minimize the background noise introduced by the radioactive sources outside the field of view of the camera. The patient lies on the examination table which slides in between two parallel gamma camera heads that are positioned above the patient. The individual elements of the gamma camera will now be considered in more detail.

1.2.1   Collimator

A collimator is a thick plate made of a material with a high atomic number (lead, tungsten, etc.) that is highly absorbent for photons and has cylindrical or conical holes, with a circular or hexagonal section, in a system of axes determined. Only photons whose path does follow these

Figure 1.1: Siemens Symbia T2 SPECT CT gamma camera

directions will pass into the crystal. Therefore, the collimator determines the direction of the projection. Thus an image is formed by excluding all gamma rays except the small number traveling in the preferred direction perpendicular to the detector. The scintigraphic image obtained after the collimator corresponds to the projection of the distribution of the radioactivity on the detector crystal. The thickness separating two adjacent holes is called septum (plural septa). The lead thickness is calculated to result in attenuation of at least 95% of the photons crossing the septa. There are four basic collimator types namely parallel hole, pinhole, diverging and converging. The most common type, the parallel hole collimator, is shown in Figure. It consists of a lead plate through which runs an array of small holes whose axes are perpendicular to the face of the collimator and parallel to each other. This kind of collimator keeps the same size as the source distribution onto the detector. The geometrical parameters (length and diameter of the holes, thickness of the septa, etc.) of a collimator with parallel holes vary according to the energy of the isotope used and the examinations to be carried out. Other collimators are also used in specific cases: this is the case of the pinhole collimator, consisting of a single aperture of 3 to 5 mm in diameter located at the end of a conical lead shield for imaging organs small and superficial (thyroid gland, joints, ...), or divergent / converging collimators for whole body imaging or imaging of organs of average size.

The gamma camera can detect four kinds of events which are: - True event: a photon is emitted parallel to the collimator holes, passes through a hole and interacts with the crystal, depositing all of its energy at a single location. - Detector scatter event: a photon is emitted parallel to the collimator holes, passes through a hole and interacts by Compton scattering with the crystal, depositing only part of its energy. - Object scatter event: a photon is not emitted toward the collimator holes but scattered by the patient body and passes through a collimator hole and subsequently is detected. - Septal penetration: in this case a γ ray is emitted toward the collimator, but not in parallel to it. Causing blurring of the image. The main parameters describing collimator performance are spatial resolution and sensitivity. Parallel geometry is the simplest from the point of view of reconstruction. The collimator defines the geometric
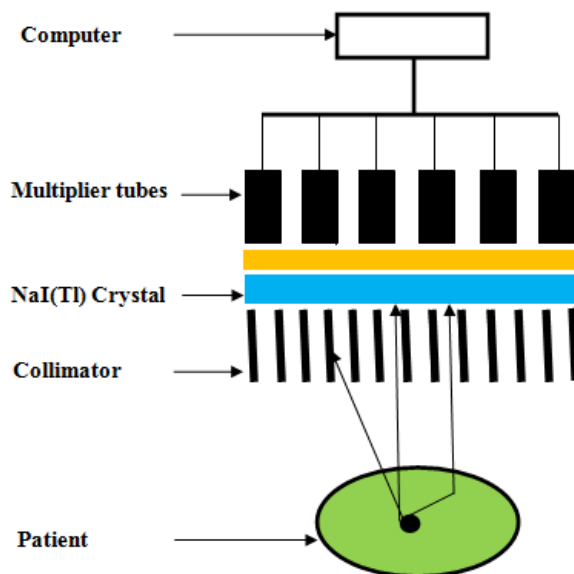
Figure 1.2: Different elements composing a gamma-camera detection head

field of view of the gamma camera and it is this which substantially determines the spatial resolution and sensitivity of the detection system.

1.2.2   The scintillating crystal

After the photons have travelled through the collimator, they interact with the cameras scintillation crystals which represent the detector part from the camera. The crystal convert energy deposited by energetic particles (charged, gamma or X photons) into light scintillation. The scintillator must have high stopping power for photons, hence the choice of dense crystals with a high atomic number, which improves the efficiency of the detector. Indeed, when a photon interacts in the scintillating crystal by a Compton effect or a photoelectric effect, it gives him a part or all its energy respectively. Most SPECT systems are equipped with sodium iodide crystal doped with thallium NaI(Tl). Its effectiveness at stopping the photons depends not only on its density but also on the thickness of crystal used. The choice of crystal thickness is a compromise between the detection efficiency and the spatial resolution which degrades when the crystal becomes thicker. The thickness of the NaI (Tl) is typically between 6 and 10 mm for the SPECT systems and can reach up to 25.4 mm in order to be able to stop the higher energy photons. Its effectiveness at stopping the gammas depends not only on its density but also on the thickness of crystal used Thallium-doped Sodium Iodide produces one of the highest signals in a PMT per amount of radiation absorbed. Under optimum conditions, an average of 10000 photoelectrons is produced per MeV gamma rays. Scintillation crystals convert the gamma rays or x-rays to visible light, which is then directed through a light guide to a photomultiplier tube. A scintillating crystal must have high intrinsic efficiency, good intrinsic spatial resolution, and good energy resolution. The spatial resolution and the energy resolution strongly depend on the magnitude of the scintillation generated at each detected event. Scintillators have the advantage of having a high intrinsic efficiency and a reasonable manufacturing cost. In addition, they are available in many forms and sizes. The disadvantage of scintillating crystals lies in their need
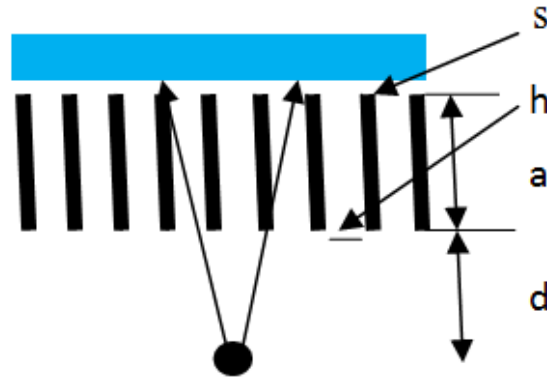
Figure 1.3: Different types of collimator and their corresponding geometries: (a) parallel hole collimator, (b) fan-beam collimator, (c) pin-hole collimator.

for a photon light converter into an electrical pulse.

Only a small fraction of the energy lost by a photons ray is converted into light, typically 10%, producing about 3000 light photons at a wavelength of 410 nm for each 100 keV of gamma ray energy absorbed, this wavelength, matches quite closely that required by the PMT. This causes information loss (light photons) at the interface between the crystal and the converter (PMT), which limit the energy resolution of the detector. The length of each scintillation must be short to avoid the overlap of light from consecutive scintillations. NaI(Tl) suffers from the drawbacks of being expensive to produce as a large crystal, fragile and so needing protection from both thermal and mechanical stresses, and hygroscopic, requiring to be canned to prevent contact with moisture. The intrinsic spatial resolution and mean energy resolution as well as the hygroscopic nature of NaI (Tl) prompted researchers to develop other inorganic scintillators. Unfortunately, only a small fraction of the energy lost by a gamma ray is converted into light, typically 10%, producing about 3000 light photons at a wavelength of 410 nm for each 100 keV of gamma ray energy absorbed. This wavelength, however, matches quite closely that required by the PMT. The length of each scintillation must be sufficiently short to avoid the overlap of light from consecutive scintillations. In the NaI(Tl) crystal it takes about 0.8μ s to collect most of the light, and this will obviously affect the maximum gamma ray rate that the camera can handle without producing a distorted image . NaI(Tl) also suffers from the drawbacks of being expensive to produce as a large crystal, fragile and so needing protection from both thermal and mechanical stresses, and hygroscopic, requiring to be canned to prevent contact with moisture. The latter requirement poses a problem since it is also necessary to ensure that the light emitted in the scintillation is transmitted to the second part of the detector system, the PMT array. While the front face and sides of the crystal are canned, usually with aluminum sufficiently thin so as not to attenuate the incoming gamma rays unduly, the rear crystal surface needs a transparent interface between the crystal and PMTs. This is usually provided by a Pyrex optical plate or light guide a few centimeters in thickness. Despite the obvious problems with using NaI(Tl), it has proved to be the only satisfactory scintillation material for gamma cameras. While it is possible, at least in theory, to produce an image from the scintillation in the crystal, the main advantage of first converting this image to electrical signals is that pulse height analysis can be used to reduce the effect of scattered photons on image quality.

The light yield yield of NaI(Tl) is $(39\pm1)10^3$ photons per MeV. Because there is an overlap in both sensitive frequency regions this setup has a high scintillation conversion efficiency. The electric field between the cathode and the first dynode accelerates the electron to create a small electron avalanche. CsI (Tl) is for example less hygroscopic than NaI (Tl), but also less efficient with PMTs, even if the number of scintillations is 18% higher than that of NaI (Tl). On the other hand, the detection of the light photons generated by the CsI (Tl) is more efficient by replacing the PMTs by photodiodes. CsI (Na) has the same characteristics as CsI (T1) with scintillation better adapted to PMTs. LaBr3 has attracted PET attention as a potential scintillator, but its properties are also attractive for SPECT. Its light response is very fast and its energy resolution (<6% at 140 keV) is much better than that of NaI (Tl) (10% at 140 keV). Recently, LaBr3 has also been used as a detector in small animal SPECT systems. Table 1 shows three clinically used scintillating crystals and their main properties. Having effective atomic numbers and comparable densities, these four crystals will have almost similar efficiency values. It has a good luminous efficiency: 13% of the energy deposited is reemitted in the form of fluorescence photons of energy 3 eV (430 nm). It is transparent to its own scintillation light, which prevents scintillation losses by self-absorption. Its time constant of 230 ns allows it to record several tens of thousands of hits per second, thus allowing a high counting rate. Its main disadvantage is its hygroscopic (moisture sensitive) character and therefore requires hermetic isolation (e.g., Al2O3 layer, epoxy, etc.).

Desirable properties of the scintillation crystal - High efficiency for stopping gamma rays
- Stopping should be without scatter
- High conversion of gamma ray energy into light
- Wavelength of light should match response of the PMTs
- Crystal should be transparent to emitted light
- Crystal should be mechanically robust
- Length of scintillation should be short

Scintillator	Effective atomic number Z	Density (g/cm3)	decay time (ns)	Wave length (nm)
NaI(Tl)	50	3.67	200	415
CsI(Tl)	54	4.5	1000	550
Cs(Na)	54	4.51	630	420
LaBr3:Ce	47	5.3	25	360

Table 1.2: Properties of the main scintillators used in SPECT

1.2.3   The light guide

The role of the light guide is to direct the light to each PMT to increase the efficiency of the light collection and imaging. It is made of a material with a refractive index close to that of the scintillating crystal, so as to optimize the transport of light towards PMs. The shape of the light guide is carefully adapted to that of the photocathode of the PM. The light guide also helps to reduce PM light collection efficiency variations: the light loss caused by dead spaces that do not cover the entry face of the PM is reduced by the light guide, which collects the light

emitted in these dead spaces and directs it to the photocathode of the PM. In gamma cameras, the light guide has significantly contributed to improving the linearity of the detection response, to the detriment of the intrinsic spatial resolution. Currently, the available PMs provide optimal coverage of the crystal surface (thus reducing dead space) and the light guide is being replaced more and more by automatic uniformity correction methods.

1.2.4   Photomultiplier tubes (PMTs)

Scintillations produced in the crystal are detected by a large number of PM tubes which are arranged in a two-dimensional array. The number of PMs placed on the surface of the crystal can vary between 37 and 91 PMTs in modern gamma cameras. The PMTs are usually arranged in a close packed array to ensure that the smallest possible gaps are left between tubes. PMTs typically have a circular section with a diameter of 5 cm and are placed in a pattern hexagonal.
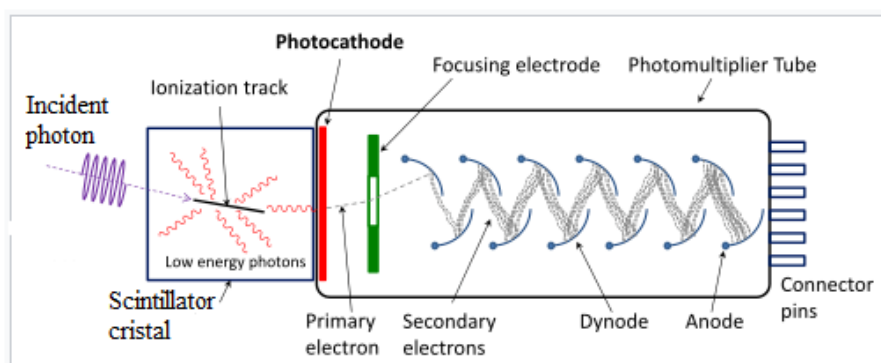
Figure 1.4: Schematic of a photomultiplier tube coupled to a scintillator.

The role of PMs is to convert visible light from scintillation into the crystal into an electrical signal that can be used by electrical circuits. PM is a vacuum tube with a photocathode and anode, between which are dynodes, which are intermediate potential electrodes. When a light photon reaches the photocathode, a photoelectric effect will take place and an electron will be ejected from it. With electrodes set to a certain potential, field lines are created, and the electrons coming out of the photocathode will follow these field lines to finish on the first dynode. They arrive there with a kinetic energy which allows them to tear out secondary electrons. These electrons are in turn accelerated to the next dynode by increasing potential difference and will in turn tear off other electrons. The process continues until the last dynode. The electrons will eventually be collected at the anode and give a measurable electrical signal at the output. The PMT not only converts light into an electronic signal but also, magnifies the electronic signal to give a sufficiently large current for the subsequent electronics. PMTs Conversion efficiency is a function of the wavelength of Incident light. The PM amplification factor can be up to 106. Even with this signal amplification pre-amplifiers built into the PMTs are necessary to ensure a sufficient signal-to-noise ratio. The PMTs produce a signal that is proportional to the light generated in the crystal. The PMTs will direct the signal to the system electronics. The signal is transferred electronically to a position circuit. The more modern gamma cameras operate through an Analog-to-Digital Converter system. This means that the PMTs output is directly digitalized through the system. These systems are able to extract the

position and energy data simultaneously. Positional information can be obtained by comparing the size of the signals from different PMTs, whereas the energy information is related to the sum of the PMTs signals. The final step to the image acquisition process comes once the images are generated on a computer monitor where they can be constructed and altered.

1.2.5   Positioning Circuit

The analog electronic circuit makes it possible to determine the location of the point of interaction of the photon in the crystal and the value of the energy of the photon. For this, the circuit analog consists of a network of four resistors by PMT. The study of the electrical signals at the terminals of each resistance of all PMTs makes it possible to calculate by barycentric weighting the location of the interaction point and the energy of the photon.

The signals of the resistors provide positioning along the X (X^+ and X^-) axis and the positioning along the Y (Y^+ and Y^-) axis, but also the energy of the E photon (corresponding to the sum of the signals of all PMTs). The total sum of the voltages (marked σ in the figure) from each photomultiplier, measured by a pulse height analyzer (PHA) is proportional to the energy of the gamma ray interaction, thus allowing discrimination between different isotopes or between scattered and direct photons.

The total sum of the voltages (marked σ in the figure) from each photomultiplier, measured by a pulse height analyzer (PHA) is proportional to the energy of the gamma ray interaction, thus allowing discrimination between different isotopes or between scattered and direct photons.

The amount of energy deposited by the photon during its interaction in the crystal is proportional to the amount of light emitted during the interaction, equal to the sum of the signals Z of all the PM

$$Z = X^+ + X^- + Y^+ + Y^- \tag{1.1}$$

The interaction point (X, Y) will be given by:

$$X = X^+ + X^- \tag{1.2}$$

$$Y = Y^+ + Y^- \tag{1.3}$$

In order for the X and Y interaction coordinates to be independent of the emission energy of the radioisotope used, the raw values of the X and Y coordinates are normalized to the total energy of the event being processed.

$$X = \frac{X^+ + X^-}{X^+ - X^-} \tag{1.4}$$

$$Y = \frac{Y^+ + Y^-}{Y^+ - Y^-} \tag{1.5}$$

Thus, during an acquisition, all the interactions are listed according to their position X ($\pm\Delta$ X).) and Y ($\pm\Delta$ Y) and their energy E ($\pm\Delta$ E). The scintigraphic image then corresponds to the visualization of the number of interactions in each position and whose energy is included in a window in energy, for example between two energies: $E_0 - \Delta E_0$ and $E_0 + \Delta E_0$,

where E_0 is energy of the photon radioisotope study (typically, 140 keV of 99mTc) and ΔE_0 is the half-height width of the energy response for E_0 energy
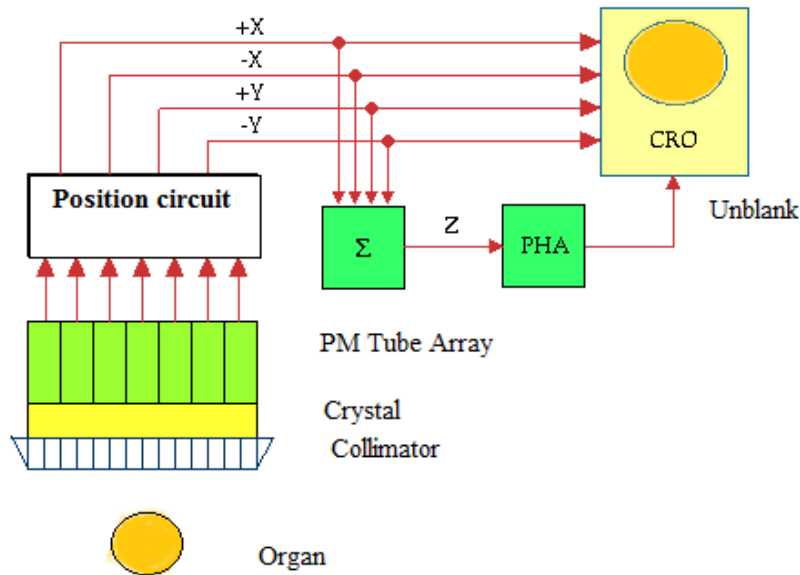
Figure 1.5: Position circuit

This voltage pulse is commonly called the Z-pulse which, following pulse height analysis, (PHA) is fed as the unblank pulse to the CRO. So we end up with four position signals and an unblank pulse sent to the CRO. The core of a CRO consists of an evacuated tube with an electron gun at one end and a phosphor-coated screen at the other end. The electron gun generates an electron beam which is directed at the screen and the screen emits light at those points struck by the electron beam. The position of the electron beam can be controlled by vertical and horizontal deflection plates and with the appropriate voltages fed to these plates the electron beam can be positioned at any point on the screen. The normal mode of operation of an oscilloscope is for the electron beam to remain switched on. In the case of the gamma camera the electron beam of the CRO is normally switched off - it is said to be blanked. When an unblank pulse is generated by the PHA circuit the electron beam of the CRO is switched on for a brief period of time so as to display a flash of light on the screen. In other words the voltage pulse from the PHA circuit is used to unblank the electron beam of the CRO. So where does this flash of light occur on the screen of the CRO? The position of the flash of light is dictated by the $\pm X$ and $\pm Y$ signals generated by the position circuit. These signals as you might have guessed are fed to the deflection plates of the CRO so as to cause the unblanked electron beam to strike the screen at a point related to where the scintillation was originally produced in the NaI(Tl) crystal. The gamma camera can therefore be considered to be a sophisticated arrangement of electronic circuits used to translate the position of a flash of light in a scintillation crystal to a flash of light at a related point on the screen of an oscilloscope. In addition the use of a pulse height analyser in the circuitry allows us to translate the scintillations related only to photoelectric events in the crystal by rejecting all voltage pulses except those occurring within the photopeak of the gamma-ray energy spectrum.

1.3   Performance of a gamma-camera

The performances of a gamma camera are characterized by several parameters: spatial resolution, energy resolution, sensitivity, uniformity and linearity. Each of these parameters depends on the characteristics of the different components of the detection head and is very often correlated. An inherent trade-off in the design of SPECT collimators are resolution vs sensitivity. It is possible to improve the spatial resolution of a collimator by further restricting the range of incident angles, but this is at the expense of reducing sensitivity. Anger cameras require collimators to localize the site within the patient from which the gamma ray photons are emitted. Because of this resolution vs sensitivity trade-off, the collimator is perhaps the most significant component of the SPECT camera affecting image quality.

   - **Parallel-hole collimators** In single photon emission computed tomography (SPECT), the type of collimator to use for a given imaging application depends mainly on the size of the FOV, the size of the detector and the required spatial resolution and/or sensitivity
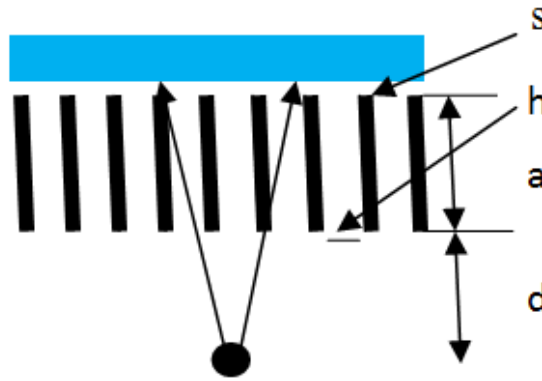
Figure 1.6: Parameters of a parallel collimator

1.3.1   Spatial resolution

Spatial resolution quantifies the size of the smallest object that can be resolved reliably, and is is measured by the FWHM (Full Width at Half Maximum) of the point spread function (PSF) or linear, obtained by making the image of a point source or linear source respectively.

   The total resolution R of the gamma-camera is the result of the contribution of the intrinsic spatial resolution RI and the spatial resolution of the collimator RC to the collimator-source distance: The intrinsic spatial resolution Ri is typically 3.5-4.0 mm for Tc-99m and is related to the characteristics of the crystal and the position logic circuitry used to compute the location of the detected photon. The spatial resolution is affected by the collimator. For a high resolution, the spatial resolution is approximately 10 mm for a Tc-99m point source located at 10 cm from the collimator face. The resolution varies for different collimators depending the on the geometry of the collimator. Collimators with smaller and longer holes will have better spatial resolution but will have lower sensitivity. A parallel-hole collimator with hexagonal holes and
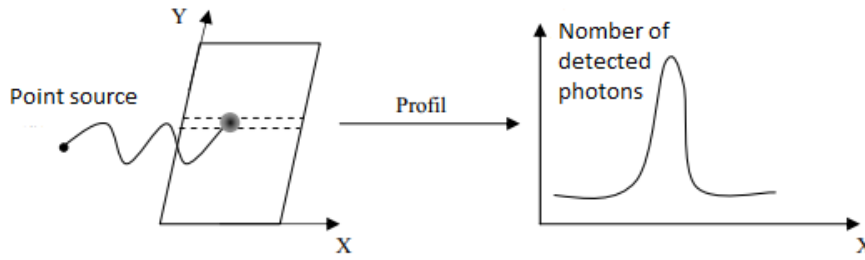
Figure 1.7: Measurement of the spatial resolution of a gamma camera, given by the width at half maximum of the point spread function.

a perfectly absorbing detector has a point-source and a geometric spatial resolution [15]:

$$R_{ph} = d\frac{a + h}{a_e} \tag{1.6}$$

Where d is the hole diameter (at-to-at distance), and h is the perpendicular distance from the point source to the detector. $a_e = -\frac{2}{\mu}$ is the physical hole length a (collimator thickness) approximately adjusted for penetration effects. μ is the attenuation coefficient $\frac{1}{\mu} = 0.37mm$ for Tc99m and lead. The collimator resolution expression do not include the mean interaction depth in the detector, which is generally much smaller than the distance from the source to the collimator surface and the collimator thickness. Spatial resolution is an important system property and is commonly quantified from the full-width-at-half-maximum (FWHM) of the point spread function (PSF), which is determined by the detector intrinsic resolution and the geometrical resolution of the collimator. The system resolution is:

$$R = \sqrt{R_i^2 + R_{ph}^2} \tag{1.7}$$

As shown in equation (1), the spatial resolution of the collimator increases as the source-collimator distance increases. This same equation shows that, we can improve the spatial resolution by increasing the length of the holes and the number of holes per unit area, or minimizing the distance between the source and the surface of the collimator. However, improving the spatial resolution by modifying the geometric parameters of the collimator leads to degrade the sensitivity of the gamma-camera. The choice of the collimator will therefore be based on the energy of the radioisotope used and considering an acceptable compromise between spatial resolution and sensitivity.

1.3.2   The count rate

When the count rate is very high, two events too close together can give rise to only one pulse at the level of the electronic detection circuit. The apparent energy can then exceed the limits imposed by the spectrometric window, in which case the pulse is rejected. Other phenomena can also appear, such as the simultaneous detection of two Compton events whose sum of deposited energies is sufficient for the detector to consider the two detected Compton events as a single event belonging to the photopic window. In SPECT, a compromise is usually sought

by administering an activity such that the counting rate does not give rise to a loss of more than 20% on the detection of the activity. This potential loss would be related to the timeout.

1.3.3   Sensitivity

Another important system property is sensitivity, which is expressed by the ratio of the number of photons per second detected and accepted through the energy window to the total number of photons emitted by the radioactive source at the solid angle seen by the detector, i.e. in cps/MBq. This value depends mainly on on the type of collimator, the radionuclide used, the light output of the crystal and width and position of the energy window. The sensitivity depends mainly on the type of collimator used and the light output of the crystal [16]. It is given by

$$S_{ph} = \frac{\sqrt{3}}{8\pi a_e^2 (d+t)^2} d^4 \qquad (1.8)$$

The equation shows that the sensitivity for a parallel hole collimator is independent of the distance between the source and the surface of the collimator. While, resolution depends on the distance h. The sensitivity of a gamma-camera with parallel holes is typically of the order of 0.01% [Madsen, 2007]. This value can be increased, without degradation of the spatial resolution, by using several detection heads. In single photon emission computed tomography (SPECT), every study on collimator utilizations show that resolution may be advantageous to small lesion oncology SPECT imaging, while high-sensitivity is generally considered to be more important than resolution in the cardiac SPECT imaging

1.3.4   Energy resolution

Image quality is affected by energy resolution which reflects the accuracy with which the gamma camera is able to determine the energy of a detected photon. Ideally, images would be comprised of only primary photons emitted by the decay of a radionuclide, not the scattered photons. The better the energy resolution result of the discrimination of primary from scattered photons, and thus, the better the image contrast, resolution and the more accurate activity quantification and distribution of the radionuclide in organ. For most modem Anger cameras, the energy resolution is expected to be 9-10% for the 140-keV photons from Tc-99m, and 15-17% for the 72-keV photons from Tl-201[]. The inaccurate measurement of energy comes from statistical fluctuations in the number of optical photons emitted by scintillation, quantum yield in photo-cathodes, gain in photomultiplier tubes, and acquisition electronics. The energy resolution is determined by the half width at half maximum FWHM (E) of the energy response of the gamma-camera for the emission energy E of the radioisotope used and is expressed in%:

$$FWHM(E) = \frac{\Delta E}{E} \times 100 \qquad (1.9)$$

The scatter photons at a low angle retain much of their initial energy. Thus, this photons can be detected in the conventional acquisition window, which is centered on the emission energy of the radionuclide having a width of 20% thereof. For example, a 140 keV photon, emitted by 99mTc, loses only 14 keV of its energy when it undergoes a Compton scattering effect at 52deg and will therefore be counted in the photopic window (140 14 keV) as a photon primary.

At 140 keV, emission energy of 99mTc, the energy resolution is typically 10% for current cameras. A standard energy window of 20% centered around the 140 keV energy peak of the emitted photons is used for Tc-99m. The greater width and smallest energy and the Tl-201 photo-peak require a wider energy window. An energy window setting of 30% is appropriate for the 70 keV peak of Tl-201, and a 15% energy window is appropriate for the 167-keV peak.

1.3.5 Spatial linearity

The spatial linearity which characterizes the geometric distortions or localization defects observed between the measured position of the photons and their real position in the input plane of the detector. It can be measured by analyzing the geometric distortions induced in the reproduction of an image of linear sources. Poor linearity introduces image deformation and troublesome field homogeneity in tomographic mode. These linearity defects depend strongly on the homogeneity of photocathode response of the photomultiplier tubes, the number of tubes used, the homogeneity of the crystal and the light guide when is present [17]. Spatial distortions were minimized by increasing the number of photomultiplier tubes equipping the gamma cameras and selecting tubes with more homogeneous photocathodes.

1.3.6 Uniformity

The uniformity that characterizes the ability of the system to reproduce a homogeneous image when the detector is subjected to uniform irradiation of the field of view. Uniformity can cause very important artifacts in tomography: small localized variations in uniformity, of the order of 5%, can lead to circular artifacts on the images.

1.3.7 Processors

Processors provide data acquisition, display and storage of images. They also allow for online corrections and data processing. Online corrections are intended to reduce imperfections in the gamma camera. They include automatic PMT gain adjustment (verification of calibration and stability in time and space), energy correction, linearity correction (suppression of spatial distortions by correction of X and Y coordinates in real time) and correction of efficiency (standardization by correction of the values of each image pixel). Data processing consists of processing the information in order to obtain an exploitable image. It includes for example the techniques of smoothing or filtering images, and image reconstruction techniques.

1.3.8 Modes and types of acquisition of an Anger gamma camera

Anger's gamma camera can operate in two modes: a static mode and a dynamic mode.
The static mode is a mode where time information is not exploited. The information used is that recorded during the total duration of the acquisition.
The dynamic mode is a mode where time information is exploited. The information used is time-related, ie the acquired data are processed according to "activity-time" curves. This dynamic mode makes it possible to know the functioning of organs such as the kidneys (dynamic renal imaging) or the heart (dynamic cardiac imaging). For this last example, the "activity-time" curves can be obtained by a synchronization between an electrocardiogram and the gamma

camera in order to position the images in the cardiac cycle. These two modes (static and dynamic) are used as well in planar acquisition (acquisition at a single angle of view) in tomographic acquisition (acquisition in several angles of view).

- During a planar acquisition, the detection head of the gamma camera remains fixed throughout the acquisition. This acquisition makes it possible to explore only part of the body corresponding to the field of view of the gamma camera. This type of acquisition allows the doctor to have a 2D image directly interpretable, corresponding to a 2D projection of a 3D volume (the patient). No information on the deep location of the radioactive sources distributed in the patient is then available.

- During a tomographic acquisition, the detection head of the gamma camera rotates around the patient. The detection head then makes acquisitions at different values of discrete viewing angles. Typically, a tomographic acquisition has 64 or 128 viewing angles covering 360° around the patient. This type of acquisition requires image reconstruction techniques so that the doctor has interpretable images in the form of (2D) sections of a volume (3D). The deep location of the sources distributed radioactive material in the patient is then known. Tomographic acquisition is commonly called SPECT, for Single Photon Emission Computed Tomography in English.

1.3.9   Examples of scintigraphic examinations

Different medical specialties make use of scintigraphic examinations, in order to highlight certain pathologies. For example, - scintigraphy is used in cardiology (heart study). It then makes it possible to study the functioning of this muscle (its way of contracting) and to highlight possible ischemic areas during an effort or necrotic areas (in the case of infarction).

- Scintigraphy is used in neurology (study of the brain) [18]. It allows for example the study of certain degenerative diseases (such as Alzheimer's disease), epileptic, or infectious.

- Scintigraphy is used in endocrinology. It allows the study of the thyroid and parathyroid. For example, it is required if one suspects a hyperthyroid, possibly even a hypofunction or an increase in volume of the thyroid (goiter) or for the control of a surgical operation.

- scintigraphy is used in oncology. It allows, for example, to detect tumors or metastases in the bones (Figure I-5), or to identify sentinel lymph nodes during breast cancer.

1.4   The limitations of SPECT imaging

Many factors affect the qualitative and quantitative accuracy of SPECT images, including physical factors (related to the interaction properties of photons with matter), technological factors (related to the components of Anger's gamma cameras) and physiological factors (related to the distribution of radiotracers in the patient and to the morphology of the patient).

1.4.1   Physical factors

Physical boundaries are related to photon interactions in the patient's body. The two main interactions of photons with matter are the photoelectric effect and Compton scattering. Following these interactions, two phenomena affect the quantification of the activity in the area of interest: the attenuation phenomenon and the phenomenon of photon scattering by the patient's tissues and the collimator crossed before reaching the detector.
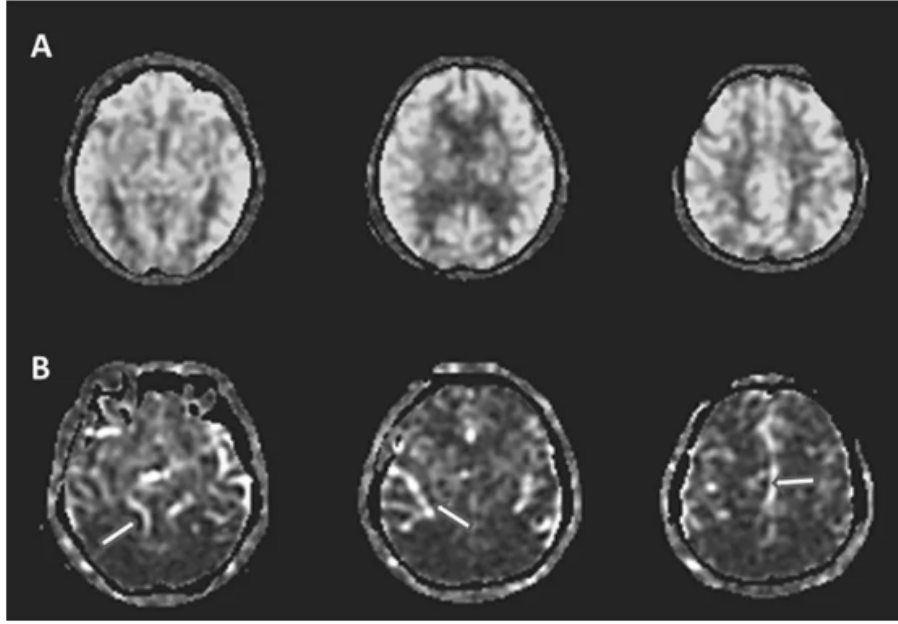
Figure 1.8: Raw arterial spin labeling (ASL) images of the represented subjects. (A) ASL perfusion images of a 70 year-old subject that is eligible for image quality checkup and enrollment. (B) ASL perfusion images from a 72 year-old subject that showed proximal portions of the arterial tree (arrows), indicating extremely prolonged arterial transit time and not eligible for study enrollment.

The attenuation

The number of photons that "disappear" (either by photoelectric absorption or diffusion at a sufficiently wide angle that they can not be detected) in the thickness dx is proportional to the number of incident photons N and to the thickness dx of material traversed; after the crossing, there remain N + dN photons:

$$dN = -\mu N dx \tag{1.10}$$

The linear attenuation coefficient μ expresses the probability that a photon will interact with matter. It depends on the material traversed and the energy $h\nu$ photons; it has the dimensions of the inverse of a length and is often expressed in cm^{-t} .This law results from the integration on a thickness x of the previous differential equation.

$$N = N_0 e^{-\mu x} \tag{1.11}$$

It is identical if we reason in flux of photons: $\phi = \phi_0\ e^{-\mu x}$, as well as in surface flux or even in intensity (provided that the light is monochromatic). A half-attenuation layer $N_{1/2}$ is defined; it is such that the number of incident photons is divided by 2.

$$N_{1/2} = \frac{ln2}{\mu} \tag{1.12}$$

$N_{1/2}$ depends on the absorbing medium (atomic number Z and state, gas, liquid, solid) and the energy $h\nu$ of the photons (but does not depend on the thickness already traversed by the

beam). Note: after a path equal to n $N_{1/2}$, the number of photons is divided by 2n. Linear attenuation coefficient and section effective interaction σ are linked by the relation:

$$\frac{\mu}{\rho} = \frac{N_A}{A}\sigma \tag{1.13}$$

Where,

ρ: represents the density of the traversed medium(g/cm^3),

N_A: the number of Avogadro (in atom mol^{-1}), A: the atomic mass of the medium (in g / mol) and σ the total cross section (in $cm^2/atom$).

The interactions responsible for attenuation are photoelectric effect, Compton scattering, scattering, and pair creation. At energies typically less than the MeV involved in medical imaging, the pair creation is not concerned since it requires a threshold energy of 1.022 MeV to create the two photons of the pair. The linear attenuation coefficient is the sum of the three partial coefficients corresponding to the three main types of interaction of radiation with matter.

$$\frac{\mu}{\rho} = \frac{N_A}{A}\left(\sigma_{photoelictric} + \sigma_{rayleigh} + \sigma_{compton} + \sigma_{pair}\right) \tag{1.14}$$

The photoelectric absorption

The photoelectric effect corresponds to the total absorption of the gamma photon by an atom whose energy is transferred to an electron that will be ejected from one of the electronic layers of the atom. This electron is called a photoelectron which carries a kinetic energy E_k equal to the energy of the incident photon E = hν minus the binding energy of the electron E_b on the electronic layer that it occupies:

$$E_k = E_\gamma - E_b \tag{1.15}$$

E_b is usually small compared to E_γ, so that the photoelectron carries off most of the photon energy.
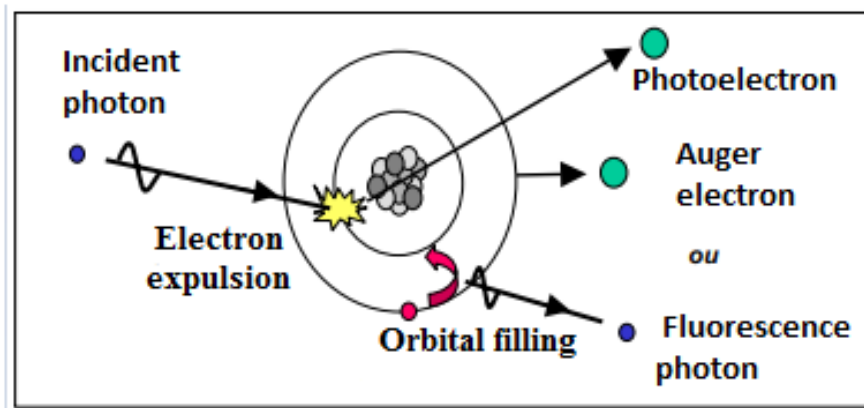
Figure 1.9: Photoelectric effect

As a result of the photoelectric effect, the vacancy in the electron shell will be filled eventually another electron from the external orbital, resulting into the emission of characteristic

x-ray (fluorescence) photons or auger electrons (effet Auger). The photoelectric effect priority being given to the more bound electrons, but it can occur with electrons of a layer i only if

$E_\gamma > E_{bi}$, where E_{bi} is the electron binding energy of the layer i. The photoelectric effect is the predominant mode of interaction of low energy γ or X radiation (≤ 100 keV) .

. It is very favored for high Z materials and decreases when the energy increases. If the photon has an energy greater than the energy of electron bonding of the K layer, it is essentially with the electrons K (more than 80%) that the photoelectric effect occurs. The photoelectric absorption breaks down into two sub-effects: the external photoelectric effect and the internal photoelectric effect. The first is the interaction of photons with the electrons of the outer electron layers of an atom. For this phenomenon, the photons must have a minimum energy hv called activation energy depending on the nature of the interaction medium. Indeed, it must be at least equal to the energy required to break the covalent bonds of the material. If this condition is fulfilled, one or more electrons of the structure absorb the energy of the incident photon thus creating the external photoelectric absorption phenomenon. When the incident energy is larger, the external photoelectric effect gives way to the internal photoelectric effect. This is a deeper interaction: the incident photon with significant energy interacts with the deep electron layers of the atom.

-Fluorescence

Fluorescence is a radiative process of de-excitation of the ionized atom. When an electron fills the vacant level from a higher energy bound state, a photon is emitted out of the atom with a hv energy corresponding to the energy difference of the start and end states of the transition. Electronic transitions coupled with the emission of a photon are subject to selection rules.

-Auger effect

An ion-excited atom, in the K-layer, for example, does not necessarily emit a K-series photon out of the atom. Indeed, the emitted photon can be absorbed by the atom itself and be used for the expulsion of a second electron from the upper layers (L, M,... in our example). This phenomenon is called the Auger effect and constitutes a non-radiative transition or internal conversion. For a given atom there is competition between the phenomenon of X fluorescence, which gives rise to the emission of a photon out of the atom, and the Auger effect, which gives rise to the emission of electrons out of the atom. It is obvious that, in a single atom, the two phenomena cant take place simultaneously: the Auger effect will therefore limit the fluorescence yield X.

The photoelectric cross section per atom σ_{ph} photo is approximately:

$$\sigma_{ph} \simeq \frac{Z^n}{E^{3,5}} \tag{1.16}$$

Where, E energy of incident photon and Z^n is the atomic number of the atom. The cross section depends strongly on the atomic number Z of the absorber medium and the energy of the photon. The exponent varies from 4 and 5 depending of photon energy.

Compton scattering

The Compton effect consists in the transfer of a part of the energy of the photon to an electron, usually to an electron of the outer layers of the atom at rest (considered as free since we can

neglect its binding energy). It follows the diffusion of a photon of energy E depending on the diffusion angle:
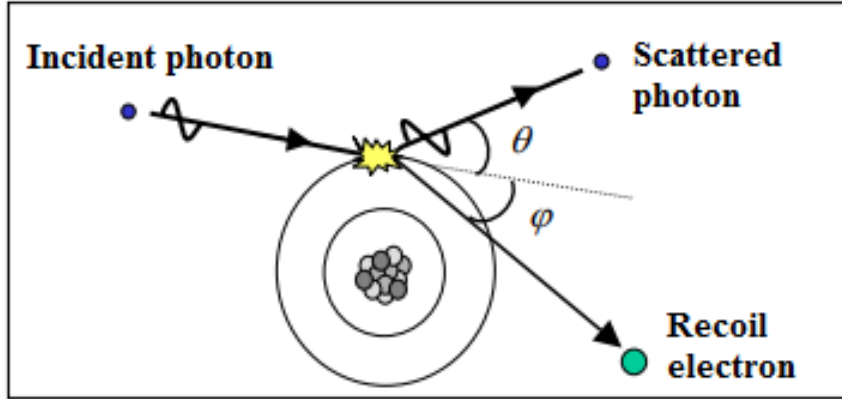
Figure 1.10: Compton effect

Both the scattered photon and the electron are emitted from the atom. In Compton effect the photons are generally more energetic than when the photoelectric effect occurs (X-rays or gamma rays).

The conservation of the energy and the momentum during the interaction make it possible to establish a relation between the incident photon energies E_γ

and the scattered photon as a function of the angle of scattering θ a thereof. In the following calculations, the binding energy of the electron is neglected because the Compton effect concerns the loosely bound electrons of the outer electron layers of the atom. The energy of the scattered photon E'_γ is given by:

$$E'_\gamma = \frac{E_\gamma}{1 + \frac{h\nu(1-\cos\theta)}{m_0 c^2}} \tag{1.17}$$

Where, $m_0 c^2$ is the electron rest mass energy (= 511 keV).

Then, the energy of the recoil electron E_e is

$$E_e = E_\gamma - E'_\gamma = E_\gamma \frac{\frac{E_\gamma(1-\cos\theta)}{m_0 c^2}}{1 + \frac{E_\gamma(1-\cos\theta)}{m_0 c^2}} \tag{1.18}$$

The angle ϕ between the trajectory the electron Compton and the direction of the incident photon is given by:

$$\tan\phi = \frac{E'_\gamma \sin\phi}{E_\gamma - E'_\gamma} \cos\phi \tag{1.19}$$

When the energy of the incident photon increases, the energetic transfer towards the electron Compton increases and the angle ϕ that makes its trajectory with that of the incident photon decreases. Two extreme cases can be identified; the minimum and maximum energy transferred to the recoil electron. Minimum energy transfer to recoil electron; $\theta=0$; $E_{\gamma\max} = E'_\gamma$ and $E_{emin} = 0$

Maximum energy transfer to recoil electron; Head on collision in which $\theta=\pi$

$$E_{e\,\text{max}} = E_\gamma - E'_\gamma = E_\gamma \frac{\frac{E_\gamma}{m_0 c^2}}{1 + 2\frac{E_\gamma}{m_0 c^2}} \tag{1.20}$$

$$E_{e\,\text{max}} = E_\gamma - E'_\gamma = \frac{E_\gamma}{1 + 2\frac{E_c}{0.511}} \tag{1.21}$$

Note: A beam of photons of the same energy gives Compton electrons whose kinetic energy varies between: $E_{\text{min}} \approx 0$ and E_{max}

Therefore, the spectrum of Compton electrons is a continuous spectrum. The angular distribution of scattered photons in the solid angle $d\omega$ about the direction θ relative to the direction of the incident photon, is obtained from the differential section per electron. The theoretical formula of Klein-Nishina giving this section effective is written:

$$\frac{d\sigma_e}{d\omega} = r_0^2 \Big[\frac{1}{1 + \alpha(1 - \cos\theta)}\Big]^2 \Big[\frac{1 + \cos^2\theta}{2}\Big]\Big[1 - \frac{\alpha^2(1 + \cos\theta)^2}{(1 + \cos\theta)^2(1 - \cos\theta)}\Big] \tag{1.22}$$

where $ro = 2,818\,fm$ is the classical electron radius and $\alpha = \frac{h\nu}{m_0 c^2}$

The electron cross section σ_e is obtained by integrating the equation on all angles. Instead, an effective cross section Compton per atom is used: $\sigma_c = Z\,\sigma_e$

Compton Cross section effect is proportional to Z and inversely proportional to the energy $E\gamma$ of the incident photon.

$$\sigma_c \propto \frac{Z}{E_\gamma} \tag{1.23}$$

Compton scattering is more important for photons with energy between 0.2 and 5.0 MeV, and predominates in absorbents with higher atomic numbers.

Rayleigh scattering

Rayleigh scattering is also called coherent scattering because it is an elastic shock of a photon with an electron strongly bound to the atom. In this case, the electron remains bound to the atom since the binding energy of the electron is high and it is therefore the entire atom that stores the shock energy of the photon. Thus, in a Rayleigh scattering, a large amount of motion can be exchanged between the incident photon and the target atom without substantially exchanging any energy [19]. The photon is at the end deviated from its initial trajectory which gives the Rayleigh effect its importance. This type of interaction is frequent for media of high atomic number and for low energy photons. This effect is often neglected in SPECT: for example, in the NaI(Tl) and for an energy of 140 keV, the Rayleigh effect represents only 6% of the interactions in the crystal, which is negligible compared to the photoelectric effect and the Compton scattering

Measurement noise

The noise corresponds to a statistical fluctuation superimposed on the signal and possibly coming from the detector (emission noise, counting noise) or reconstruction. Throughout the detection chain, be it the radioactive emission of photons, the creation of photoelectrons in the crystal, their conversion into electrons by the photocathode.

1.4.2   Physiological factors

The physiological limits are related to the distribution of radiotracers in the patient and the morphology of the patient. Indeed, radiotracers can be attached to other organs than that or those specifically sought by the tracer. This then creates a background activity in the patient's body. As a result, the contrast of the images (difference in activity measured between the region of interest and the background) is degraded. In addition, the quality of the images is deteriorated because of the movements of the patient, whether inherent (heartbeat, breathing ...) or fortuitous (movement of the patient during the examination). This causes a blur on the image and creates artifacts on the reconstructed images. Finally, the quality of the images is dependent on the size and the morphology of the patient. Indeed, the larger the body of a patient, the greater the proportion of attenuated photons and scattered photons in the tissues. The statistics of counting the gamma camera is therefore lower, increasing the noise on the image: the image is therefore of lower quality.

1.4.3   Technological factors

The technological limits are related to the components of Anger's gamma cameras, and more particularly to the detection module (NaI (Tl) scintillator and PMTs) and the collimator. These limits are translated by the parameters of the detection module (spatial resolution, energy resolution, sensitivity, uniformity and geometric linearity), some are corrected online during the acquisition by the processor, but others, whose spatial resolution, have very significant consequences on the projections acquired and the reconstructed cuts: these consequences are presented below, as well as the effect partial volume.

Collimator response

The spatial resolution is determined by collimator-detector response (CDR). The CDR results in a spatially varying and asymmetric reconstructed point spread function (PSF), leading to a blurred tomogram and consequently significantly affects accuracy and precision of radioactivity quantification.

Partial volume effect

The partial volume effect is defined as the loss of apparent activity in small objects or regions because of the limited resolution of the imaging system. These results in an underestimation of the radioactivity in the small volumes, even greater volumes become smaller. This effect is present until the size of the object is approximately three times the spatial resolution of the camera.

Septal penetration

Gamma rays that penetrate the lead septal of collimator can result in image degradation quality. In parallel-hole penetration typically occurs when gamma rays cross from one collimator hole to the next. With thicker septa, there is less penetration; however, more of the detector area is obstructed, which degrades sensitivity. A proper trade-off is thus needed. A method for

calculating the septal thickness, given a single-septal penetration of, e.g., 5% (which may be considered acceptable for some tasks), was described in Refs. 84 and 85.

1.5   Ionizing radiation

1.5.1   Electromagnetic radiation

The radiation results from the emission of energy in the form of waves of particles. There are two main types of radiation: ionizing radiation and non-ionizing radiation. Particulate or electromagnetic radiation is ionizing when it is likely to tear electrons out of the material. For this, it is necessary that the individual energy of the particles or photons is greater than the minimum binding energy of the electrons of the medium considered. X-rays, gamma rays, beta-rays (electrons) are all characterized by sufficient energy deposition to ionize the material, but show strong differences in their precise modes of interaction. With it and, in particular, with living matter. The γ and X radiation and are much more penetrating.

1.5.2   Gamma radiation

Gamma radiation is electromagnetic radiation emitted as a result of alpha or beta radiation when they produce a new nucleus in an excited state. This excess energy is released in the form of high energy photons with a high potential for penetration into matter.

1.5.3   X-rays

X-rays were discovered by Röntgen in 1895 and are not a natural phenomenon on Earth. X-rays are a form of high-frequency electromagnetic radiation consisting of photons whose energy ranges from a hundred eV (electron-volt), to about one MeV. X-rays are in the same range of energy or frequency as gamma rays, but x-rays are extra-nuclear in origin, while gamma rays come from nuclear decay (nuclear origin). X-rays can be produced in two very specific ways:
- X-rays are produced by electronic transitions involving the inner layers, close to the nucleus; the excitation giving the transition can be caused by X-rays or by electron bombardment: component of spectral lines
The bremsstrahlung radiation of electrons passing near a nucleus: continuous spectrum component.

Component of spectral lines: Fluorescence radiation

The incident electron expels an atomic electron. There is then an electronic rearrangement, an electron of a higher layer, to see a free electron, taking its place. During this rearrangement, a photon X of characteristic energy of the transition is emitted. Often the rearrangement is done with several electrons, several lines X are issued. X-rays are unique for each element as energy emitted is proportional to the binding energy of the element.

Spectrum component: Bremsstrahlung radiation

The electromagnetic radiation produced due to deceleration of a charged particle (electron) when deflected by the atomic nucleus. Bremsstrahlung energy is released under shape of a photon X or heat if the energy is low. The electron continues its course on another trajectory having been deviated by the braking, until the following atom where it will produce another photon X. Bremsstrahlung radiations have a continuous spectrum where as intense peaks of the characteristic x rays can be seen on the spectrum. The probability of hitting the nucleus is very small, to pass near the nucleus is low, and to pass away from the nucleus is high. The further the electron passes near the nucleus, the higher the energy of the X photon. At the limit, all the kinetic energy Ec of the electron is transferred to the X ray. Low energy X photons are the most numerous, but they are reabsorbed more easily in the material; important heating. The coulombic interaction is all the more important as the material is dense (high Z). The overall spectrum results from the superposition of the continuous spectrum of Bremsstrahlung radiation (which is predominant) and the line spectrum. Generally, when we speak of radiation/matter interaction, three phenomena must be taken into account and depend on the initial energy involved. These are photoelectric absorption, Compton scattering, Rayleigh scattering, and finally pair creation if the starting energy is sufficient (greater than twice 511 keV). In the case of this study, we will not be interested in the third type of interaction given the energy involved (less than 580 keV).

1.6   Spectrometry of electromagnetic radiation

Electromagnetic radiation is indirectly ionizing; any spectrometry performed using a scintillator as a detector provides the energy spectrum of the electrons displaced or created by the incident gamma or X-rays within the detector medium. The interpretation of this spectrum, knowing the different modes of primary interactions (photoelectric effects, Compton and pair creation) makes it possible to obtain quantitative information on the energy, the emission rate of the incident radiation, by means of a calibration prior. All the phenomena that contribute to the formation of an impulse have a random character.

1.6.1   Analysis of interactions in the scintillator: case of low energy electromagnetic radiation $E_\gamma \leq 1.02 MeV$

Consider a spectrometer equipped with a thallium-activated sodium iodide crystal (NaI). NaI, like any scintillation detector designed for spectrometry, will deliver pulses whose amplitudes are strictly proportional to the amount of light. This is also proportional to the energy of the electrons set in motion by the incident radiation. If the energy of this radiation is less than 1.02 MeV, only the photoelectric and Compton effects can take place.

Photoelectric absorption

A photoelectron is set in motion following the interaction of the incident γ. Its most probable energy is:

$$E_{ph} = E_\gamma - E_{ki} \tag{1.24}$$

(1) E_{ph}: Photoelectron energy E_{ki}: Electron energy of the K layer of the iodine atom The energy of this photoelectron is entirely transferred to the scintillator by collision with its electrons. The procession of the iodine atom is reorganized, leading to the emission of electronic (Auger) or electromagnetic (X) radiation. Since these radiations have low energies, they have a high probability of interaction in the scintillator. This one then recovers the sum of their energies EKi. All these phenomena can not be distinguished by the detector; only the total energy is taken into account.

$$E_{tot} = (E_\gamma - E_{Ki}) - E_{Ki} \tag{1.25}$$

$(E_\gamma - E_{Ki})$: energy of photo-electron
E_{Ki} :energy recovered during rearrangement
E_γ: incident radiation energy

It is possible that the most energetic rearrangement X-ray, $E_{xki} = (E_K - E_L)_i$, escapes from the detector without interacting. The energy then recovered by the scintillator is equal to:

$$E'_\gamma = \ E_\gamma - E_{Xki} = (E_K - E_L)_i \tag{1.26}$$

Following the photoelectric interactions two groups of pulses are delivered: - Those whose maximum amplitude is proportional to E_γ

$$V_{\max} = kE_\gamma \tag{1.27}$$

- Those whose maximum amplitude is proportional to $E'_\gamma = \ E_\gamma - (E_K - E_L)_i)$

$$V'_{\max} = k[\ E_\gamma - (E_K - E_L)_i] \tag{1.28}$$

In general the second group is quantitatively much less important than the first group. If $E_\gamma \gg E_{XKi}$, the amplitudes are very close.

Compton scattering

A Compton electron is set in motion with energy equal to:

$$E_c = E_\gamma - E'_\gamma \tag{1.29}$$

This is transferred to the scintillator. The higher the energy of the scattered radiation E'_γ , the greater the probability that it has to escape from the detector without interacting. If it interacts, it can do it either by photoelectric effect or by Compton effect. Since the detector can not distinguish cascaded phenomena, because of their quasi-simultaneity, two groups of pulses are distinguished: - those whose amplitudes are variable from 0 to a certain maximum value; they correspond to initial Compton interactions followed or not by a partial absorption of the energy of the diffused radiations produced. - those whose amplitudes are identical and proportional to E_γ ; they correspond to initial Compton interactions followed by the total absorption of the energy of the diffused radiations produced,
$V_{\max} = kE_\gamma$

1.6.2   Calibration, energy resolution

Calibration in energy

To perform the energy calibration of a gamma spectrometer, a number of radioactive sources emitting gamma radiation whose energies are known with great precision are used. The amplitudes of the pulses corresponding to the total absorption lines are recorded on each of the spectra obtained. The results obtained are then plotted on a graph paper, associating with each measured amplitude (or the channel number), the corresponding reference energy. We draw the curve joining the different points; for a good spectrometer it must be a straight line in a wide range of energy. We can deduce: - The threshold energy Es which is the smallest energy that the spectrometer can analyze due to the existence of an input threshold necessary to eliminate the background noise produced by the different electronic units (preamplifier, amplifier, analyzer) . - The slope k of the calibration line expressed in keV / mV or keV / channel for example. After locating the total absorption lines of an unknown source and determining their position V, we can deduce the energies of the emitted electromagnetic radiations using the relation:

$$E = kV + E_t$$

Then the search for energy in the tables giving the various gamma emissions will eventually identify the transmitter. If one refers to the course of radioactivity, the presence of a line of total absorption of X-radiation in a gamma spectrum may be a valuable additional indication because it allows to determine the descending element of the transmitter.

Energy resolution

The random nature of the phenomena used in a scintillation detector (light emission, emission and electronic multiplication ...) causes a dispersion of the amplitudes of the pulses collected, for identical energies ceded to the scintillator by the incident radiation. This phenomenon has the effect of modifying the appearance of the spectra, in which, in particular, the total absorption line is replaced by a total absorption peak.

1.6.3   Interaction of electromagnetic radiation outside the detector

The interaction of electromagnetic radiation in the scintillation detector environment may cause additional peaks in the observed spectrum. Gamma radiation causes by photoelectric effect on the materials surrounding the detector, the emission of X-rays characteristic of the products used.

$$E_{KX\alpha} = (E_K - E_L)_{lead}, E_{KX\alpha} = 74keV \, E_{KX\beta} = (E_K - E_M)_{lead}, E_{KX\beta} = 85keV \quad (1.30)$$

Gamma radiation causes, by the Compton effect on the materials surrounding the detector, the emission of scattered gamma radiation. They produce a rather broad backscattering peak, this being due to the energy dispersion, a consequence of the angular distribution. The energy of the scattered radiation is obtained by the relation:

$$E'_\gamma = \frac{E_\gamma}{1 + 2\frac{E_c}{0.511}}, (E_\gamma) in MeV \quad (1.31)$$

Chapter 2

Tomographic reconstruction methods in SPECT

2.1 Tomographic reconstruction

A rotating gamma camera is obtaining 2D projection images of the 3D distribution of the radionuclide at different angular positions. After data acquisition the 3D distribution of the radioactive substance can be reconstructed using appropriate reconstruction algorithm. Tomographic reconstruction consists in estimating the signal of interest that yielded the measured projections using a mathematical algorithm. The reconstruction methods are used both in X-ray transmission tomography such as scanner images and in gamma emission tomography such as Single Photon Emission Computed Tomography (SPECT) images or PET (Positron Emission Tomography) images.). We will limit this presentation to the SPECT emission tomography, since this is the framework of this thesis. In SPECT, the detection head of the gamma camera rotates around the patient and makes acquisitions (called 2D projections) at different angles of view (angle θ) of the radiotracer. The problem consists of reconstructing a volume (3D) of the patient's activity from these projections (2D). Because no information with projection operation regarding the depth at which disintegrations occur is available; moreover, activities distribution may overlap each other on the detector plane, and the contrast may be low. With only 1 projection image, it is impossible to determine the activity distribution because an several number of distributions can yield the same projection. It is as difficult as to find 2 values knowing only their sum. However, the overlap observed in the projections depends on the relative positions of the detector and of the inside the phantom structures. To solve this inverse problem, we use tomographic reconstruction methods, which we will present. Note that this 3D volume is generally visualized in the form of 2D images, for example in the form of transverse (or axial), coronal (or frontal), or sagittal sections. So, more information about the relative positions can be obtained by acquiring projections over a large number of angles of view around the phantom. The basic idea of SPECT is to determine the accurately position as possible. Consider the cut of an organ containing a radioactive focus. The distribution of activity can be defined by a function f (x, y) which at each coordinate point (x, y) of the cutting plane gives the value of the radioactive concentration. The head of the camera will rotate around the organ and under each incidence acquire a two-dimensional projection. We can define the one-dimensional projection at the angle θ, p (u, θ), corresponding to the sum of the activity along the projection lines, by the following expression:

$$p(u, \theta) = \int_{-\infty}^{+\infty} f(x, y) dv \qquad (2.1)$$

The fixed Cartesian coordinate system (O, x, y) is linked to the activity distribution f(x, y) while the rotating marker (O, u, v) is associated with the gamma camera in rotation at the incidence θ. f (x, y) the activity at point (x, y) under ideal conditions (no attenuation or diffusion). The coordinates in both landmarks are linked by relations:

$$u = x \cos \theta + y \sin \theta \qquad (2.2)$$

$$x = u \cos \theta - v \sin \theta \qquad (2.3)$$

$$v = -x \sin \theta + y \cos \theta \qquad (2.4)$$

$$y = u \sin \theta + v \cos \theta \qquad (2.5)$$

The two-dimensional projection (2D) at the angle θ corresponds to the set of all the one-dimensional projection lines (1D) at the angle θ along the z axis. It simply corresponds to the 2D image at the output of the detector obtained at the angle θ. The set of one-dimensional projections for all angles $\theta \in [0, \pi]$ is the 2D Radon transform of f (x, y), whose graphical representation is called the sinogram. The Radon transform has the following expression:

$$R[f(x, y)] = \int_0^{\pi} p(u, \theta) d\theta \qquad (2.6)$$

This Radon transform does not take into account the various disruptive physical effects (attenuation, diffusion and photon noise). Inverting the Radon transform returns to solving the inverse problem of tomographic reconstruction. In SPECT, the inverse problem consists in estimating the (3D) distribution of activity f from the acquired projections (2D). This is a problem called "ill-posed problem" for two main reasons: The first reason is that the exact analytical reversal of the tomographic reconstruction problem leading to a single solution is only possible if the number of acquired projections is infinite. In practice, however, the number of projections acquired is limited (64 or 128 views), and the data acquired by the detector is sampled and digitized, so that the solution determined is not unique. The second reason is the presence of measurement noise (Photon noise Poisson kind (major), noise detection and Electronics). The inversion of the Radon transform can be done either analytically or algebraically. A general overview of analytic and iterative methods of reconstruction in SPECT is presented in this chapter.

2.2 Analytical reconstruction methods

The analytical methods of reconstruction are based on an analytical inversion of the Radon transform. They assume that the data are continuous and that the value of a projection is known at each point (u, θ) of the sinogram.
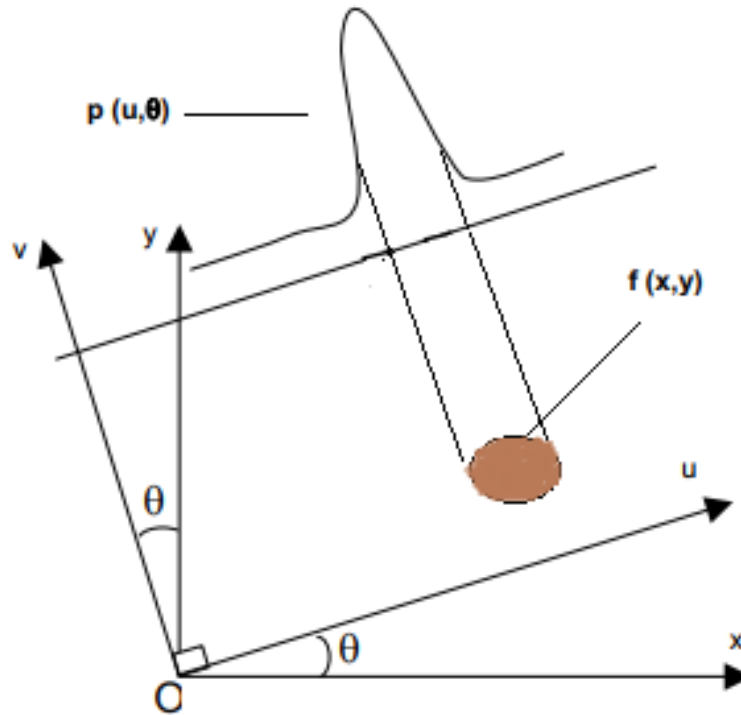
Figure 2.1: $p(u, \theta)$ projection of the activity distribution f (x, y) at the angle θ

2.2.1 Simple backprojection

The simplest analytical reconstruction algorithm is simple backprojection. This simple back-projection makes it possible to estimate the activity distribution f * (x, y) by integrating the projection p (t,θ) for all the values of θ. The projections are then simply projected in the opposite direction. The mathematical expression of this simple backprojection is:

$$f(x, y)^* = \int_0^{\pi} p(u, \theta) d\theta \tag{2.7}$$

However, this simple back projection generates areas of nonzero activities where no activity exists: these are the reconstruction artifacts, known as "artifacts star." These star artifacts decrease with increasing number of projections. One method also allows limiting these artifacts; it is the method by filtered back projection.

2.2.2 Filtered backprojection (FBP)

FBP is available on all commercial scanners (X-ray scanners, SPECT and PET devices) Bracewell and Riddle in 1967, introduced the method called filtered backprojetion (FBP) method based on Fourier Transform. The FBP is widely used due to low processing time and easy to use. It is available on all commercial scanners (X-ray scanners, SPECT and PET devices). Theoretically, under the assumption of a uniform attenuation in the studied object, filtered backprojection provides an exact solution of the inverse problem of tomographic reconstruction if the projections were continuous and the number of angles of view infinite. The theorem of projections, also called a center cut theorem (Central Slice Theorem-CST) facilitates the process. This says a

1D Fourier transform of the Radon transform of the function corresponds to 2D Fourier transform of the function. That is, performing the Fourier transform of the projections, one arrives at the space frequency distribution of densities that wish to discover. Within the operations are performed frequencies filtering and 2D inverse transform returns the reconstructed image.

$$p(\nu, \theta) = \int_{-\infty}^{+\infty} p(u, \theta)e^{-2\pi i\nu u} du \tag{2.8}$$

By replacing p(u, θ) by its value given by the equation 2.14 , we have:

$$p(\nu, \theta) = \int_{-\infty}^{+\infty} \int_{-\infty}^{+\infty} f(x, y)dve^{-2\pi i\nu u} du \tag{2.9}$$

The formulas for transforming Cartesian coordinates to polar coordinates give us:

$$\nu u = x\nu \cos\theta + y\nu \sin\theta = x\nu_x + y\nu_y \tag{2.10}$$

In addition, we have $dudv = dxdy$
Finally, we have:

$$p(\nu, \theta) = \int_{-\infty}^{+\infty} \int_{-\infty}^{+\infty} f(x, y)e^{-2\pi(ix\nu_x + y\nu_y)} dxdy \tag{2.11}$$

This double integral is none other than the two-dimensional Fourier transform of the activity distribution to be estimated. The inverse Fourier transform for estimating f (x, y) from is written as P(ν,θ):

$$f(x, y) = \int_{-\infty}^{+\infty} \int_{-\infty}^{+\infty} P(\nu, \theta)e^{2\pi(ix\nu_x + y\nu_y)} d\nu_x d\nu_y \tag{2.12}$$

We can make the change of variable by replacing $d\nu_x d\nu_y$ by $\nu d\nu d\theta$ using the Jacobian of the transformation. The integration terminals of the variable θ become 0 and 2π. Due to the symmetry with respect to the origin, the point(ν,θ) has the same value as the point (-ν, $\theta + \pi$): we can therefore use the absolute value of ν to traverse the frequency plane and vary θ from 0 to π. The equation becomes

$$f(x, y) = \int_{0}^{\pi} \int_{-\infty}^{+\infty} P(\nu, \theta)|\nu|e^{2\pi i\nu u} d\nu d\theta \tag{2.13}$$

The internal integral represents the inverse Fourier transform of the Fourier transform of the projection multiplied by the absolute value of ν: this internal integral is a filtered projection

$$\hat{P}(u, \theta) = \int_{0}^{\pi} P(\nu, \theta)|\nu|e^{2\pi i\nu u} \tag{2.14}$$

It is therefore possible to reconstruct f (x, y) by which is none other than the rear projection of the filtered projections. The projections are filtered using the ramp filter, noted $|\nu|$ in equation. The ramp filter sets the constant component to zero, which introduces negative values and amplifies the high frequencies. In practice, the ramp filter introduces negative values on either side of the filtered object, which gradually erase the star artifacts left by the projection step.

$$f(x,y) = \int_0^\pi \hat{P}(u,\theta)d\theta \tag{2.15}$$

The filtering used is the ramp filter, which makes it possible to obtain good spatial resolution. However, this filter has the effect of amplifying very high frequencies, so noise. It is then weighted by an apodization filter, for example the Hann and Butterworth filters (the most frequently used).

2.2.3 Filters used with the filtered backprojection

The filtering used is the ramp filter, which allows obtaining good spatial resolution. However, this filter has the effect of amplifying very high frequencies, so noise. It is then weighted by an apodization filter, for example the Hann and Butterworth filters (the most frequently used). Other filters are sometimes used, such as the Hamming filter or the Gaussian filter. Hann's filter [20] esponds to a cosine function in the frequency space and its formula is given by:

$$\begin{cases} H(\nu) = 0.5(1 + \cos \pi \frac{\nu}{\nu_c}) & \text{if } \nu \le 0 \\ H(\nu) = 0 & \text{if } \nu \ge 0 \end{cases}$$

The parameter ν_c s called the cut-off frequency of the filter: the lower it is, the smoother the filter, which results in a high attenuation of the noise but also in a loss of details at high frequency, and therefore of resolution, and sometimes a modification of the medium frequencies. This filter allows extremely fast calculations.

Another filter frequently used is that of [21]: it depends on two parameters, the cutoff frequency ν_c er order n which determines the rate of decay in the high frequencies. Its formula is given by the equation:

$$\begin{cases} \frac{1}{\sqrt{1+(\frac{\nu}{\nu_c})^2}} & \text{if } \nu \le 0 \\ H(\nu) = 0 & \text{if } \nu \ge 0 \end{cases} \tag{2.16}$$

If correctly set, the Butterworth filter also preserves the mid frequencies and therefore the resolution. The higher the order n, the lower the smoothing is stronger and less high frequencies is preserved. FBP works if data are not very noisy and if the measurement can be accurately modeled as a Radon transform.

2.3 Algebraic reconstruction methods

Algebraic methods are based on the discrete and matrix expression of tomographic reconstruction problem. The problem is to solve a system of large linear equations. The projections p are described in the form of a vector of dimensions $n\theta$ N^2, where nθ denotes the number of projections under which the object is seen by the detection system (number of angles of view) and NN the sampling of the detector, that is to say the number of detection pixels. The activity distribution in the studied volume is described by a vector of dimensions V^3, representing the number of voxels 3D volume to rebuild. The components of the projection vector and the activity distribution vector are respectively denoted pk

and fi, where $k \in [1, n\theta \times N^2]$ et $i \in [1, V^2]$.

A matrix, named R, makes it possible to connect the projections and the object of the distribution of activity according to the matrix expression [p] = [R]. [F]. The discrete Radon transform is then written:

$$p_k = \sum_{i}^{n} r_{ij} f_j \qquad (2.17)$$

R represents the matrix of the Radon operator of dimensions $(n\theta \times N^2 , V^3)$, and each rki element of

the matrix R represents the probability that a photon emitted by the ith voxel object is detected by the kth detector pixel. The rki coefficients of the matrix R are difficult to assess, and must be each acquisition geometry. They can integrate the physical effects degrading the image such as the attenuation of the object and the septal transparency of the collimator. The inverse problem therefore aims to estimate the activity distribution of the object volume f (3D) knowing the acquired projections p (2D) and the matrix R. A simple reasoning would be to say that $f = R^{-1}p$. However, the R^{-1} matrix inversion of the projection operator R is often impossible because of its dimensions (a non-square matrix R is non-reversible, and a square matrix too large is very difficult to reverse, the often impossible). In addition, the measurement noise and the approximation of modeling are an exact solution does not exist: we seek an approximate solution by iterative method. This approximate solution is an estimate of the object f.

There are three categories of algebraic algorithms: Iterative statistical methods, which take into account the statistical nature of the acquired data and include the Maximum Likelihood Expectation Maximization (MLEM) method and its accelerated OSEM (Ordered-Subsets Expectation Maximization) version. Filtered back-projection algorithms iterative, based on the FBP algorithm presented in section II.2.1 and were originally developed to correct the attenuation images obtained by FBP. conventional iterative algebraic methods, which reconstruct the projections by solving a set of linear equations defined by equation II.21: these methods include the ART (Algebraic Reconstruction Technique) method, the SIRT (Simultaneous Iterative Reconstruction Technique) method) [Herman, 1980], the descent method and the gradient methods. We present here only the MLEM method and the OSEM method that were used during this thesis work.

2.3.1 Statistical iterative methods

We interest in finding a vector f that is a solution of g = A.f The principle of the iterative algorithms is to determine a solution by successive estimates. The measured projections are compared with the projections corresponding to the current estimate. The result of the comparison is used to modify the current. The algorithms differ in the way the measured and estimated projections are compared and the kind of correction applied to the current estimate. The process is initiated by arbitrarily creating a first estimate for example, a image initialized to 0 or 1. It depending on whether the correction is carried out under the form of an addition or a multiplication). Statistical methods are based on a probabilistic representation of the problem. They assume that the projections contain a statistical noise. So the measurements and the object are supposed to be random variables. These statistical methods seek the object f the more likely given the p observed projections.

The Maximum Likelihood Expectation-Maximization (MLEM) method

In SPECT imaging the Maximum Likelihood Expectation Maximization (MLEM) algorithm is a popular reconstruction method, although the MLEM based image reconstruction is a time consuming process especially in the case if we use it with attenuation correction and compensation for the distance dependent spatial resolution of the detector.

The MLEM method was first developed for PET tomography by Shepp and Vardi [22], and then for transmission tomography [23] and for SPECT [24].

It assumes that numbers of both the emitted and the detected disintegrations are considered to be Poisson random variables. Let us consider fj, the mean number of disintegrations in pixel j, and the element r_{ij} of the matrix R_{ij}, the probability that bin i detects a photon emitted from pixel j. The mean number of photons emitted from pixel j and detected by bin i is a $r_{ij}\bar{f}$. The mean number of photons $\bar{r}_{ij}$ detected by bin i is the sum of the mean numbers of photons emitted from each pixel:

$$\bar{p}_i = \sum_{j=0}^{n} r_{ij}\bar{f}_j \tag{2.18}$$

It shows that the number of photons emitted from the n pixels and detected by bin i is a Poisson variable. The probability of detecting p_i photons is given by:

$$P(p_i) = \frac{\bar{p}_i^{p_i} e^{\bar{p}_i}}{p_i} \tag{2.19}$$

The maximal probability is reached when the number of counts is equal to the mean number $P(p_i = \bar{p}_i)$. The i Poisson variables are independent, and the conditional probability $P(p \mid \bar{f})$ of observing the vector g when the emission map is $\bar{f}$ is the product of the individual Probabilities $P(p_i)$. we can easily compute the likelihood function $L(\bar{f})$, so we can use the EM-algorithm to estimate f. We find for the likelihood function

$$L(\bar{f}) = P(p \mid \bar{f}) = P(p_1)P(p_2)P(p_3)...P(p_n) \tag{2.20}$$

$$L(\bar{f}) = \prod_{i=1}^{n} \frac{\bar{p}_i^{p_i} e^{\bar{p}_i}}{p_i} \tag{2.21}$$

The highest value for the likelihood $L(\bar{f})$ is found by computing its derivative. To maximize the expectation, one usually considers $l(\bar{f}) = lnL(\bar{f})$.

$$l(\bar{f}) = \sum_{i=1}^{m} (-\bar{p}_i + p_i ln\bar{p}_i - lnp_i!) \tag{2.22}$$

$$l(\bar{f}) = \sum_{i=1}^{m} (-\sum_{i=1}^{n} r_{ij}\bar{f}_j + p_i ln \sum_{i=1}^{n} r_{ij}\bar{f}_j - lnp_i!) \tag{2.23}$$

This equation, called the likelihood function, is of fundamental importance in the MLEM algorithm, because it allows one to calculate the probability to observe a projection dataset for any mean image $\bar{f}$. Obviously, we want the image that has the highest probability to yield g, so the essential point here is that the vector $\bar{f}$ for which $l(\bar{f})$ is maximal is considered as the best estimate for the solution. This maximum is found when the derivative of $l(\bar{f})$ is zero:

$$l(\bar{f}) = -\sum_{i=1}^{m} f_{ij} + \sum_{i=1}^{m} \frac{p_i}{\sum_{k=1}^{n} r_{ij}\bar{f}_j} = 0 \tag{2.24}$$

One can also write:

The MLEM algorithm estimates $f_j^{(n+1)}$ from the estimate fi(n) by a multiplicative correction factor $c^{(n)}$. This algorithm is written in the form:

$$\bar{f}_j^{\,(n+1)} = \frac{\bar{f}_j^{\,(n)}}{\sum_{i=1}^{m} r_{ij}} \sum_{i=1}^{n} \frac{p_i}{\sum_{k=1}^{n} r_{ij} f_k^{(n)}} \tag{2.25}$$

Where i and j are respectively the indices of the object voxel and the detector pixel.

$\bar{f}_k^{\,(n)} \; \bar{f}_j^{\,(n+1)}$ are the estimates of the jth voxel of the object respectively at iteration n and $n+1$.

The MLEM algorithm has some interesting properties, in particular: - If the initial estimate $\bar{f}_j^{\,(0)}$ is a positive distribution, then all the following estimated distributions will be positive; -If a pixel has a zero value at initialization, this value remains zero; The EM algorithm can be seen as a set of successive projections/backprojection:

$$\frac{p_i}{\sum_{k=1}^{n} f_k^{(n)}} \tag{2.26}$$

This factor is the ratio of the measured number of counts to the current estimate of the mean number of counts in bin i:

$$\sum_{i=1}^{n} \frac{p_i r_{ij}}{\sum_{k=1}^{n} f_k^{(n)}} \tag{2.27}$$

This is the backprojection of this ratio for pixel j. Equation*, which is to be applied pixel by pixel, can be extended to the whole image and interpreted as: $Image^{(k+1)} = Image^k$ Normalized Backprojection of (Measured projections)/projections of image(k)) The measured projections are then compared with simulated projections of the current estimate, and the ratio between these simulated and measured projections is used to modify the current estimate to produce an updated (and hopefully more accurate) estimate, which becomes iteration $k+1$.

- The total number of events is kept at each iteration. But this algorithm also has two major drawbacks: slow convergence and instability from a large number of iterations.

- This process is then repeated many times. The MLEM algorithm converges slowly: it can require up to a hundred iterations, which makes its delicate use in clinical routine. Among the existing acceleration methods are the OSEM method. The MLEM algorithm is unstable after a large number of iterations in the case of noisy data. This brings up edge artifacts and amplification of high frequencies (spatial resolution and computation noise). Thus the number of iterations directly affects the compromise between spatial resolution and noise in the reconstructed images. The simple solution of stopping the iterations before amplification of the measurement noise is therefore not optimal because it is possible to stop the algorithm before its convergence.

The FBP algorithm is faster than iterative algorithms, with the latter providing a framework for accurately modeling the emission and detection processes.

Ordered Subsets Expectation Maximization method

The OSEM (Ordered Subsets Expectation Maximizations) method is the accelerated version of MLEM. It was developed by Hudson [25] to improve the speed of convergence of MLEM. It consists of grouping the projections into ordered subsets (Figure III-41) before applying the MLEM method. The number of subsets determines the acceleration factor relative to the MLEM method. For example, a 5-iteration OSEM-8 subset reconstruction is equivalent to a 10-iteration OSEM-4 subset reconstruction, and equivalent to a 40-iteration MLEM reconstruction. It is useful for each subset to contain projections equally distributed about the patient, to help promote convergence of the algorithm. The MLEM is then applied to each subset in turn, as a subiteration. The first full iteration is complete when all subsets have been processed. Thus considerably shorten the computing time needed for reconstruction.

Statistical iterative methods regularized

In the case of heavily noisy data, the MLEM algorithm is unstable after a large number of iterations and noise then appears in the reconstructed object. The solution, to limit this noise, is to use the so-called regularization methods. These are methods based on the introduction of constraints (spatial, probabilistic) on the radioactive distribution sought in the object, thus allowing the estimated distributions to be stabilized. Note, however, that there is no standard regularization method. The introduction of a constraint on the radioactive distribution sought in the object is achieved by introducing a priori on the object (prob(f) 1). The goal is to maximize the likelihood function:

$$\arg_f max[L(f)] = \arg[prob(p|f) + prof(f)] \tag{2.28}$$

The prior knowledge of what the reconstructed image should be is introduced in the EM algorithm using Bayes theorem. It states that:

$$P(\bar{f}/p) = \frac{P(p/\bar{f})P(\bar{f})}{P(p)} \tag{2.29}$$

where $P(\bar{f}/p)$ is the likelihood function $P(\bar{f})$, the prior function, defines the a priori knowledge of the image; $P(p)$ is the a priori probability distribution of the measurements; $P(p/\bar{f})P(\bar{f})$ is the a posteriori probability distribution of the image. Taking the logarithm of both sides of Equation yields:

$$ln[P(\bar{f}/p)] = ln[P(p/\bar{f})P(\bar{f})] - lnP(p) \tag{2.30}$$

A common Bayesian prior to enforce local smoothness is the Gibbs prior, with

$$P(\bar{f}) = Ce^{-\alpha U(\bar{f})}) \tag{2.31}$$

where C is a constant, λ is a regularization parameter and $U(\bar{f})$ is a potential function of $\bar{f}$; λ is the weight of the prior and C is the weight of the prior and is a normalizing constant. The regularized MLEM algorithm proposes to estimate the object to be reconstructed by finding the maximum log-likelihood function [26] given by the equation:

$$ln[P(\bar{f}/p)] = \sum_{i=1}^{m}[(-\sum_{i=1}^{n} r_{ij}\bar{f}_j + p_i ln \sum_{i=1}^{n} r_{ij}\bar{f}_j - ln p_i!] - \alpha U(\bar{f}) + lnC - lnP(p) \quad (2.32)$$

Again, the derivative of $ln[P(\bar{f}/p)]$ is used to find the image f maximizing $ln[P(\bar{f}/p)]$

$$\frac{\partial ln[P(\bar{f}/p)]}{\partial \bar{f}_j} = \sum_{i=1}^{m} -r_{ij} + \bar{f}_j \sum_{i=1}^{m} \frac{p_i}{\sum_{k=1}^{n} r_{ik}\bar{f}_k} r_{ij} - \lambda \frac{\partial U(\bar{f}_j)}{\partial \bar{f}_j} \quad (2.33)$$

The regularized MLEM algorithm can then be written as:

$$\bar{f}_j^{(n+1)} = \frac{\bar{f}_j^{(n)}}{\sum_{i=1}^{m} r_{ij} + \lambda \frac{\partial U(\bar{f}_j)}{\partial \bar{f}_j}} \sum_{i=1}^{n} \frac{p_i}{\sum_{k=1}^{n} r_{ij}\bar{f}_k^{(n)}} \quad (2.34)$$

In the literature many potential functions are listed [27, 28, 29, 30] . For example, the quadratic potential (Geman et Geman) [30], allows taking into account the weighted average of the neighbors (b) of the voxel object (i), according to the expression:

$$\bar{f}_j^{(n+1)} = \frac{\bar{f}_j^{(n)}}{\sum_{i=1}^{m} r_{ij} + 2\lambda \sum_{a} \omega_{ja}(f_j - f_a)} \sum_{i=1}^{m} \frac{p_i}{\sum_{k=1}^{n} r_{ij}\bar{f}_k^{(n)}} \quad (2.35)$$

With wib the neighbor weighting factor (b), which satisfies Equation

$$\sum_{a} \omega_{ja} = 1 \quad (2.36)$$

The regularized method called MRP (Median Root Prior) [30, 31, 32] allows the median Mi value of the neighbors (b) of the voxel object (i), according to the expression:

$$\bar{f}_j^{(n+1)} = \frac{\bar{f}_j^{(n)}}{\sum_{i=1}^{m} r_{ij} + \lambda \frac{f_j - M_j}{M_j}} \sum_{i=1}^{m} \frac{p_i}{\sum_{k=1}^{n} r_{ij}\bar{f}_k^{(n)}} \quad (2.37)$$

This OSEM-MRP method tends to render the image locally monotonous, while preserving transitions at the edges of objects [33]. By correctly selecting the value of λ, the regulation parameter, the MRP method allows to control the noise, while obtaining contrast close to those obtained by MLEM.

This chapter reviews the problem of tomographic reconstruction in SPECT and presents the most used reconstruction algorithms, namely FBP, MLEM and OSEM. These are the algorithms of the reconstruction methods used in my thesis.

Chapter 3

Monte Carlo Simulation

Monte Carlo simulation technique was used widely in medical physics application. and are an invaluable aid to treat various problems, among which the design and optimization of imaging devices (collimator, detector ...) or the development and reconstruction algorithms. Monte Carlo modeling has been carried out by various simulation codes. In nuclear medicine Monte Carlo (MC) simulation studies are today an essential tool in a number of applications in area of emission tomography. Such applications for both single photon emission tomography (SPECT) and positron emission tomography (PET) include, among others, optimization of system design for new scanners, study of factors affecting image quality, validation of correction methodologies for effects such as scatter, attenuation and partial volume, as well as development of new reconstruction algorithms. Also use in internal dosimetry. Monte Carlo techniques simulate the random trajectories of individual particles by using machine-generated (pseudo-)random numbers to sample from the probability distributions governing the physical processes involved [2], The main advantage that all known physical interactions can be modeled fairly well. And it is practical for most applications also it can be utilized for general geometries in 1-D, 2-D, and 3-D

3.1   Review of existing simulation codes

Two types of simulation codes are available: generic codes, developed for the needs of high energy physics and dosimetry, are very comprehensive but also complex to use and not always adapted to the needs of nuclear imaging, and codes specifically designed specifically for PET and SPECT requirements, they are easier to use but also less flexible and less durable. So, there is currently no standard simulation code for nuclear imaging, which is both flexible enough to allow the simulation of original devices and validated, therefore reliable, in a large number of configurations SPECT and PET. Monte Carlo modeling has been carried out by various simulation codes such EGSnrc (electron gamma shower National Research Council of Canada), MCNP (Monte Carlo Neutron Photon), GATE (Geant Application for Tomographic Emission), and dedicated codes such as SIMIND, SimSET(The simulation system for emission tomography), SORTEO(Simulation Of Realistic Tridimensional Emitting Objects),especially designed for Single Photon Emission Computed Tomography (SPECT) and Positron Emission Tomography (PET).

3.2   Monte Carlo simulation software SIMIND

3.2.1   Introduction

Monte-Carlo methods are statistical methods based on the drawing of random numbers according to probability laws (or probability density functions) that describe the physical processes studied. Monte-Carlo methods are commonly used to solve complex mathematical or physical problems, to which analytical or numerical calculations can not provide a solution. They prove to be particularly adapted to medical physics because of the stochastic nature of the processes of emission, transport and detection. These different processes are governed by probabilistic laws: for example, the interactions of particles in matter are described by interaction cross sections representing the probability that the particle will interact in the medium. Improvements in theoretical models describing physical processes in statistical physics and particle physics have directly benefited Monte Carlo methods. The Monte Carlo method is based on the sampling of probability density functions by random number draws. To simulate each step of a physical process (particle generation, particle interaction), several random number draws may be required. The generation of random numbers is therefore a crucial step in Monte Carlo methods.

The Monte Carlo simulation program SIMIND (SIMulation of Imaging Nuclear Detectors) [5] is available in the public domain and downloadable free https://www.msf.lu.se/research/the-simind-monte-carlo-program. It has been developed by Professor Michael Ljungberg at the Department of Medical Radiation Physics, Lund University, Sweden. SIMIND is Monte Carlo-based simulation program that simulates clinical SPECT systems and can easily be modified for almost any type of calculation encountered in SPECT (Single Photon Emission Tomography) and planar imaging. A large parameters are made possible to manipulate in order to simulate different gamma camera from different manufacturers. When simulating SPECT, the camera rotates in the ZY plane either clockwise or counter-clockwise
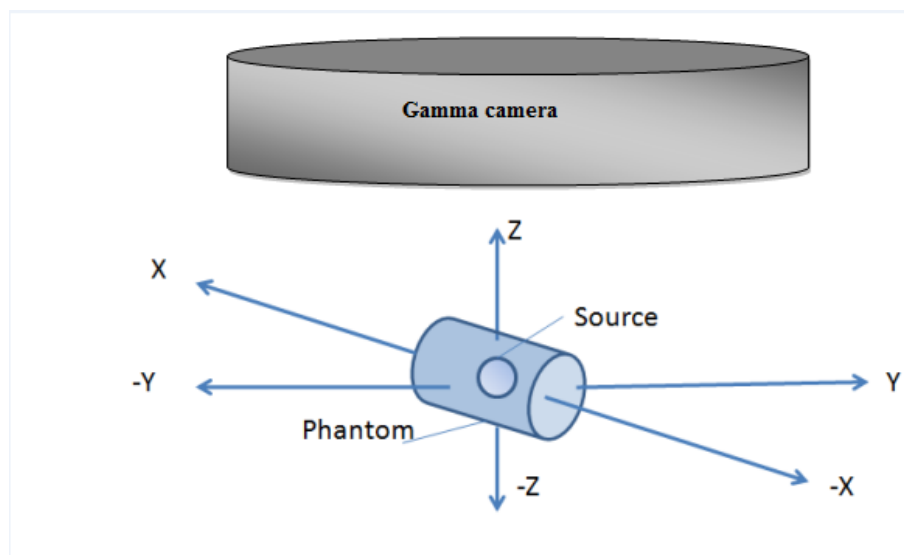

Figure 3.1: The coordinate system

The drawback with SIMIND is only simulates photons and omits the secondary electrons created through interaction in the phantom. The photon energies used in SPECT are however

relatively low and this is usually not a problem. Two main programs are used in order to set the simulations. CHANGE program and the SIMIND simulation program. The CHANGE program provides a menu-driven way of defining necessary parameters for the system that will be simulated.

The system values that are set here will be saved as input files for SIMIND which then is the program that actual makes the Monte Carlo simulation. The result from the SIMIND is then written to various results files including energy spectrum and projection images. The common way of running SIMIND is by using command files. This is very convenient since each simulation usually takes considerably time. SIMIND contains several simulation flags which the user easily can turn on and off. These flags represent different features such as SPECT simulation, simulation of photon interaction in the phantom, the addition of a collimator and a backscattering compartment behind the crystal and so on.

The SIMIND program provides images that are normalized to represent a measurement of an activity distribution. The images are also stored as floating point values. The program is based on the use of uniformly distributed random numbers for modeling the processes of the different photon interactions. It simulates the passage of photons through a phantom and collimator towards the detector crystal and calculates the projections. As in reality, the detection of the photons is affected by attenuation, scatter, the collimator and characteristics of the scintillation crystal among other things. Septal penetration and characteristic x-rays, emitted from photoelectric absorption in the collimator, can also be simulated if desired. The advantage of this Monte Carlo simulation is that it calculates parameters that are not directly measurable in experimental measurements, such as the Scatter to Total ratio (S/T) which is the fraction of the detected photons that are scattered, owing to the fact that the program can tell whether a detected photon is primary or scattered. The user can at run times change the input parameters, originally created by GANGE. each value defined by an index numbers in CHANGE can be overridden by giving a corresponding control switch eat run time. The advantage with option is that only one data file is necessary for multiple simulations.

3.2.2 Scoring routines

The following scoring routines are now included in simind.

The scattwin scoring routine

This routine performs multiple window simulations easily without the need for programming. The structure of the file is relatively simple, as shown in the following example: For easy use of the simind-generated scatter images and for the castor reconstruction program, it is possible to write two keywords in the *.win file depending on whether you select the double energy windows (DEW) method or the triple energy window (TEW) method. The structure of the file is relatively simple, as shown in the following example: 126.0,154.0,0 154.0,157.0,0 123.0,126.0,0 The files created by scattwin have the format

    out_airw1.a00
out_totw1.a00
out_scaw1.a00

The DEW method: The scatter is estimated on the basis of the previous energy window. For example, assume this energy window file: 126.0,154.0,0 92.0,124.0.74,dew This now works in such that the scatter file for the second energy window 92-124 is scaled to match the energy window in the previous setting, i.e. the scaling factor will be [154- 26]/[124-92]. In addition, the data will be scaled optionally by the constant 0.5. Thus, the total scaling will be [154-126]/[124-92]*0.74. The TEW method: This works as follows. Assume an energy window file as in this example: 126.0,154.0,0 154.0,158.0,0 122.0,126.0,1.0,tew The scatter data in the third window will then be scaled by the factor [Data2*W2 + Data3*W3]*0.5 * W1, where W1 = [154-126], W2 = [158-154], and W3 = [126- 122]. Here, there is no optional scaling, i.e. the factor is 1.0 but there could have been a value. The BIS file saved by this routine contains spectra for the total photons (spectra t), primary unscatter spectrum (spectra-p) and scattered photons (spectra-s) and the for each of the scatter orders selected (1, 2, 3, 4 ...). The spectra can be extracted using the bis program, e.g.

bis spectra spectra-t/spe:1 Extracted spectra = the total events bis spectra spectra-p/spe:2 Extracted spectra = the primary events bis spectra spectra-s/spe:3 Extracted spectra = the scatter events bis spectra spectra-fso/spe:4 Extracted spectra = the first scatter order

The forced collimation scoring routine

This is an option of including a forced collimation in the simulation to speed up the simulation. Owing to technical reasons, this option cannot be made as an ordinary collimator routine. Instead, it must be a scoring routine. The principle of the method is that multiple images are created on the basis of the distance between the lower collimator surface and the last interaction point. When the simulation of a certain projection is completed, each of these multiple images is convolved with a Gaussian function with sigma calculated from the distance between the plane for those interaction points and the camera surface. Subsequently, the images are added to a final image. The following assumptions have been made:
The ordinary collimator is turned off and the direction of the photon after the last interaction point is directed perpendicular to the crystal surface. The attenuation is then calculated on the basis of the distance from the last interaction point to the surface of the phantom. This means that the difference in attenuation as a function of the azimuthal angle close to the surfaces is not taken into consideration.
The shape of the Gaussian will be symmetric.
No backscatter from the volume behind the crystal is included.
No events from penetration or scatter in the collimator are included.
Finally, the images will be saved to *.bim or *.a00 files. Note: Because this technically is a scoring routine, it is not possible to combine this feature with the Scattwin, Penetrate, or List Model routines in this version.

The penetrate scoring routine

This scoring routine separates the components of an image or spectrum. Further, 18 different images and energy spectra are stored. The content in the energy spectrum file follows the order of appearance described above, but different spectra are stored in a single file. *.b01 All type of interactions. *.b18 photons without scattering and attenuation in the phantom. *.b19 photons without scattering and attenuation in the phantom and geometrically ollimated for primary photon energy (indicated by a negative energy in the *.isd file).

The following files are with no backscatter from the compartment behind the crystal and show events coming from.

*.b2 Geometrical collimated primary attenuated photons from the phantom.

*.b3 Penetration of a septa from primary attenuated photons from the phantom.

*.b4 Scatter from the collimator from primary attenuated photons from the phantom.

*.b5 X-rays from the collimator from primary attenuated photons from the phantom.

*.b6 Geometrical collimated from scattered photons from the phantom.

*.b7 Penetration of a septa from scattered photons from the phantom.

*.b8 Scatter from the collimator from scattered photons from the phantom

*.b9 X-rays from the collimator from scattered photons from the phantom.

The following files are with backscatter from the compartment behind the crystal and show events coming from.

*.b10 Geometrical collimated primary attenuated photons from the phantom.

*.b11 Penetration of a septa from primary attenuated photons from the phantom.

*.b12 Scatter from the collimator from primary attenuated photons from the phantom.

*.b13 X-rays from the collimator from primary attenuated photons from the phantom.

*.b14 Geometrical collimated from scattered photons from the phantom.

*.b15 Penetration of a septa from scattered photons from the phantom.

*.b16 Scatter from the collimator from scattered photons from the phantom

*.b17 X-rays from the collimator from scattered photons from the phantom.

The content in the energy spectrum file follows the order of appearance described above, but different spectra are stored in a single file.

The listmode scoring routine

This routine saves information about the photon history in a binary list mode file. The file will have the extension *.lmf. To save disk space, each record of a history in the binary file will have nine 16-bit integer values, one 32-bit float value, and one 8-bit value in the order indicated in the table. To preserve the decimal precision, the floating values have been multiplied with a scaling factor before being truncated to integers. Therefore, you should divide the values by the corresponding scaling factors before using them.

3.2.3 Source routine

The following source routines are included in SIMIND

The image-based sources source routine

This simulates a source distribution in three dimensions by using the information in a file that contains integer matrices when generating the location for the decays in the phantom. With this procedure, very geometrically complex source distributions can be simulated in a relatively easy manner. The routine simulates decays randomly within the voxel volume corresponding to the location of the source map voxel. The number of decays from that location is determined from the contents of the source map voxel. A pixel size (/PX described below) is needed for

conversion to physical coordinates because the location to a matrix cell is referred by relative indices (i, j, k). Note that this pixel size has no connection to the pixel size that defines the projections being simulated. A tumor file can be read into the source map routine and the count is incremented according to the definition in the tumor file. One tumor is defined by one row in the file as floating-point values separated by a space. Instead, the number of photon histories is determined by calculating the sum of the voxel values in the source map.

The myocardiac source routine

This is a source routine that simulates a heart consisting of a combination of a half sphere shell and a cylindrical shell, both with the same thickness. The source distribution can very accurately be matched to the physical cardiac insert manufactured by DataSPECTRUM Inc. A defect can be inserted in the half cylinder at an arbitrary location. The multiple spheres source routine This source routine simulates a Jaszczak cylindrical uniform source phantom (Data Spectrum, Inc., Chapel Hill, North Carolina). The sources must be defined in an input text file with the extension *.inp. The input file: This file is an ASCII file where each row defines a sphere. Float 32-bit valuesseparated by a comma are used. . The values at the first three positions define the size of the source. The values at positions 4-6 are the location in the coordinate system for the centre of the source. Note that this is not the centre of gravity but the starting point for each of the axes that define the ellipsoid. The value at position 7 in the row is a relative value of the desired activityconcentration (MBq/cc). The value at position 8 determines whether the source shape will be a sphere (0.0) a cylindrical horizontal rod (1.0) a rectangular horizontal rod (2.0) a hexagonal horizontal rod (3.0) a cylindrical vertical rod (4.0) a cone (5.0)

3.2.4   Running SIMIND

A simind command at the operating system prompt consists of the following parts: The program name, simind. An input file (optional). An output file (optional). Control switches (optional)

The example below considers a Windows operating system with possible differences from other operating systems in the prompt and the upper case of the characters simind input output/

Example of the program running on a PC

The user can control the input parameters created originally by change at the command level. This means that a single data file (e.g. input.smc) can be used for multiple simulations. Each value given by an index or by a flag in change can be overwritten by a matching control switch. By giving a two-character alphanumeric corresponding value, this new value takes precedence over the value defined by change. Additional characters may be given for clarity but only the first two are used.

The bim program

The bim program performs calculations on the created projection image in the *.bim file. The program is invoked in the same manner as simind, i.e. giving an input file name and additional

switches after the program name. bim input output/switches. BIM outputs a very simple 'image', based on keyboard characters, of the matrix together with calculated data and a two-row data of a profile through the matrix. The profile can then be plotted or included in a spreadsheet program for further analysis.

3.2.5   The bis program

The bis program works on the calculated energy spectra from simind. It generate a two-column ASCII string of the spectra to be used for plotting.. The program is invoked in the same manner as simind. bis input.bis output.prn/switches

The smc2castor program

The simind only creates projection images and no reconstruction software is included or supported. It is possible on some clinical systems to import the Interfile file, it is often difficult and requires a deeper understanding of the Interfile file format and how to make simind to write such a file properly. In March 2017, the Castor reconstruction software was released for download in the public domain. Information about the program can be found by visiting http://castor-project.org/. CASToR is an open-source multi-platform project for 4D emission (PET and SPECT) and transmission (CT) tomographic reconstruction. This platform is a scalable software providing both basic image reconstruction features for "standard" users and advanced tools for specialists in the reconstruction field, to develop, incorporate and assess their own methods in image reconstruction (such as specific projectors, optimization algorithms, dynamic data modeling, etc) through the implementation of new classes. The general syntax for the program is

smc2castor smcspectprojs.h00 resultfile [scatter file]/switches

where smcspectprojs.h00 is the header file for the simind SPECT simulation and resultfile is the result file for the reconstructed data. The smc2castor program creates a castor file and can spawn a reconstruction by adding the switch /ru.

The collimator database

This file includes data for the most common collimator files. It is based on a 6-character code that is associated with the dimensions of the collimator. The user can easily modify this file and add new collimators. If a user lacks some common collimators and wants to include them for other users, please send the data to Michael so that he can include them in this file for further releases. The result-file simind calculates some basic detector parameters by default. These appear on the screen and in the result file (*.res) together with the input parameters, defined in change. Collimator data are only written to the result file if a collimator has been included. SPECT input parameters are written only if the SPECT flag is set. Moreover, the scatter fraction and the percentage scatter, described below, are only written if a phantom has been simulated.

3.2.6   Some examples

Spatial resolution Simulation

Simulate the spatial resolution for a bar phantom and Tc-199m as a function of distance and collimators. Display the planer images using ImageJ program. Run the simulations with the

(a) LEHR-10   (b) LEHR-30   (c) LEGP-10   (d) LEGP-30

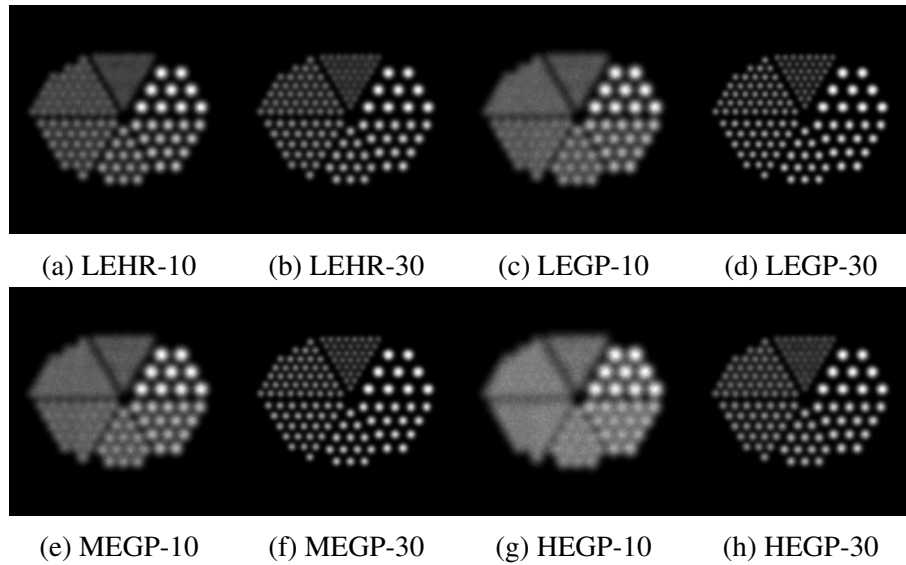(e) MEGP-10   (f) MEGP-30   (g) HEGP-10   (h) HEGP-30

Figure 3.2: Simulate the spatial resolution for a bar phantom and 140 keV photons as a function of distance in (cm) and Low energy high resolution (LEHR), Low energy all purpose (LEGP), Medium energy (MEGP) and High energy (HEGP) collimators

following command.
simind lehr lehr1/fi:tc99m/px:0.15/th:0.1/dir:3/12:30/29:5/12:10
simind lehr lehr2/fi:tc99m/px:0.15/th:0.1/dir:3/12:30/29:5/12:30
simind legp legp1/fi:tc99m/px:0.15/th:0.1/dir:3/12:30/29:5/12:10
simind legp legp2/fi:tc99m/px:0.15/th:0.1/dir:3/12:30/29:5/12:30
simind megp megp1/fi:tc99m/px:0.15/th:0.1/dir:3/12:30/29:5/12:10
simind megp megp2/fi:tc99m/px:0.15/th:0.1/dir:3/12:30/29:5/12:30
simind hegp hegp1/fi:tc99m/px:0.15/th:0.1/dir:3/12:30/29:5/12:10
simind hegp hegp2/fi:tc99m /px:0.15/th:0.1/dir:3/12:30/29:5/12:30

where /12: indicates the distance from the detector to the source. /PX is a switch that defines the pixel size of the image of the bar phantom
    (rodellh.smi),
which is used for the simulation. This pixel it not the same as the pixel of the image that simind calculates. /TH is the rods thickness, /DIR is the direction of the source. The bim images are stored as float 128×128 in the files that have the extension .bim. during the simulation, we collected 5 million of photons.

Jaszczak SPECT simulation

Jaszczak SPECT simulation consists of using spheres of different sizes and locations inside a cylindrical filled-water phantom. The jaszak.inp file give the shape, location, and activity of the six spheres. The source routine reads data from jaszak.inp, in which each row defines a sphere. We started the simulation by following command:
    simind jaszak output
The output files are, in addition to the res file, a file called jaszak1.a00, which contains 64 float 64×64 projections. Moreover, the file jaszak1.h00 is stored, which is an Interfile header.
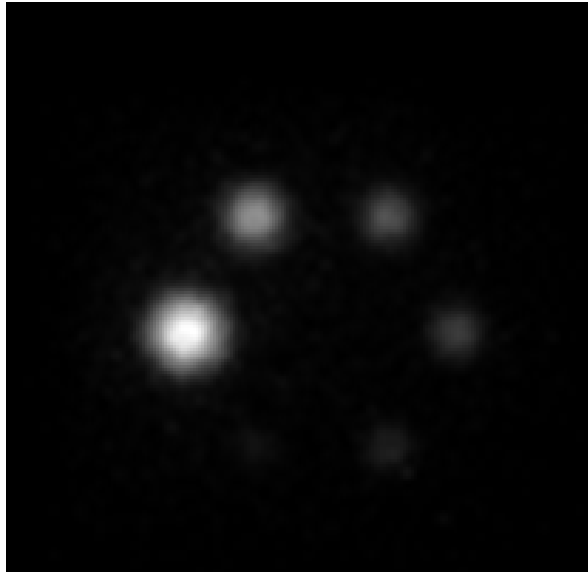
Figure 3.3: The reconstructed images of simulated Jaszczak phantom SPECT for comparing image contrast of six hot spheres with different diameters: 9.5, 12.7, 19.1, 15.9, 25.4, and 31.8 mm

We can made cold-spot simulation where the spheres activity is removed and assumed to be disabled while the rest of the phantom is assumed to be uniformly filled with activity. We perform the simulation by the command. simind jaszak jaszak2/co

We can using the activity in the spheres defined by the values in the inp file as well as background activity equal to the value defined by the /bg switch. In this case we use the following command: In the following case: simind jaszak jaszak3/bg:0.5

Simulation of bone-scan using an MDP-like radiopharmaceutical (SPECT)

The Zubal phantom consists of a set of 8-bit-coded images where each voxel has a unique value. This is related to the organ or structure that the voxel belongs to. These coded images define either density maps or activity maps provided that the user has appropriate density and activity values. It is easy to use this phantom bi SIMIND. The program reads in the 8-bit-coded images and from a special user-written table, creates activity maps. A special file called mdpect.zub is used.

The file is of ASCII type and consists of four columns 1. The organ name , 2. The unique code of that organ, 3. The density value, expressed as g/cm3*1000, and 4. A value representing the activity concentration (MBq/cc). The following example performs a simulation of an MDP-99m-Tc SPECT.

simind mdpect mdpect1/tr:11

Here, the file mdpect.zub is used as input to define the activity distribution.

Simulation of bone-scan using an MDP-like radiopharmaceutical (Whole body)

This example shows the possibility of simulating whole-body studies with the extended Zubal phantom, which has been developed by Dr Katarina Sjögreen, Lund University. The major improvement here is that the arms are in a realistic position for WB investigations.
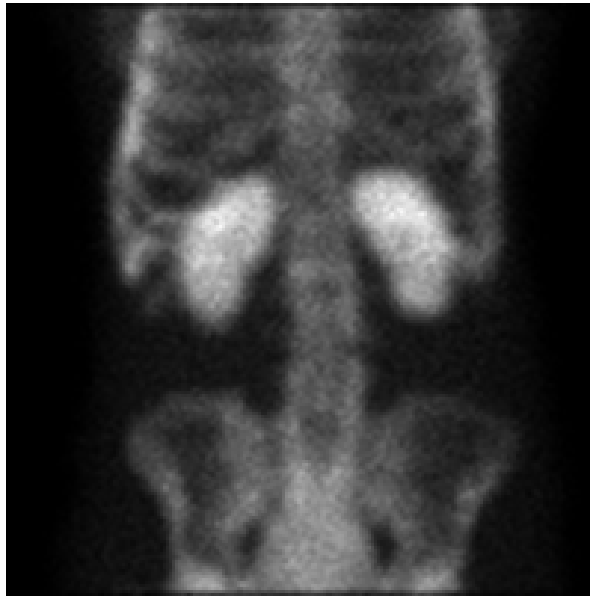
Figure 3.4: simulation of an MDP-99m-Tc SPECT

simind mdpwb mdpwb1/wb/fa:11 without phantom interactions simind mdpwb mdpwb2/wb/tr:11 with phantom interactions simind mdpwb mdpwb3/wb/tr:11/if add lesions

3.3   ImageJ software

3.3.1   Introduction

ImageJ is a public domain Java image processing program inspired developed at the National Institutes of Health and the Laboratory for Optical and Computational Instrumentation (LOCI, University of Wisconsin) [34]. It runs, either as a downloadable application or an online applet, on any computer with a Java 1.4. Downloadable distributions are available for Microsoft Windows, Mac OS, Mac OS X and Linux. The source code for ImageJ is freely available.In ImageJ can display, analyze, edit process, save, and print 8-bit, 16-bit and 32-bit (real) grayscale images and 8-bit and 32-bit color images. 8-bit images are represented using unsigned integers in the range 0 to 255. 16-bit images use unsigned integers (0 to 65,535) and 32-bit grayscale images use floating-point numbers.16-bit and 32-bit grayscale images are not directly displayable on computer monitors, which typically can show only 256 shades of gray. Therefore, the data are mapped to 8-bits by windowing. The window defines the range of gray values that are displayed: values below the window are made black, while values above the window are white. It can read many image file formats, including TIFF, PNG, GIF, JPEG, BMP, DICOM, and FITS, as well as raw formats.imageJ, analysis and processing plugin can be developed using ImageJ's built-in editor and a Java compiler is possible to solve many image processing and analysis problems with User-written plugin. ImageJ supports image stacks, a series of images that share a single window. ImageJ can calculate area and pixel value of user-defined selections and intensity-thresholded objects. It can measure distances and angles. It can create histograms and line profile plots. It supports standard image processing functions such as logical and arithmetical operation between images, contrast manipulation, convolution, Fourier analysis,

Figure 3.5: Whole body simulation

sharpening, smoothing, edge detection, and median filtering.It does geometric transformations such as scaling, rotation, and flips. The program supports any number of images simultaneously. Image can be zoomed up to 32:1 and down to 1:32. Spatial calibration is available to provide real world dimensional measurements in units such as centimeters. The calibration of density or gray scale is also available. ImageJ can made most image processing operations: viewing and adjusting the grayscale histogram, denoising, lighting correction, Fourier transformation, thresholding, logical operations and arithmetic, and in general, any type of linear transformation by custom definition of masks.

3.3.2 Basic concepts

Windows

ImageJ is a floating main window that opens data windows, which are also floating. The main window contains a menu tool bar, status bar, and a progress bar. Images, line profile, etc. are displayed in additional windows. Measurement results are displayed in the "Results" window.
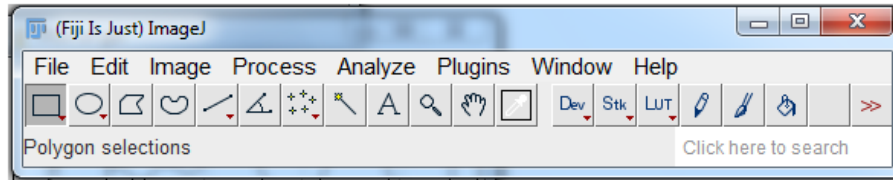
Figure 3.6: Window of imageJ

Toolbar

The toolbar contains tools for making selections, for zooming and scrolling images. Mouse over a tool and a description is displayed in the status bar.

Figure 3.7: Toolbar

Status Bar

The status bar, when the cursor is over an image, displays pixel coordinates and values. After running a filter, it displays the elapsed time and processing rate in pixels/second. Click on the status by and it will display (as shown above) the ImageJ version, the Java version, memory in use, memory available and percent memory used.
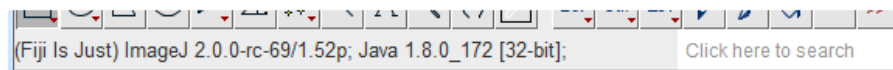
Figure 3.8: Status bar

Progress Bar

The progress bar, located to the right of the status bar, shows the progress of time-consuming operations. It will not appear if the operation requires less then approximately one second.

Figure 3.9: Progress Bar

Stacks

ImageJ can display multiple spatially or temporally related images in a single window. These image sets are called stacks. The images that make up a stack are called slices. All the slices in a stack must be the same size and bit depth. A scroll bar provides the ability to move through the slices. Most ImageJ filters will, as an option, process all the slices in a stack. ImageJ opens multi-image TIFF files as a stack, and saves stacks as multi-image TIFFs. The File>Import>Raw command opens other multi-image, uncompressed files. File>Import>Image Sequence opens a folder of images as a stack. To create a new stack, simply choose File>New>Image and set the "Slices" field to a value greater than one. The Image>Stacks submenu contains commands for common stack operations.

Selections

Selections are user defined areas or lines within an image. Area selections are created using the rectangular, elliptical, polygonal and freehand selection tools. Area selections can be measured (Analyze>Measure), filtered, filled (Edit>Fill) or drawn (Edit>Draw). Line selections are created using the straight, segmented and freehand line selection tools. Use Edit>Draw to draw the line in the current color. The length of line selections can be measured using Analyze>Measure. Selections can be moved by clicking and dragging. The status bar displays the coordinates of the upper left corner of the selection (or the bounding rectangle for non-rectangular selections) as it is being moved. Notice that the cursor changes to an arrow when it is within the selection. To move the contents of a rectangular selection, rather than the selection itself, Edit>Copy (c), Edit>Paste (v), and then click within the selection and drag. Use the arrow keys to nudge selections one pixel at a time in any direction. Rectangular and elliptical selections can be resized. As the selection is resized, the width and height are displayed in the status bar. Use the arrow keys with the alt key down to stretch rectangular or elliptical selections one pixel at a time. To delete a selection, choose any of the selection tools and click outside the selection, or se Edit>Selection>Select None (shift-a). Use Edit>Selection>Restore Selection (shift-e) to restore a selection back after having deleted it. A selection can be transferred from one image window to another by activating the destination window and using Edit>Selection>Restore Selection. Selections can be saved to disk using File>Save As>Selection and restored using File>Open. Use the ROI Manager to work with multiple selections.

File Formats

The File>Open command opens TIFF, GIF, JPEG, PNG, DICOM, BMP, PGM and FITS images. It also opens lookup tables and selections. In addition, the File>Import submenu provides

access to plugins for reading "raw" files, images in ASCII format, and for loading images over the network using a URL. To import a raw file, you must know certain information about the layout, including the image size and the offset to the image data. Files can be saved in TIFF, GIF, JPEG, PNG, PGM, FITS, tab-delimited text, and raw formats. Add support for additional formats by downloading or writing plugins. The Bio-Formats plugin from the University of Wisconsin opens 69 different life sciences image file formats. Plugins ImageJ's functionality can be expanded through the use of plugins written in Java. Plugins can add support for new file formats or they can filter or analyze images. Plugins located in ImageJ's "plugins" folder are automatically installed in the Plugins menu or they can be installed in other menus using Plugins/Hot Keys/Install Plugin. Plugins can be created or modified using Plugins/Edit. More than 150 example plugins are available for download from the ImageJ website.

 Lookup Tables

Grayscale images are displayed using a color lookup table which describes the color to be used for each of 256 possible displayed pixel values. Select alternative color palettes from the Image/Lookup Tables submenu. Use Image/Adjust/Brightness/Contrast to enhance images by dynamically changing the lookup table mapping and Analyze/Show LUT to display the lookup table of the active image.

3.4   SPECT Correction methods

Energy window methods attempt to estimate the scatter component included in the photopeak window based on photon acquisition in some other energy windows.

3.4.1   Dual Energy Window (DEW) method

The dual-energy window method assumes that the spatial distribution of the scattered photons detected in the photopeak window can be estimated as k times the spatial distribution of the photons detected in a scatter window which is placed over the Compton part of the energy spectrum [35]

$$S_{pk=kT_s} \tag{3.1}$$

Where S_{pk} is the scatter projection acquired, T_s is the total projection from the scatter window. Then, the estimated projection of unscattered photons in the photopeak window, US_{pk}, can be deduced by

$$US_{pk} = T_{pk} - S_{pk} \tag{3.2}$$

$$US_{pk} = T_{pk} - kT_s \tag{3.3}$$

The k value depends on the phantom and imaging situation used. In Jaszczak's study [8], two Tc-99m line sources were imaged in air and in a water-filled cylindrical phantom with a diameter of 22 cm. the k value was optimized to be 0.5 which resulted in a compensated line source image whose count rates were within 10% of the count rates of the image of the line source in air.

3.4.2   Triple energy window (TEW) method using trapezoidal approximation

In this method [36, 37], it is assumed that the scatter component energy spectrum in the photopeak can be estimated by the area of a trapezoid that its left and right heights are equal to the total number of photons acquired in two narrow energy windows centered on lower- and upper-edge energies of the photopeak window divided by the width of the window, respectively, that is:

$$C_{sca} = (\frac{C_{left}}{w_{left}} + \frac{C_{right}}{w_{right}})\frac{w_{pk}}{2} \qquad (3.4)$$

Where C_{left} and C_{rigth} denote the total counts detected in the left and right narrow energy windows, respectively. w_{pk} and w ($w= w_{left} = w_{rigth}$), are the widths of the photopeak and narrow windows respectively [].

Equation () is applied for each pixel in the photopeak projections to calculate scatter counts. The calculated scatter counts were subtracted from total counts for each pixel.

$$C_{prim} = C_{tot} - C_{sca} \qquad (3.5)$$

Where C_{prim} is the total count in the energy window, C_{tot} the total count and C_{sca} the scatter count.

3.4.3   Triple energy window (TEW) method using triangular approximation

In this method [38], instead the trapezoidal area, the spectrum of the scattered counts of the photopeak window is estimated by the area of a right triangle that its height is equal to the estimated scatter counts in the left narrow energy window. In this method, it is assumed:
a. There isnt any scattered photon in the narrow window centered on the upper-edge energy of the photopeak window, and therefore the photons detected in this window are only unscattered photons:

$$C_{right} = US_{rigth} \qquad (3.6)$$

b. and the photopeak is symmetric around the emission energy E0 if there is no scatter:

$$US_{left} = US_{rigth} \qquad (3.7)$$

Then the number of scatter counts in the lower narrow window can be estimated as:

$$S_{left} = C_{left} - US_{left} \qquad (3.8)$$

$$S_{left} = C_{left} - C_{right} \qquad (3.9)$$

The number of scattered photons detected in the photopeak is then:

$$C_{sca} = (\frac{C_{left}}{w_{left}} - \frac{C_{right}}{w_{right}})\frac{w_{pk}}{2} \qquad (3.10)$$

3.4.4 Dual-photopeak window (DPW) method

In this correction method [39], Instead of using extra windows next to the photopeak energy window to estimate the scatter in the photopeak window, the information in the photopeak window itself can be used. It employs the fact that the lower part of the main energy window contains more scattered photons than does the upper part. The dual-photopeak window (DPW) method is split into two abutting non-overlapping energy windows that are symmetrically located around the photopeak energy window and is assumed that for each pixel, there is a regression relation between the ratio of the scatter counts to the unscatter counts in the photopeak window, SF, and the ratio of the total counts detected in the lower subwindow to the upper subwindow, R, as shown in the following equation:

$$SF = AR^B + C \tag{3.11}$$

Where,

$$R = \frac{T_{lw}}{T_{uw}} \tag{3.12}$$

T_{lw} and T_{uw} are the numbers of counts detected in the lower and upper. A, B, and C can be calibrated by nonlinear regression analysis. It may be obtained from Monte Carlo simulations or from experimental measurement of point sources in different depths in a water phantom. The ratio between the two windows is then used to calculate the scatter fraction. The DPW method assumes that a unique regression relation exists between the SF in the total photopeak window and the ratio R.

3.4.5 Downscatter (DS) correction method

To correct for downscatter, a window above the main energy window was defined with the same width as the main energy window. The corrected image was calculated as follows [40]:

$$C_{prim} = C_{tot} - k_{ds}C_{ds} \tag{3.13}$$

Where the subscript k_{ds} is used to indicate the downscatter window. To determine k_{ds}, a region of interest outside the phantom was drawn. In the projection data outside the phantom no primary photons are present. In contrast, downscattered photons can be detected if they penetrate through the septa of the collimator, while it is assumed that they are collimated perpendicular to the detector surface. Alternatively, they can be backscattered into the crystal and detected outside the projection of the phantom. Assuming that k_{ds} is space invariant (not depending on position), k_{ds} was calculated using the formula:

$$k_{ds} = \frac{\sum C_{tot}}{\sum C_{ds}} \tag{3.14}$$

3.4.6 Channel ratio method

The same two subwindows that split the photopeak window as used in the above method are used in the channel ratio method. This method [41] assumes that the ratio of the number of

unscattered photons detected in these two subwindows is constant as well as the ratio of the number of scattered photons:

$$\frac{U_{lw}}{U_{up}} = G \tag{3.15}$$

$$\frac{S_{lw}}{S_{up}} = H \tag{3.16}$$

where U and S stand for unscattered and scattered respectively, lw and uw represent the lower window and upper window respectively.
The number of counts detected in the lower and upper windows is:

$$T_{lw} = U_{lw} + S_{lw} \tag{3.17}$$

$$T_{uw} = U_{uw} + S_{uw} \tag{3.18}$$

Then the estimated number of unscattered photons in the photopeak window can be expressed by:

$$U_{pk} = \frac{1+G}{G-H}(T_{lw} - HT_{uw}) \tag{3.19}$$

We have recalled in this chapter the principles on which Monophotonic Emission Tomography is based, as well as the limits imposed on this modality by many factors. The presence of the collimator is also an important penalty in terms of spatial resolution and sensitivity. To these technological limits are added limits due to the physical phenomena of attenuation, diffusion, variation of the spatial resolution of the camera and measurement noise. The physical origin and description of these phenomena are given in this chapter and their effects on the quality and quantification of images are underlined. It is essentially a degradation of the spatial resolution and the contrast of the reconstructed sections, which lead to errors in the quantification of images to artefacts, and affect the estimation of reliable dimensions and concentrations. Correction methods exist for these different physical phenomena and are presented in this chapter. They can be implemented before or after the reconstruction on the acquired projections or the reconstructed sections respectively.

Chapter 4

Contributions

4.1 Evaluation of Acceptance Angle in Iodine131 Single Photon Emission Computed Tomography Imaging with Monte Carlo Simulation

4.1.1 Introduction

The accurate quantifcation of iodine131 (I131) activity, which is estimated from scintigraphic images, has great importance because of the recent success of using it in thyroid cancer therapy, as well as in liver cancer therapy.[42] However, quantitative imaging is limited mainly by the phenomena of scattering and penetration into the septa of a collimator which leads to an error in the determination of activity. The highest intensity emissions of I131 are 284 (6.1%), 364 (82%), 637 (7.2%), and 723 keV (1.8%).[43] The photons of 637 and 723 keV undergo only a slight attenuation in the phantom, and they have a higher probability of penetrating the collimators. They are counted in the window of the photopeak 364 keV. [44, 45, 46] The I131 imaging was evaluated using its 364keV photons. [47] Several methods have been proposed to correct scattering and septal penetration in I131 imaging. [48, 49, 50] However, no method has yet been universally successful. The solution is to use a Monte Carlo simulation code such as simulation Monte Carlo imaging nuclear detector (SIMIND), for scatter and penetration evaluation to develop a method for correcting these events. The aim of this work was to evaluate the imaging parameters of I131, especially the collimator acceptance angle to obtain the optimum conditions allowing as much as possible the precise quantifcation of the activity

4.1.2 Materials and Methods

We simulated the Siemens Medical Systems equipped with highenergy collimator using Monte Carlo simulation SIMIND code version 5.0. We used the following imaging parameters: 0.95 cm NaI (Tl) crystal thickness, intrinsic spatial resolution of 1.2 cm, and energy resolution of 9.80% at 140 keV. The dimension of the crystal was 50c×40 cm. The energy window setting was 20% at 364 keV. The collimator data used during the simulation are given in Table 1.

A cylindrical water phantom of dimension 22 cm×30 cm×22 cm was placed at 20 cm from the detector surface. We used the SIMIND Monte Carlo simulation to acquire the data from I131 point source of $0.005cm$ diameter located at the center of the cylinder phantom. The

High energy collimator	
Hole diameter (cm)	0.506
Hole length (cm)	5.970
Septal thickness (cm)	0.2
Hole shape	Hexagonal
Type of collimation	PA

Table 4.1: Design parameters of high energy collimator

images have $0.3cm$ pixel size and 128×128 matrix size. We imported binary images created by SIMIND in ImageJ software. In this study, we used the acceptance angles to evaluate the image quality. Photons are isotropically emitted from a point source O, but the photons which are only propagating within the angle α can be detected [Figure 1]. The angle α can be defned as the collimator acceptance angle, and it is determined by the ratio of the hole size and length of the collimator [51] .

$$\alpha = \tan^{-1}(\frac{Holediameter}{Holelength}) \quad (4.1)$$
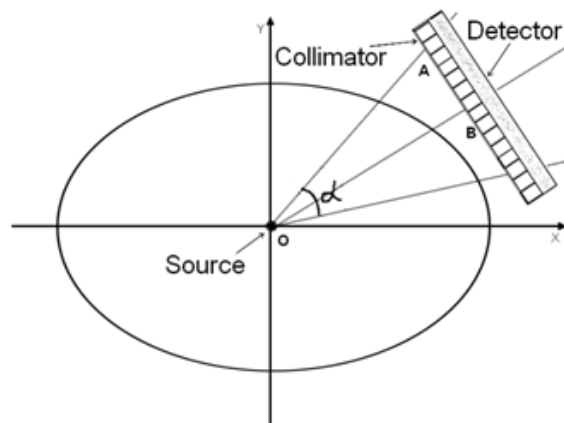
Figure 4.1: Schematic of acceptance angle

Practically, the acceptance angle α is small to eliminate most of the tilted rays.

4.1.3 Results and Discussion

The contribution of geometric, penetration, and scatter photons was calculated for a point source at 20 cm from the detector surface as shown in Table 2.

Acceptanceangle (°)	Geometric (%)	Penetration (%)	Scatter (%)
45	46.42	27.80	25.79
4.845	81.98	14.49	3.53

Table 4.2: Design parameters of high energy collimator

When the acceptance angle is 45°, the geometric component is very weak and does not carry even half of the detected photons. The scattering and penetration components are increased by the contribution of the 637keV and 723keV photons in the photopeak energy window, and thus, the geometric photons are decreased. When 4.845°is used, we notice that the geometrical component goes up to (82% at 20 cm) that explains why the contribution of the photons of the upper peaks becomes weak. This is due to small acceptance angle. Figure 2 diagram shows that blue and green spectra are obtained when the acceptance angles are 45°and 4.845°, respectively.
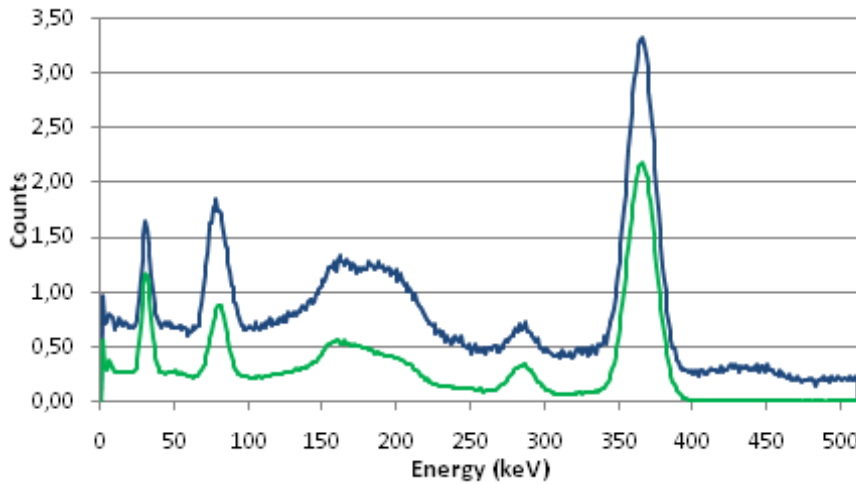
Figure 4.2: Energy spectra for iodine131 source for two acceptance angles values: Blue spectrum (45°), green spectrum (4.845°)

The counts of blue spectrum are more than the one in the green spectrum. That can be explained by the existence of other peaks of high energies such as 637 keV and 723 keV which can be detected by the detector after the scattering in the collimator. Hence, the photopeak energy window in the case of 45°contains an important part of the scattered photons in comparison to the case of 4.845°.
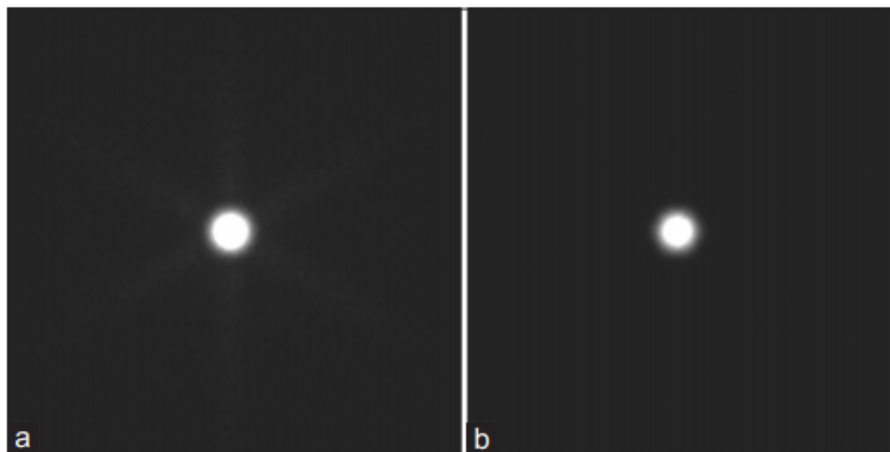
Figure 4.3: Images of a I-131 point source obtained with two acceptances angles: 45°(a) and 4.845°(b).

A star like appears in the image of Figure 3a resulted from septal penetration, while this star is not as clear as the image for Figure 3b. According to Table 3, the best resolution is obtained

when the distance between the source and the detector is 12 cm fullwidth at halfmaximum (FWHM = 7.21 mm, fullwidth at tenth maximum [FWTM] =12.36 mm), but the sensitivity slightly decreases at the same distance. Figure 4 shows that the sensitivity becomes large when using the 3cm thickness value.

Distance (cm)	Geometric (%)	Penetration (%)	Scatter (%)	Sensitivity (Cps/MBq)	FWHM (mm)	FWTM (mm)
20	81.98	14.49	3.53	54.24	9.45	16.15
15	79.28	16.83	3.89	55.07	7.9798	14.1678
12	84.75	11.99	3.26	52.36	7.21	12.36

Table 4.3: The results of the simulations at three different distances from the detector

Figure 4.4: Variation of sensitivity with NaI(Tl) crystal thickness.

4.1.4 Conclusion

In this study, we have evaluated the imaging parameters for I131 using Monte Carlo simulation. The obtained results show that the image quality ery depends on the acceptance angle. When its value equal to 4.85°, the good results were obtained for the geometric component (81.98%) and the resolution (FWHM = 7.21 mm, FWTM = 12.36 mm).

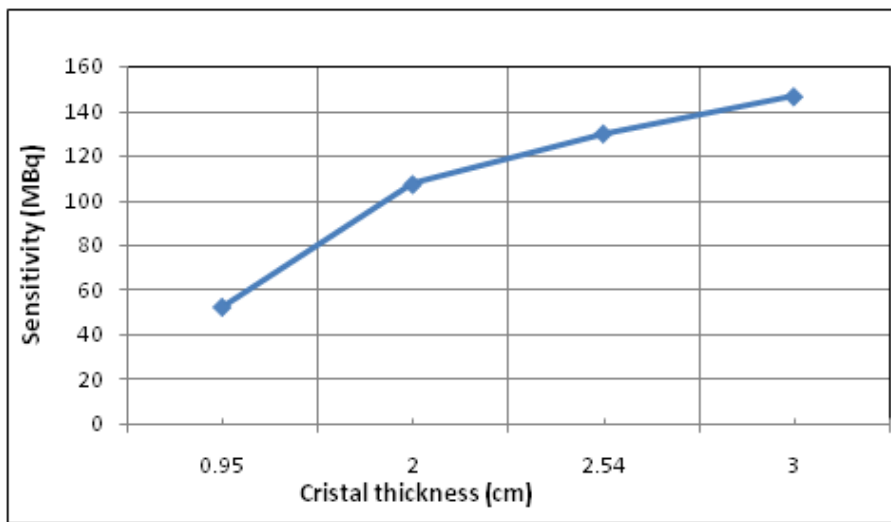## 4.2 Energy Window and Collimator Optimization in Lutetium177 Singlephoton Emission Computed Tomography Imaging using Monte Carlo Simulation

4.2.1 Introduction

In recent years, lutetium177 (Lu177) isotope is a promising radionuclide for the treatment of neuroendocrine tumors and prostate cancer. [52, 53, 54, 55, 56, 57] Lu177 has a therapeutic betaenergy of 0.5 MeV and two main gammaenergies of 113 and 208 keV (6.1% and 10.3% yield) used for imaging to evaluate the radiotracer biodistribution. We used only the higher energy peak because of downscatter from the 208 keV peak into the 113 keV window. Previous studies were investigated experimentally 20energy window with mediumenergy (ME) collimator for the 208 keV.[?, 59]] Gamma camera cannot classify the imageforming photons into primary and scattered photons. Knowledge of scatter distribution is essential for the optimization of imaging parameters and development of correction method. In this work, we evaluated three collimators highenergy (HE), Medium energy (ME) and lowenergy high resolution (LEHR) and 20%, 15%, and 10% energy windows around the 208 keV using the SIMIND Monte Carlo code .

4.2.2 Materials and Methods

In experimental study, it was not easy to calculate the scattered photon fraction accurately. Using a Monte Carlo simulation, it was possible to track the photons and hence calculate the fractions of primary, scattered, and collimatorpenetrated photons. Since high scatter and penetration fraction have deteriorated the image quality, their characterizations give insight into the effectiveness of the chosen collimator and energy window. In this work, we used Monte Carlo simulation code to simulate a planar acquisition of the Lu177 point source having 0.05 cm diameter and located in the center of the cylinder phantom. The dimension of crystal surface was 59.1×44.5 and had 2.54 cm NaI (Tl) crystal thickness. A waterled cylindricaphantom of dimension 16cm$\times$22cm$\times$22cm was placed at 15 cm from the detector surface. Three parallel-hole collimators have been used during the simulation: HE, ME, and LEHR. The collimators data used during the simulation are given in Table 1. Lutetium177 radiation emission rays are shown in Table 2. The.

Collimators	HE	ME	LEHR
Hole diameter (cm)	0.506	0.294	0.111
Hole length(cm)	5.970	4.064	2.405
Septal thickness(cm)	0.2	0.114	0.016
Hole shape	Hexagonal	Hexagonal	Hexagonal
Type of collimation	PA	PA	PA

Table 4.4: Design parameters of highenergy, medium energy and Lowenergy high resolution collimators

The Figure 1 shows the geometric used during the simulation. The projections were generated in matrices of 128 Œ128 pixels, 0.39 cm pixel size. We imported the images created by

Energy (keV)	Abundance(%)
54.61	0.016
55.79	0.027
62.99	0.003
63.24	0.005
64.94	0.002
71.64	0.001
112.95	0.061
208.37	0.103
249.67	0.002
321.32	0.002

Table 4.5: Energies and intensities of gamma rays emitted from Lu177

SIMIND in ImageJ software Institutes of Health and the Laboratory for Optical and Computational Instrumentation, University of Wisconsin (Bethesda, Maryland, USA).The authors of the SIMIND have used the deltascattering methods to sample the photon interaction through the collimators. [60] Therefore, with SIMIND Monte Carlo program, it is possible to calculate the fractions of geometrical, penetrating, and scattered photons inside the photopeak.
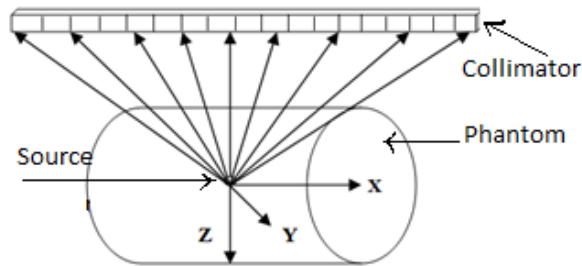
Figure 4.5: Geometry of simulation

4.2.3   Results and Discussion

Figure 2 shows the simulated total energy spectrum of a Lu177 point source in water placed at 15 cm away from detector surface. The spectrum characteristics will help explaining the choice of collimator type of imaging. Spatial resolution is an important system property and was obtained using the point spread function (PSF). In this study, we evaluated the primary and scattered PSFs for Lu177 singlephoton emission computed tomography (SPECT) imaging. It varies in shape and magnitude with collimators, as illustrated in Figure 3. It clear that, when using the ME and LEHR, we obtained a large and similar primary components, while a small components of this one for HE collimator. In Lu177 SPECT, image quality and quantifcation accuracy are degraded by scatter and penetration in the collimator.

In this study, we evaluated the geometric, penetration, and scatter component in parallelhole collimators (HE, ME, and LEHR) for 20%, 15%, and 10% energy windows, respectively, using Monte Carlo simulation. Figure 3 shows the variation of geometric, penetration, and scatter component with energy window width in HE, ME, and LEHR collimators, respectively.

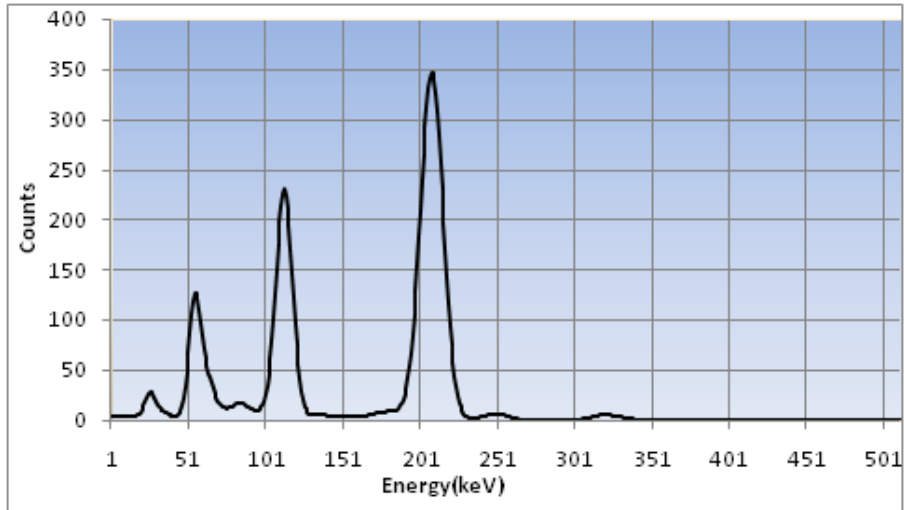Figure 4.6: The simulated energy spectrum for Lutetium177
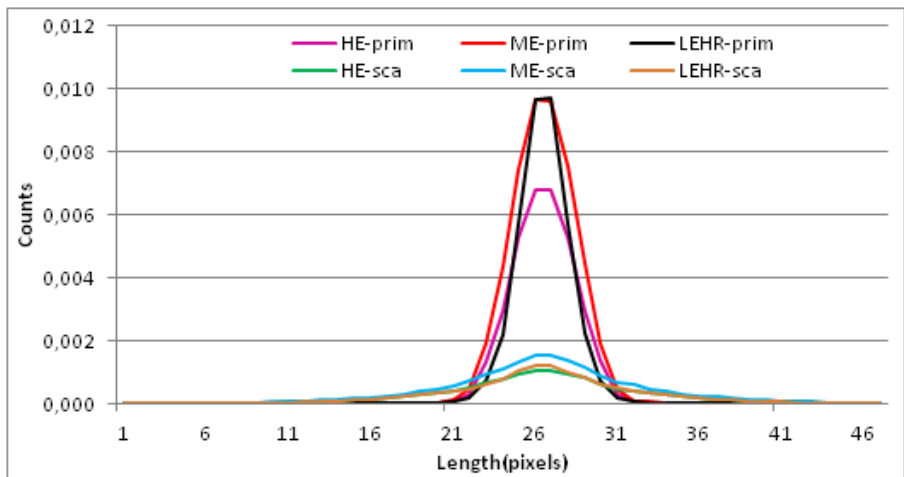
Figure 4.7: Primary and scattered point spread functions for highenergy, mediumenergy, and lowenergy high-resolution collimators

Spatial resolution was obtained using fullwidth half maximum (FWHM) and fullwidth tenth maximum (FWTM) of the PSF curve. Results for both FWHM and FWTM are shown in Figure 4. It shows that the use of a LEHR collimator would be better for good spatial resolution. The spatial resolution observed for HE and ME in comparison to LEHR collimator may be due to the combined effect of larger diameter of the holes (diameter = 0.506 cm for HE and diameter = 0.294 cm for ME) and increased septa thickness.

As shown in Figure 5, It is clear that the geometric component is large and remains constant with increase in energy window width collimator produces a weak component of geometric for the three windows. It suffers from a lot of penetration and scattering from the main emission peak. Collimators are made mostly of lead materials with a high density and have holes that allow only those photons traveling along the desired paths to pass through and will determine the geometrical feld of view. It also essentially determines the sensivity and

resolution of the system. Collimator sensitivity refers to the percentage of incident photons that pass through the collimator. Therefore, only a small fraction of emitted photons pass
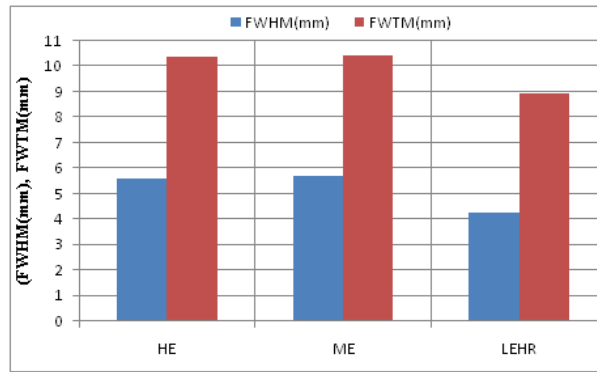
Figure 4.8: Fullwidth half maximum and fullwidth tenth maximum of the point source images with highenergy, mediumenergy, and lowenergy highresolution collimators
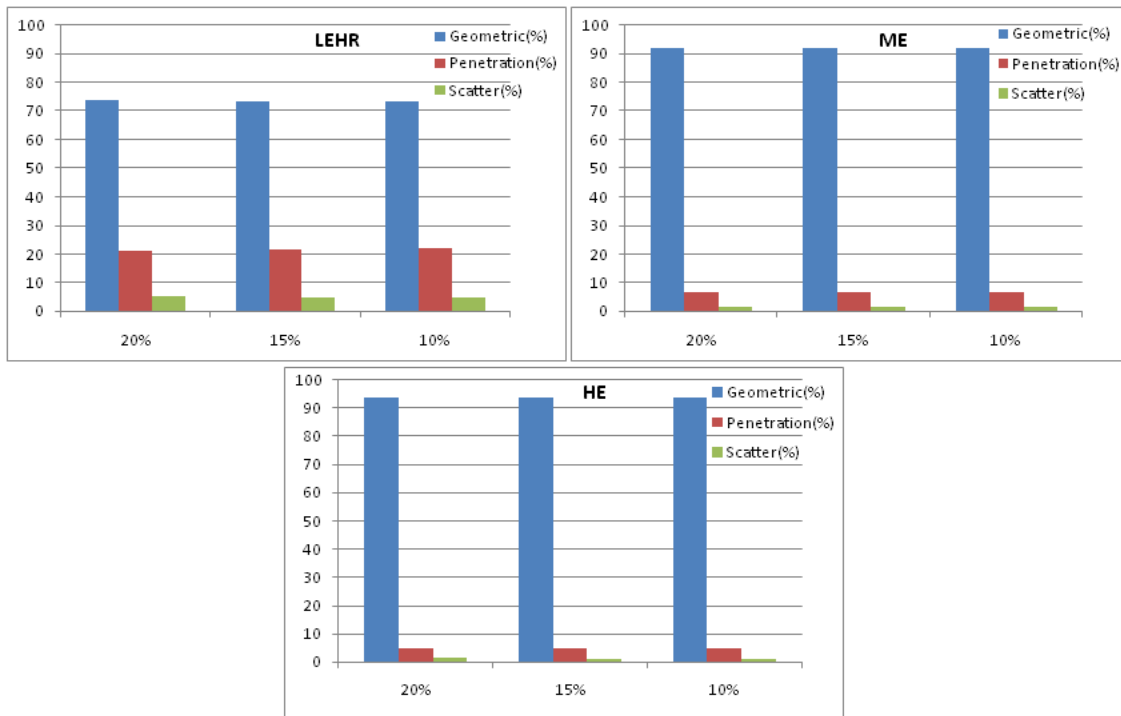
Figure 4.9: The variation of geometric, penetration, and scatter component with energy window width for high energy, medium energy, and low energy highresolution collimators

through the holes and are detected, which seriously limit sensitivity. The sensitivities were determined by the ratio of the detected counts in the energy window per second per unit activity (cps/MBq). In this study, we presented the impact of HE, ME, and LEHR collimators on sensitivity as it affects the image quality in Lu177 SPECT imaging, as illustrated in Table 3.

The sensitivity decreases when the energy window width decreases. The better sensitivity is recorded by ME collimator with 20% window. Figure 6 shows total and scatter images of point source obtained as a result of the simulation. The sixfold symmetry of tails is related with the hexagonalhole shape of the collimator used in the simulation. As shown in Figure 6, the foggiest image has the highest value of collimator penetration and scatter.

Energy windows, n (%)	HE	ME	LEHR
20	5.75	8.21	6.26
15	5.20	7.42	5.69
10	4.26	6.08	4.68

Table 4.6: Sensitivity (Cps/MBq) as function of energy windows for highenergy, mediumenergy, and lowenergy highresolution collimators
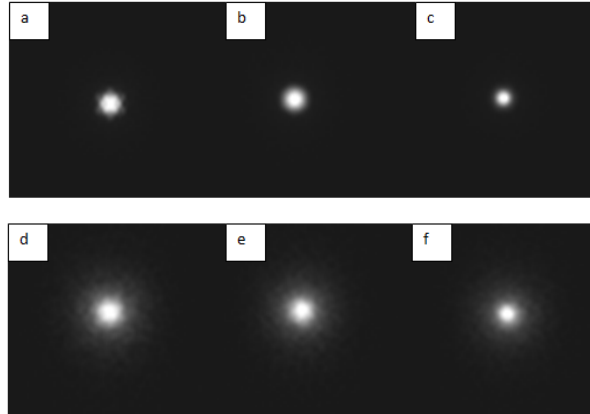
Figure 4.10: Total images obtained with highenergy (a), mediumenergy (b), and lowenergy highresolution (c) collimators. Scatter images with highenergy (d), mediumenergy (e), and lowenergy highresolution (f) collimators

4.2.4 Conclusion

From this study, we believe it should be evident that solely using ME collimator and 20% energy window is enough to improve Lu177 SPECT image to its fullest extent. The result provides the optimal collimator and energy window for Lu177 SPECT imaging and will help the quantifcation of Lu177.

4.3 Energy window optimization for Y-90 Bremsstrahlung SPECT imaging: Monte Carlo simulation

4.3.1 Introduction

The short halflife (64.1 h) of the yttrium-90 and its quasi-pure emission of high energy beta particles. makes it the privileged isotope in targeted radionuclidetherapy for treatment of non-Hodgkin s lymphoma and unresectable liver cancer [61, 62]. Whereas, the Y90 bremsstrahlung photons have a continuous and broad energy spectrum, with a high energy (Emax = 2 MeV).

Therefore, the image quality is influenced by the photons detected in the energy window. Subsequently, the choice of collimator and energy window have a great influence on Y-90 imaging. Pervious works have used Monte Carlo simulation to select the appropriate collimator and energy window settings for bremsstrahlung SPECT of Y90 [63, 69]. The classification of photons is done according to their history in the collimator: the geometric photons (photons passed through a collimator hole), the scatter photons (photons that scatter in the collimator or in the object) and the penetration photons (photons that penetrated the collimator and that did not scatter in the collimator or in the object). Moreover, the photons absorbed in the collimator septa can provide a x-rays component. [70].

Only the geometric photons provide correct positional information. The authors of the SIMIND Monte Carlo code have used the delta scattering methods to sample the photons interaction through the collimators. Therefore, SIMIND Monte Carlo program can accurately simulate all interaction of photons inside the collimator. Subsequently, with the Monte Carlo Simulation technique, accurate assessment of the geometric, penetration and scatter contributions inside the photopeak window can be made.

Several works have been interested in SIMIND Monte Carlo Simulation program, to determine the different components of the detected radiation. Bremsstrahlung imaging makes difficult to choose collimator and energy window, hence the optimal clarity of the image is not always achievable. Therefore, in this work, we used the SIMIND Monte Carlom: code to estimate the geometric, penetration, and scatter components for parallelhole collimators. Y90 sensitivity is very low, because approximately 1% of the kinetic energy of the β^- particle is emitted in the form of Bremsstrahlung radiation, which decreases the image quality. To overcome this problem, i.e. to increase the sensitivity, a large window could be used, but it includes a large contribution of scattered photons. In this study we choice the six narrow energy windows and two collimators in order to optimize the tradeoff between the sensitivity and resolution for Y90 bremsstrahlung imaging.

4.3.2 Materials and methods

In this work, we used the SIMIND (6.2) code to simulate the Siemens Medical System Symbia equipped with detector having: 0.95 cm NaI(Tl) crystal thickness, intrinsic spatial resolution of 0.45 cm and energy resolution of 8.80 % at 140 keV. The dimension of the crystal was 59.1 Œ 44.5 cm2. A 0.05cm diameter point source filled with Y-90 (3.7 MBq) was placed at 15 cm from the detector and located in a cylindrical water phantom (diameter 16 cm, length 32 cm). Acceptance angle of photons emitted towards the camera was set as 45deg.The pixel size in the simulated planar source images is 0.34 cm and 128 Œ 128 matrix size. At the end of the simulation SIMIND code creates a planar image having float values (real *4). We imported

these images in ImageJ software [18]. In this simulation we included two collimators: Medium Energy (ME) and High Energy (HE) (Table 1).

Diameter(cm)	Septa(cm)	Length(cm)	Hole shape	Collimator type	collimator
0.294	0.114	4.064	hexagonal	Parallel hole	ME
0.400	0.200	5.970	hexagonal	Parallel hole	HE

Table 4.7: Collimators data

We have chosen six energy windows ranging from 10 keV to 580 keV (Table 2). Figure 1 illustrates the SIMIND simulation of for point source.

Windows (keV)	[10.50]	[51.120]	[121.189]	[190.259]	[260.329]	[330.580]
Center (keV)	30	85	154	224	294	485

Table 4.8: Energy windows used during the simulation

The Figure 1 shows the geometric used during the simulation. The simulated Y-90 images were quantitatively evaluated using spatial resolution (FWHM, FWTM) for both the HE and MELP collimators.
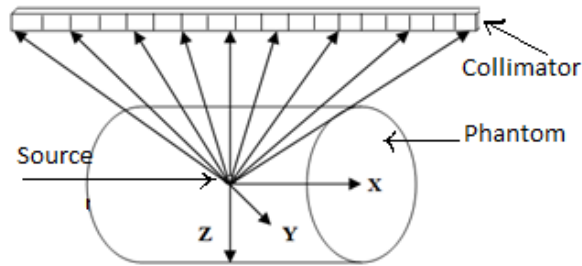
Figure 4.11: Geometry of simulation

The SIMIND program has two main programs; CHANGE, which define the system parameters and SIMIND, which execute the simulation. Moreover, using CHANGE program, we can introduce the desired parameters of system. At the end of simulation, SIMIND provide the value of geometric, penetration, scatter and x-rays component and image in separate files. The simulated Y-90 images were quantitatively evaluated using spatial resolution (FWHM, FWTM) for both the HE and ME collimators.

4.3.3 Results

In this study, we evaluated the geometric, septal penetration, scattering components and x-ray in parallel-hole collimators (ME and HE collimators) using Y-90-point source with six energy windows ranging from 10keV to 580keV using SIMIND Monte Carlo code. The result of the simulation is given in Table 3.

Figure 2 shows the variation of geometric, penetration, scatter and x-rays components with energy window in ME and HE collimators, respectively.

Collimator	Energy window	Geometric(%)	Penetration(%)	Scatter(%)	X-ray
ME	[10-50]	63.55	16.28	19	1.1
	[51-120]	56.89	17.98	18.59	6.54
	[121-189]	32.87	31.77	35.37	0
	[191-259]	13.64	48.32	38.04	0
	[260-329]	7.33	44.97	47.7	0
	[330-580]	2.39	46.47	51.14	0
HE	[10-50]	83.3	5.78	10.22	0.7
	[51-120]	72.62	8.6	13.4	5.38
	[121-189]	61.17	16.31	22.52	0
	[191-259]	32.49	26.12	41.38	0
	[260-329]	17.44	32.19	50.37	0
	[330-580]	6.03	31.01	62.96	0

Table 4.9: Results of the simulation

The geometric component has decreased with energy window. While, the penetration and scatter components has increased with increase of energy window. We noted that, the geometric component reaches 83% for the collimator HE and 63% for the ME in 51-120 keV energy window. The high penetration and scatter components are due to the large spectrum of Y-90 (up to 2000 kev). It is clear from Figure 2 that the penetration and scatter are a significant problem for ME making this collimator less useful for imaging. Moreover, even for the HE collimator, the penetration and scatter effect is also significant. (Figures (3,4)) show images of Y-90-point source obtained experimentally and by the simulation respectively. The absence of pronounced photo-peak energy of bremsstrahlung photons is the main reason for a poor quality of Y-90 point source image (for simulation and experimental) obtained by HE and ME collimators.

This is evident from the calculated value of high septa penetration and scattering obtained as a result of the simulation in Table 3. It is important to note that, the foggiest images has the highest value of penetration and scatter for both collimators. The 6-fold symmetry of tails is associated with the hexagonal-hole shape of the collimator used in the simulation. The measured and simulated spatial distribution PSFs of the photons detected in the six-energy window is shown in Figure 4. To characterize the point source profiles, the FWHM is not enough because of the presence of tails at the sides of the PSFs; therefore, also the FWTM must be assessed. The FWHM and the FWTM were computed on the simulated PSFs.

Results for both FWHM and FWTM are shown in Table 4.

The values of the FWHM and FWTM are reported in Figure 5 for the PSFs normalized at their maximum value. It shows that, the ME collimator increases the FWTM. For all energy windows, we have found more FWTM (less spatial resolution) for ME in comparison to the HE collimator. The calculated sensitivities in six energy windows are listed in Table 4.The FWHM and FWTM were better (FWHM= 7mm, FWTM=35,06mm) in the 51120 keV window than another window for HE collimator.

The HE sensitivity was lower than ME sensitivity for six energy windows as shown in Figure 6. The spatial resolution (FWHM= 7mm, FWTM=35,06mm at 51120 keV) observed with HE collimator is best spatial resolution with consideration of HE sensitivity observed. The ME collimator gives higher sensitivity and septal penetration. On the other hand, the HE collimator gives a lower sensitivity and septal penetration.
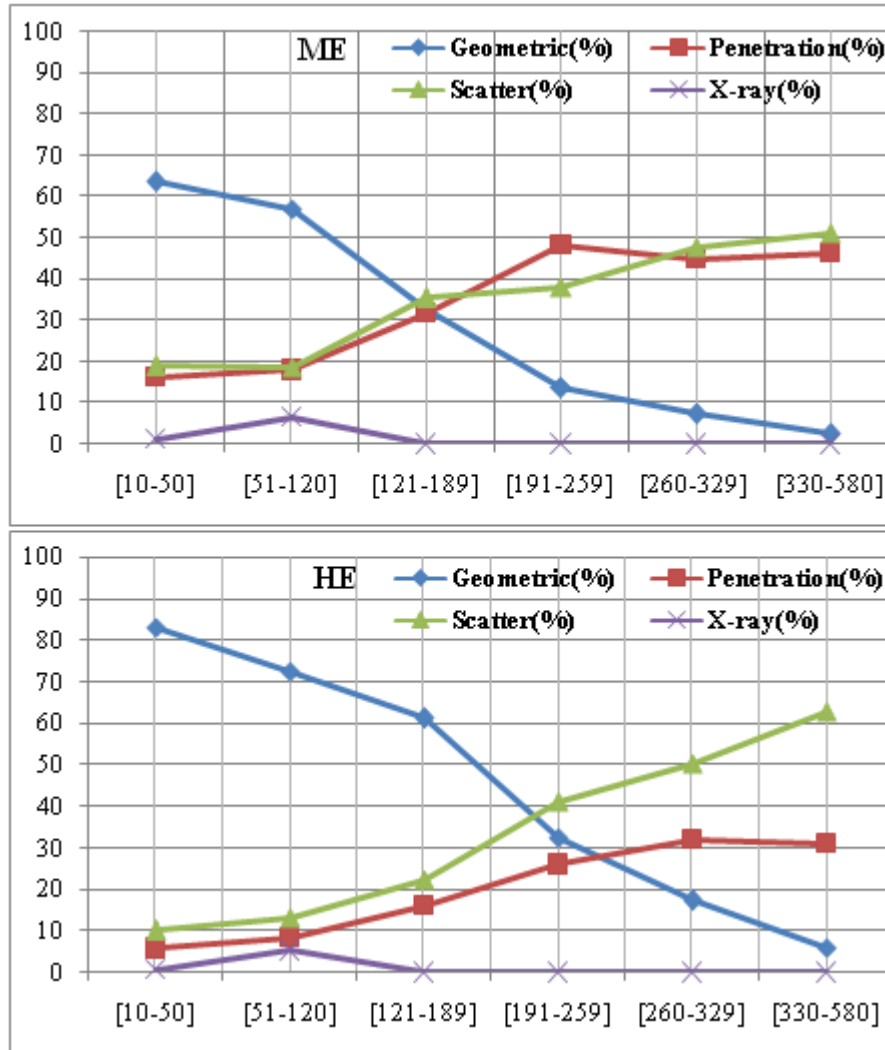
Figure 4.12: The variation of geometric component (photons detected on the detector without any scatter or penetration), penetration component (photons passed through septa without attenuation), scatter (photons that scatter in the collimator) and x-rays component (photons that are absorbed in the septa collimator) as a function of the center energy for ME and HE collimators.

4.3.4   Discussion

Scattered and penetration photons through the collimator septal are the degrading effects of image in the Y-90 bremsstrahlung SPECT imaging.. For a particular selection of collimator, the fogginess in the images has changed with energy window. The good images quality can be achieved when using HE collimator. From the profiles, the FWHM and FWTM were determined and it were found significantly varied with energy windows for both collimators. The HE collimator offers higher resolution than the ME collimator, for all energy windows. The Y-90 sensitivity is related to image noise, which can be important for detecting small amounts of activity. The sensitivity (Cps / MBq) was calculated as the ratio of the total counts in the field of vision and the acquisition activity. The collimators with parallel holes, the sensitivity and the spatial resolution have an inverse relationship. A longer hole means better spatial resolution but low sensitivity. Therefore, a range of collimators is often used to achieve the optimal compro-
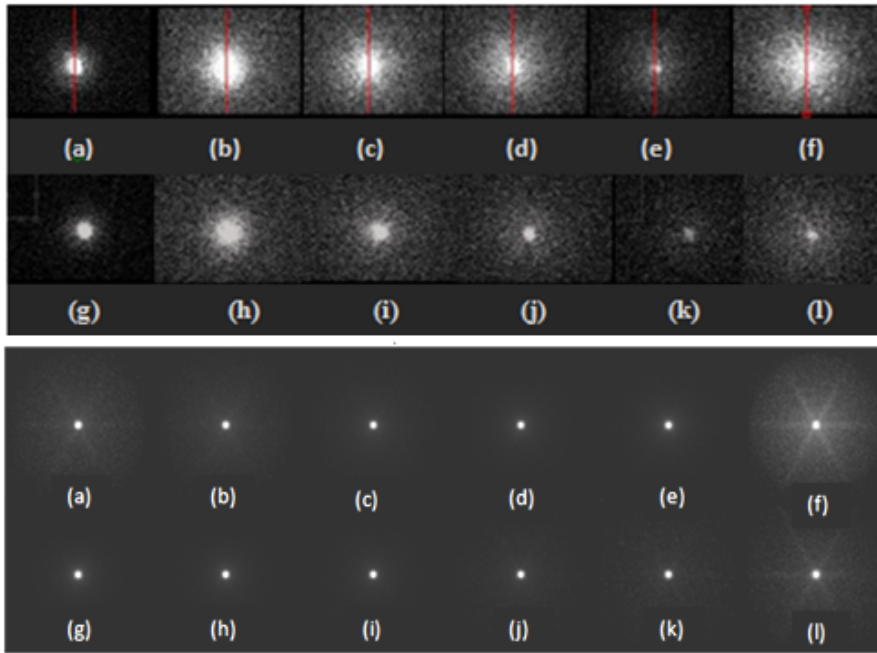
Figure 4.13: Image of the Y-90 point source: obtained experimentally (above images) and by the simulation (below images) which were obtained in energy window widths:(a,g) 10-50keV, (b,h) 51-120keV, (c,i) 121-189keV, (d,j) 190-259keV, (e,k) 260-329keV and (f,l) 330-580keV.
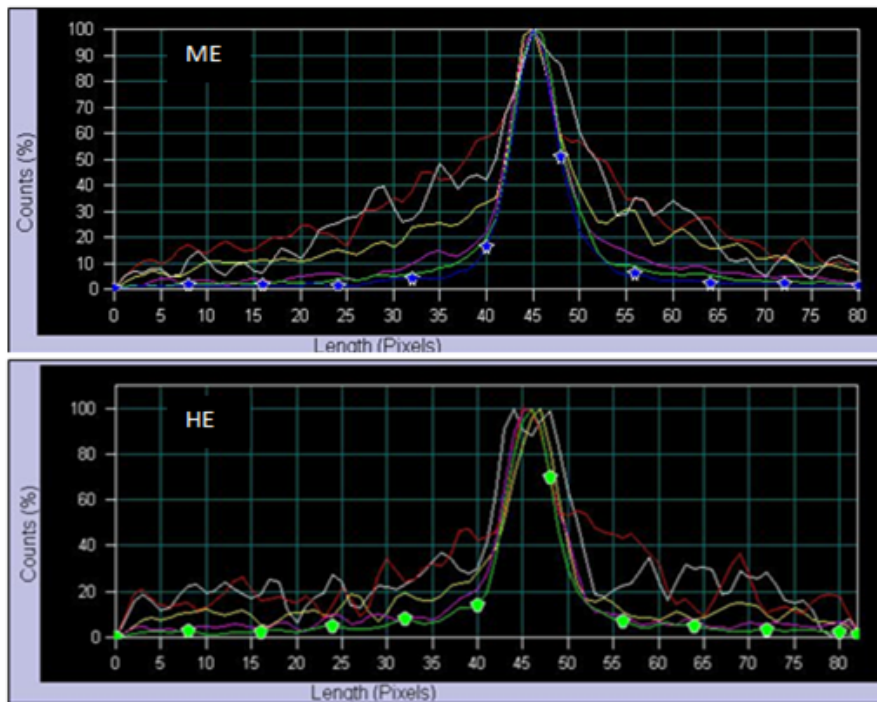
Figure 4.14: spread functions (PSFs) vs pixels number: simulation data

mise between sensitivity and resolution. To improve the sensitivity, a large energy window was used but this can lead to a decrease in resolution. The ME collimator offers higher sensitivity and lower spatial resolution compared to the HE collimator because the HE collimator reduces
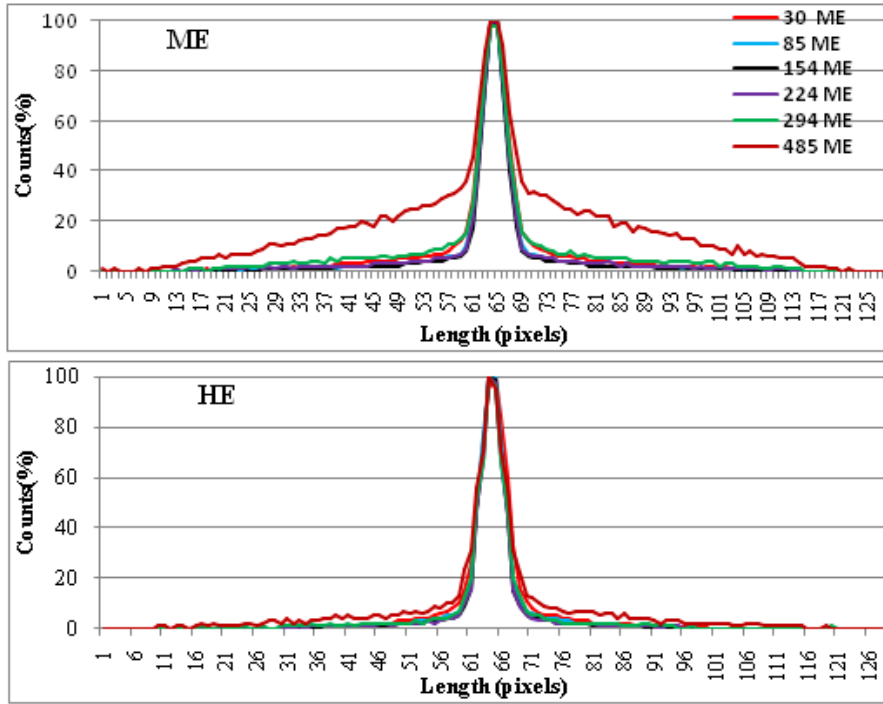
Figure 4.15: Point spread functions (PSFs) vs pixels number: experimental data [(30keV-blue); (85keV -green); (154keV-magenta); (224keV-yellow); (294keV-white) and (485keV-red)]

septal penetration with thicker septa. The determination of collimator and the energy window for Y-90 imaging are therefore a compromise between sensitivity and spatial resolution.

Collimator	Energy window	FWHM(mm)	FWTM(mm)	Cps/MBq
ME	[10-50]	7.05	36.45	1.27
	[51-120]	6	49.03	1.82
	[121-189]	5.94	36.92	3
	[191-259]	8.26	47.87	1.34
	[260-329]	2.19	39.13	0.84
	[330-580]	3.36	72.96	2.25
HE	[10-50]	7.42	30.06	0.71v
	[51-120]	6.59	35.12	1.63
	[121-189]	6.23	28.75	0.78
	[191-259]	4.39	29.63	0.4
	[260-329]	3.6	20.09	0.21
	[330-580]	5.56	35.26	0.9

Table 4.10: FWHM of the point source images
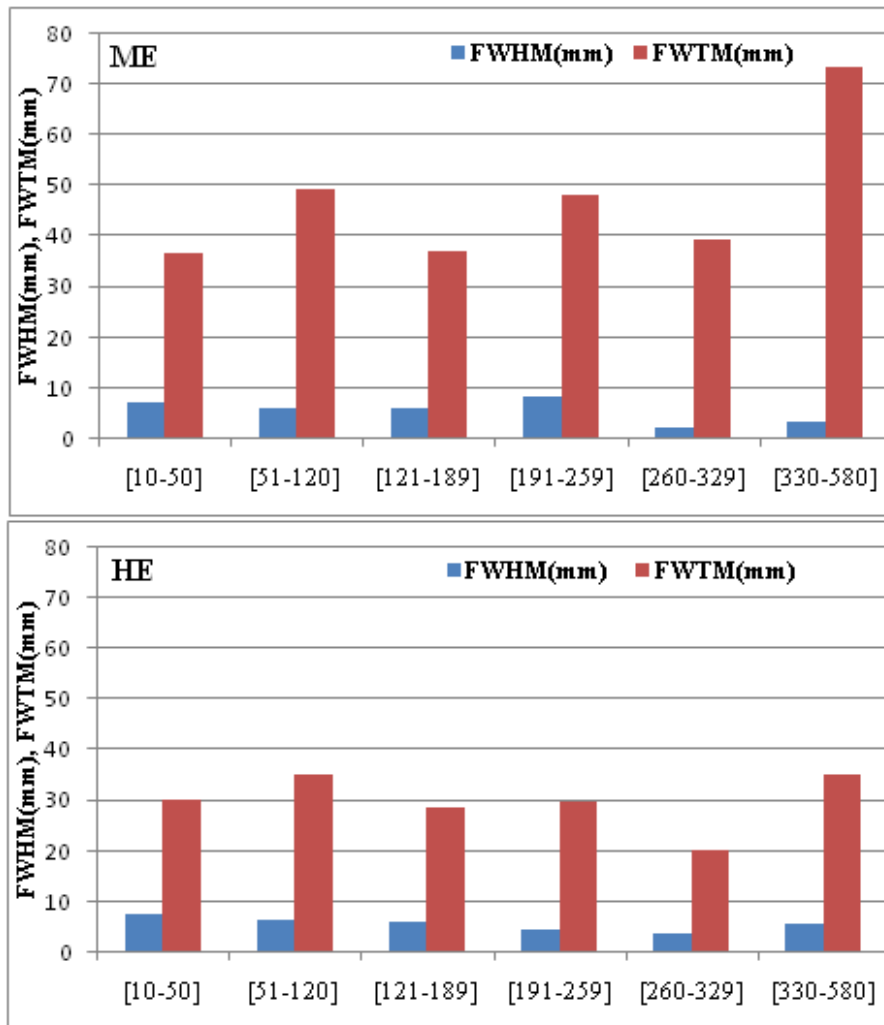
Figure 4.16: spread functions (Full widths at half of maximum (FWHM) and Full widths at ten of maximum (FWTM) vs. energy with ME and HE collimators
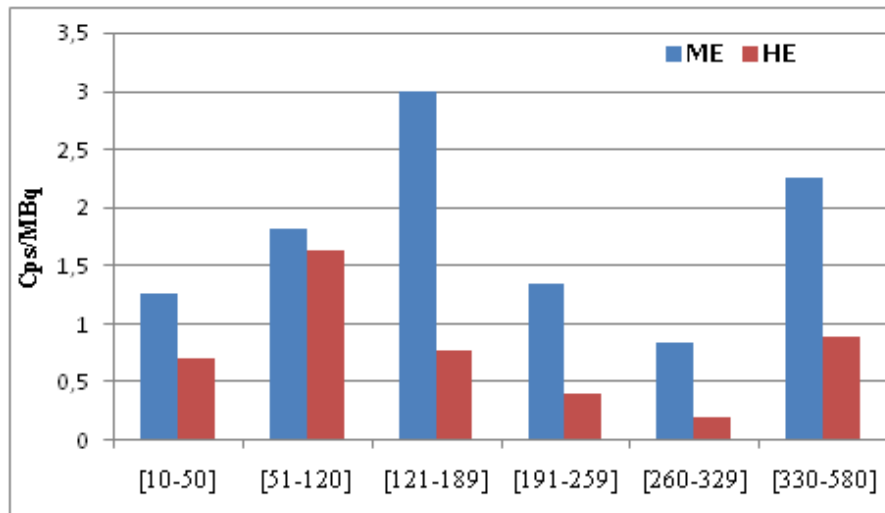
Figure 4.17: spread functions (Sensitivity in counts per second per unit activity (Cps/MBq) Vs energy

4.3.5 Conclusion

We evaluated the effect of the parallel hole collimators and energy window on the resolution and sensitivity using SIMIND Monte Carlo program. The results indicated that the best compromise between the sensitivity and resolution was obtained when using an energy window 51-120 keV.

4.4 Optimization of scatter correction method of Sm-153 at nuclear medicine using TEW; a Monte Carlo simulation study

4.4.1 Introduction

In nuclear medicine, Samarium-153 (Sm-153) isotope is potential choice because
, it emits both medium-energy β^- particles ($E_{\beta max} = 0.80 MeV$) with a short half-life (46.7 h) and gamma-photons suitable for imaging at 103keV. The physical characteristics of Sm-153 allow to be considered as excellent radiotherapeutic and diagnostic image agent [71, 72]. Pervious works [72, 73, 74] demonstrated that, the isotope chelated to ethylene diamine tetramethylene phosphonate (EDTMP) is an effective treatment of bone metastases by the excellent biolocalization. Moreover. Sm-153 is potentially suitable as an alternative to 90Y in liver cancer treatment with advantage of gamma radiation for imaging [75]. Images obtained additionally permit be a rapid diagnostic of the therapeutic isotope. In Sm-153 single-photon emission computed tomography (SPECT) imaging with a gamma camera, the presence of scatter results in introduces significant uncertainty in quantification of activity distribution. The scattered and primary photons cannot be determined experimentally. While, with the help of Monte Carlo Simulation, it is possible to track the photons originating from the source that ultimately deposits its complete energy inside the crystal. It is increasingly used in nuclear medicine to develop new imaging parameters, scatter correction methods and reconstruction algorithms. We have used Monte Carlo simulation SIMIND to accurately assess the contribution of scattered photons in the photo-peak window. The quantification of gamma-camera imaging is improved after the correction of scattered radiation. Previous works [76, 81] were used TEW (triple energy window) scatter-correction to eliminate the detected scattered counts inside energy window. In order to quantify emission from the isotope Sm-153 using a gamma camera accurately, however, it is important to correct the scattered photons which degrade image quality. We can reduce the counts of scattered photons in a photo-peak energy window using TEW method, which is a simple method to use in Clinical study for SPECT imaging. However, there are to date no study of measurements of the scatter fraction of Sm-153 as a function of the energy windows, in order to determine the optimal main- and sub-energy window for Sm-153 SPECT imaging. In this study, we assessed the fraction of scattered photons and determined the optimal main and sub-energy windows for triple energy window (TEW) scatter correction method for Sm-153 by means of Monte Carlo simulation.

4.4.2 Materials and method

4.4.3 Detection system description

In this study, we simulated Siemens Medical System Symbia equipped with low-energy high resolution (LEHR) (Table1). The images were acquired by a single-head SPECT system (Symbia) based on 103 keV peak. The dimension of detector surface was 59.1cm Œ 44.5cm and having 2.54cm NaI (Tl) crystal thickness. A water-filled cylinder phantom (diameter 22 cm. length 32 cm) was placed at 12 cm from the detector surface. We used the SIMIND Monte Carlo program to acquired data from a Sm-153 point sources of 0.05 cm diameter located in

different seven positions at the center of the cylinder phantom and offset by ś 5 cm in the X. Y. and Z directions relative to the center. Moreover, the Jaszak phantom consists of six spheres with different diameters (31.8, 25.4, 15.9, 19.1, 12.7 and 9.5 mm) which are used to evaluate the image contrast. Figure 1 illustrates the SIMIND simulation for each point source.

Low Energy High Resolution (LEHR) collimator	
Geometric of hole	Hexagonal
Length of hole (cm)	5.970
Septal thickness(cm)	0.016
Diameter of hole(cm)	0.111

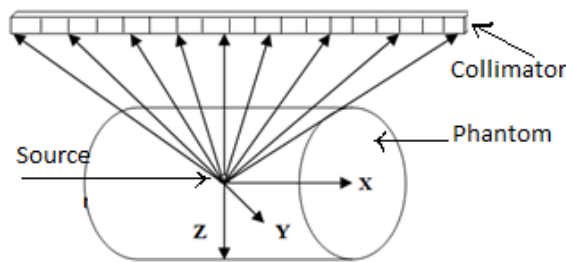Table 4.11: Design parameters of (LEHR) collimator

Figure 4.18: Geometry of simulation

We collected 50 millions photons during the simulation. The images had 0.34 cm pixel size and 128 $times$ 128 matrix size. Figure 2 shows photons energies and intensities of I Sm 153 radionuclide decay.
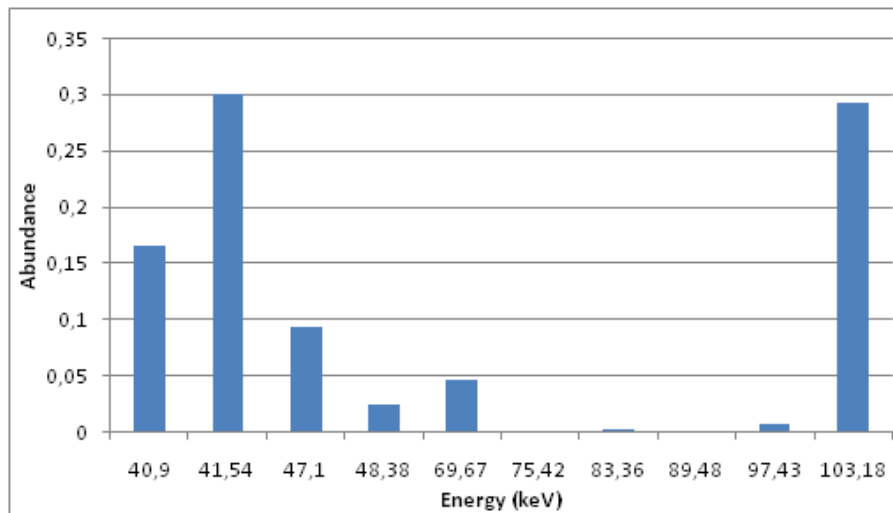

Figure 4.19: Energies and intensities of gamma rays emitted from the samarium 153 sources

Energy(keV)	40.90	41.54	47.10	48.38	69.67	75.42	83.36	89.48	97.43	103.18
Abundance	0.166	0.300	0.094	0.024	0.046	0.001	0.002	0.001	0.007	0.292

Table 4.12: Samarium-153 main radiation emission rays.

Monte Carlo simulation

The Monte Carlo simulation SIMIND code , describes a SPECT camera. The SIMIND program has two main programs; CHANGE, which define the system parameters and SIMIND, which execute the simulation. Moreover, using CHANGE program, we can introduce the desired parameters of system. SIMIND accurately simulate all interaction of photons inside the collimator. At the end of simulation, SIMIND provide the value of geometric, penetration, scatter and x-rays component and image in separate files. We imported binary images created by SIMIND in ImageJ software [77]. The validation of the SIMIND program for SPECT imaging has been verified for different gamma camera according to the previous studies [78, 82] [1923].

Triple energy window (TEW) method

The TEW method estimates the counts of the scattered photons in the main photo-peak window from the counts acquired in two sub-windows on both sides of this window. At each pixel in planer image, the counts of scattered photons are subtracted from the total counts in photo-peak window to obtain the count of primary photons. If the measured count is not enough, we can enlarge the width of the sub-windows. In this study, we used the main-energy windows widths (10, 15 and 20%) centered on 103 keV and sub-energy windows widths (2, 4 and 6 keV) Table 2.

The true scattered photons fractions for the main energy window calculated by SIMIND were compared with the scattered photons fraction assumed from TEW scatter-correction method. The counts of scattered photons and counts of primary photons were calculated by relationships below [14.15]:

$$C_{sac} = (\frac{C_{left}}{W_s} + \frac{C_{right}}{W_s})\frac{W_m}{2} \tag{4.2}$$

$$C_{prim} = C_{tot} - C_{sca} \tag{4.3}$$

Where C_{left} counts in lower sub-energy window;C_{right}: counts in upper sub-energy window; Ws: width of sub-energy window; Wm: width of main window; Ctot:counts in main window; Csca: scatter counts and C_{prim}: primary counts. The scatter to total ratio (scatter fraction) was calculated as Eq.(3) [6]:

$$S/T = \frac{C_{sca}}{C_{tot}} \times 100 \tag{4.4}$$

The quality of the Sm-153 SPECT image was quantitatively evaluated using the image contrast assessment. Contrast was calculated by the following formula using Eq.(4):

$$Contrast = \frac{M_s - M_b}{M_s + M_b} \tag{4.5}$$

Where, M_s and M_b are the mean pixel values of the activity of spheres and the activity of background as noise, respectively.

4.4.4 Results

The simulated energy spectrum is shown in Figure 3. The counts acquired in different windows is shown in Table 3. Table 4 shows the comparison of true scatter fraction (%) and scatter fraction estimated by TEW scatter correction method at each position. The scatter fraction depended on the source position in cylindrical phantom. The results showed that; for 20% of the main energy window and 6 keV sub-energy window of Sm-153, the scatter fraction estimated by TEW is similar to the true scatter fraction determined by SIMIND. Figure 5 demonstrates the images for Sm-153 point source at seven positions. The calculated vertical and horizontal FWHM on the images is shown in Table 5. It shows that, for each position, the TEW method is decreasing the FWHM. Figure 6 show the reconstructed images of simulated Jaszczak phantom SPECT before and after scatter correction. It noted that, the contrast of the six spheres was improved with 20% of the main-energy window and 6 keV sub-energy windows for TEW as shown in Figure 7. Therefore, 6keV sub-window with a 20% main-energy was possible energy windows setting for the TEW method in Sm-153.
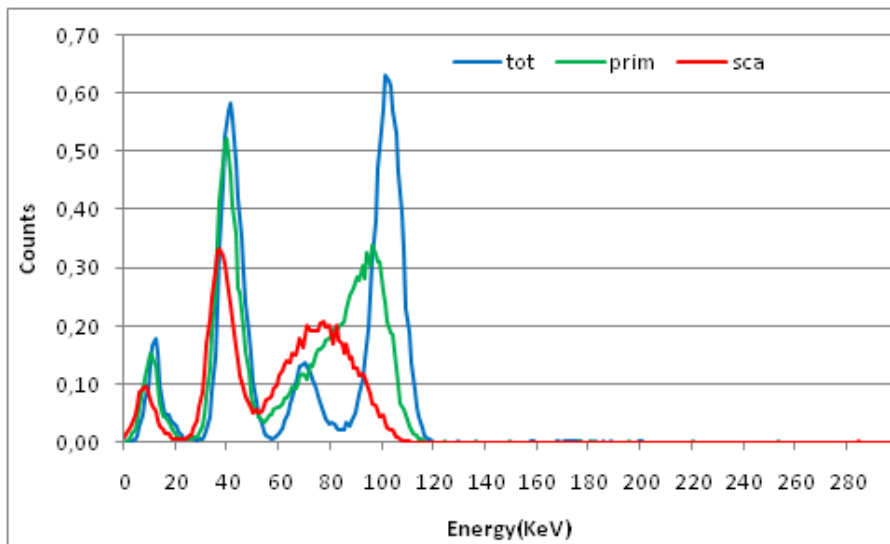
Figure 4.20: The simulated photon spectrum emitted by the Sm-153.

Table 3 shows the comparison of true scatter fraction (%) and scatter fraction estimated by TEW scatter correction method at each position. The scatter fraction depended on the source position in cylindrical phantom. The results showed that; for 20% of the main energy window and 6 keV sub-energy window of Sm-153, the scatter fraction estimated by TEW is similar to the true scatter fraction determined by SIMIND.

Figure 3 demonstrates the images for Sm-153 point source at seven positions. The calculated vertical and horizontal FWHM on the images is shown in Table 4. It shows that, for each position, the TEW method is decreasing the FWHM.

Figure 4 show the reconstructed images of simulated Jaszczak phantom SPECT before and after scatter correction. It noted that, the contrast of the six spheres was improved with 20% of the main-energy window and 6 keV sub-energy windows for TEW as shown in Figure 5.

Range(keV)	Counts
93- 113	11500
113- 115	386
91- 93	1270
113- 117	656
89- 93	2480
113 - 119	822
87 - 93	3600
95 - 111	9660
111 113	544
93 - 95	1330
111 - 115	930
91 - 95	2600
111 - 117	1200
89 - 95	3810
98 - 108	6430
108 - 110	818
96 - 98	1400
108 - 112	1440
94- 98	2790
108 - 114	1900
92 - 98	4060

Table 4.13: The counts acquired in different windows
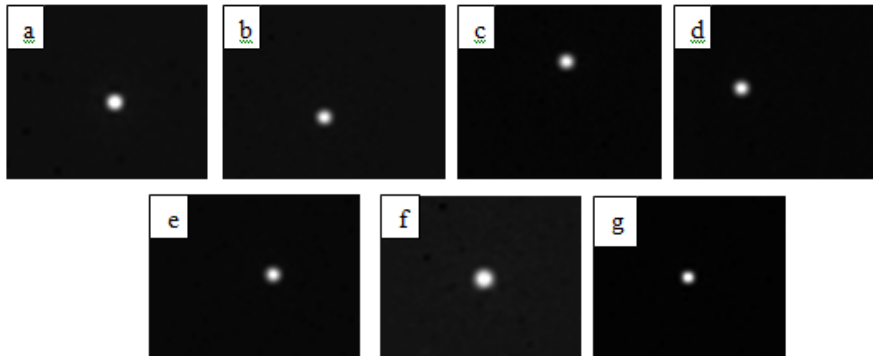
Figure 4.21: Images for Sm-153 point source at each position in water cylindrical phantom (a) center of water. (b) Point source offset from center to X-axis (-5 cm). (c) Point source offset from center to X-axis (+5 cm). (d) Point source offset from center to Y-axis (-5 cm). (e) Point source offset from center to Y-axis (+5 cm). (f) Point source offset from center to Z-axis (-5 cm). (g) Point source offset from center to Z-axis (+5 cm).

Therefore, 6keV sub-window with a 20% main-energy was possible energy windows setting for the TEW method in Sm-153.

4.4.5 Discussion

Previous study [82] has assessed the TEW method for Sm-153 SPECT data. But until now, no study has compared the fraction of scattered photons of Sm-153 with varying main- and sub-energy windows for the implementation of the TEW method. The scattered photons are

Window width	Position (x,y,z)	Simulation(Sca/Tot)	TEW (Sca/Tot)			Difference (%)		
			2keV	a 4keV	6keV	2keV	4keV	6keV
20%	(0,0,0)	36	51.39	50.14	49.04	29.95	-2.50	-2.25
	(-5,0,0)	37	51.79	50.24	48.94	28.56	-3.09	-2.65
	(5,0,0)	37	47.71	46.19	45.53	22.45	-3.30	-1.44
	(0,-5,0)	31	43.35	40.99	40.38	28.49	-5.75	-1.52
	(0,5,0)	31	47.85	46.50	44.28	35.21	-2.90	-5.02
	(0,0,-5)	47	52.41	52.93	51.68	10.32	0.98	-2.42
	(0,0,5)	20	38.86	36.57	36.52	48.54	-6.27	-0.15
15%	(0,0,0)	33	46.46	44.83	43.72	28.98	-3.65	-2.55
	(-5,0,0)	34	49.29	46.50	44.83	31.01	-6.00	-3.72
	(5,0,0)	34	50.99	45.74	43.15	33.31	-11.47	-6.00
	(0,-5,0)	28	45.70	41.03	38.09	38.73	-11.39	-7.70
	(0,5,0)	28	45.70	42.47	40.84	38.73	-7.59	-4.01
	(0,0,-5)	45	44.86	51.40	49.65	-0.30	12.71	-3.51
	(0,0,5)	17	57.58	36.22	33.74	70.48	-58.99	-7.35
10%	(0,0,0)	29	69.02	59.96	114.79	57.98	-15.11	47.77
	(-5,0,0)	29.1	68.34	88.98	106.79	57.42	23.19	16.68
	(5,0,0)	29.5	68.39	90.59	107.51	56.87	24.50	15.74
	(0,-5,0)	23.6	66.37	86.68	101.14	64.44	23.43	14.30
	(0,5,0)	24.5	65.01	85.17	100.72	62.31	23.68	15.43
	(0,0,-5)	40.7	73.10	97.20	118.73	44.32	24.80	18.13
	(0,0,5)	14.5	61.58	77.95	89.87	76.45	21.00	13.26

Table 4.14: Comparison of simulated scatter fraction (%) and scatter fraction estimated using TEW scatter correction method for different main- and sub-windows.

Figure 4.22: The reconstructed images of simulated Jaszczak; (a) without the TEW image, (b) Scatter image, (c) with the TEW image.

a major factor degrade resolution image and image contrast [**?**]. The resolution is mostly expressed as the full width at half of maximum (FWHM) of the PSF. A smaller FWHM imply the better quality of the image. The FWHM and contrast were utilized to assess the effect of the processing method on image quality. The choice of optimal energy window in TEW method has a key role which appearing the lowest scatter fraction. We have determined the optimal windows that it display the similar scatter fraction calculated by means of simulation and TEW method. Different scatter fractions were obtained for each source location. There was a smaller difference with 20% main-energy window and 6 keV secondary energy window. By looking at the Table 4, it is obvious that the calculated the spatial resolution was improved with TEW method. As shown in Figure 5, the 20% main-energy window with 6 keV sub-energy windows produce the better contrast when using the TEW correction. The simplicity of this method

Source position (x,y,z)	Without TEW)		With TEW)	
	X FWHM(mm)	Y FHM(mm)	X FWHM(mm)	Y FWHM(mm)
(0,0,0)	9.73	9.51	3.47	3.47
(-5,0,0)	9.65	9.42	7.95	7.24
(5,0,0)	9.62	9.51	7.08	7.21
(0,-5,0)	9.47	9.29	7.00	7.24
(0,5,0)	9.60	9.29	7.52	7.79
(0,0,-5)	12.19	11.98	8.90	8.52
(0,0,5)	7.68	7.46	6.67	5.10

Table 4.15: FWHM of the point source images of Figure 3
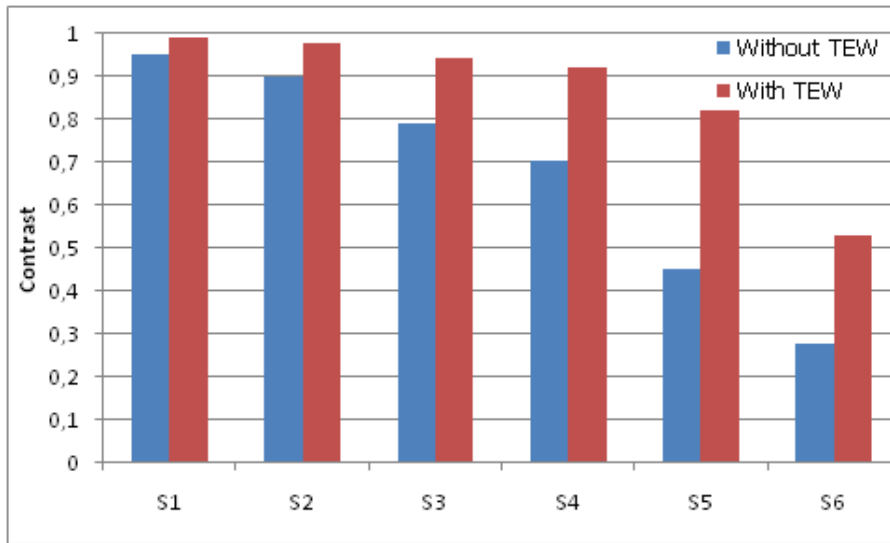
Figure 4.23: Calculated contrast of six hot spheres (S1, S2, S3, S4, S5 and S6) with different diameters: (31.8, 25.4, 15.9, 19.1, 12.7 and 9.5mm) respectively.

making it feasible in Clinical study. However, the estimation of scattered photons cannot be determined experimentally, with the help of Monte Carlo simulation, accurate assessment of the scattered photon fractions inside photo-peak window can be made.

4.4.6 Conclusion

In this study, we used the Monte Carlo SIMIND code with triple energy window scatter correction method to correct the scatter events detected in photo peak window for Sm-153. The results indicate that, it is better to use 20% main photo-peak window with 6 keV sub- windows when TEW method is applied.

General conclusion

The results from the Monte Carlo simulation indicate that this technique can be useful for determination and evaluation of imaging parameter because of its capability to differentiate the events into separate components. Important parameters, such as the scatter-to-total ratio and primary-to-total ratio, can then be determined and serve as an aid when developing correction methods for scatter and septal penetration. The SIMIND Monte Carlo code used in this work includes complete modeling of collimator interactions, which is essential when higher energy photon emitters are simulated. The following conclusions can be drawn from this thesis: We have evaluated the imaging parameters for I 131 using Monte Carlo simulation. We showed that, in I-131 SPECT, the collimator scatter and penetration are significant and our results demonstrates that, the small acceptance angle has a major effect on the image quality in I 131 SPECT imaging. We used Monte Carlo simulation to perform detailed characterization of spatial distributions of photons that undergo scatter and septal penetration in Lu-177 imaging. This characterization will be useful for development of new techniques and evaluation of existing method that correct for scatter and penetration in Lu-177 SPECT imaging. The obtained optimal ME collimator and optimal 20% energy window have the potential to improve the image contrast of Lu-177 images. Subsequently, high quality Lu-177 images can provide reliable estimate of the Lu-177 activity distribution.

Bibliography

[1] LAZARO D, .Validation de la plate-forme de simulation GATE en Tomographie d'Émission Monophotonique et application au développement d'un algorithme de reconstruction 3D complète. Ecole Doctrorale des Sciences Fondamentales 2003.

[2] LAZARO D, .Etude dune nouvelle architecture de gamma caméra à base de semi-conducteurs CdZnTe /CdTe. Ecole Doctorale D'angers 2007.

[3] Van Holen R, Staelens S, Vandenberghe S. .SPECT imaging of high energy isotopes and isotopes with high energy contaminants with rotating slat collimators.Med Phys. 2009 Sep;36(9):4257-67.

[4] Pandey AK, Sharma SK, Karunanithi S, Kumar P, Bal C, Kumar R. Characterization of parallel-hole collimator using Monte Carlo Simulation.Indian J Nucl Med. 2015 Apr-Jun;30(2):128-34.

[5] Ljungberg M. The SIMIND Monte Carlo program home page. Available from: https://www.msf.lu.se/forskning/the-simindmonte-carlo-program. [Last accessed on 2020 Feb]

[6] Asmi H, Bentayeb F, Bouzekraoui Y, Bonutti F. Optimization of scatter correction method in samarium-153 single-photon emission computed tomography using triple-energy window: A monte carlo simulation study. Indian J Nucl Med 2020;35:210-215.

[7] Bouzekraoui Y, BENTAYEB F, Asmi H and Bonutti F. Energy window optimization for Y-90 Bremsstrahlung SPECT imaging: A Monte Carlo simulation study. Iranian J Med Phys 2020.

[8] Asmi H, Bentayeb F, Bouzekraoui Y, Bonutti F. Evaluation of acceptance angle in iodine131 single photon emission computed tomography imaging with Monte Carlo simulation. Indian J Nucl Med 2019;34:246.

[9] Asmi H, Bentayeb F, Bouzekraoui Y, Bonutti F, Douama S. Energy Window and Collimator Optimization in Lutetium-177 Single-photon Emission Computed Tomography Imaging using Monte Carlo Simulation.Indian J Nucl Med. 2020 Jan-Mar;35(1):36-39.

[10] Bouzekraoui Y, Bentayeb F, Asmi H, Bonutti F.Energy Window and Contrast Optimization for Single-photon Emission Computed Tomography Bremsstrahlung Imaging with Yttrium-90.Indian J Nucl Med. 2019 Apr-Jun;34(2):125-128.

[11] Bouzekraoui Y, BENTAYEB F, Asmi H and Bonutti F. Determination of the Energy Windows for the Triple Energy Window Scatter Correction Method in Gadolinium-159 Single Photon Emission Computed Tomography Using Monte Carlo Simulation. Iranian J Med Phys. 2019;16:405-409.

[12] Bouzekraoui Y, Bentayeb F, Asmi H, Bonutti F.Comparison of Image Quality of Different Radionuclides Technetium-99m, Samarium-153, and Iodine-123.Indian J Nucl Med. 2019 Jul-Sep;34(3):201-204.

[13] Upadhyay B, Mo J, Beadsmoore C, Marshall T, Toms A, and Buscombe J.Technetium-99m Methylene Diphosphonate Single-photon Emission Computed Tomography/Computed Tomography of the Foot and Ankle. World J Nucl Med. 2017 Apr-Jun; 16(2): 88100.

[14] Anger, H. O. (1964). "Scintillation camera with multichannel collimators." Journal of Nuclear Medicine(5): 515-531.

[15] Audenhaege KV, Holen RV , Vandenberghe S, and Vanhove C. Review of SPECT collimator selection, optimization, and fabrication for clinical and preclinical imaging. Med. Phys. 42 (8), August 2015.

[16] Esquerré J.P., Danet B. and Gantet P. (1996). Évolution des gamma-caméras. Revue de lAcomen 2: 175-181.

[17] Moretti J.L. and Roussi A. (1993). Contrôle de qualité des gamma-caméras planaires et tomographiques. RBM 15 : 375-85.

[18] Huang CW, Hsu SW, Chang YT, Huang SH, Huang YC, Cerebral Perfusion Insufficiency and Relationships with Cognitive Deficits in Alzheimers Disease: A Multiparametric Neuroimaging Study Scientific Reports 2018;8:1541.

[19] Cagnac B and Pebay-Peyroula J.C. (1971). Physique atomique Introduction à la physique quantique et structure de lédifice atomique. Dunod, Paris.

[20] Gilland D.R., Tsui B.M.W., McCartney W.H., Perry J.R. and Berg J. (1988). Determination of the optimum filter function dor SPECT imaging. J. Nucl. Med. 29: 643-650.

[21] Gilland D.R., Jaszczak R.J., Greer K.L. and Coleman R.E. (1991). Quantitative SPECT reconstruction of iodine-123 data. J. Nucl. Med. 32: 527-533.

[22] Shepp L.A. and Vardi Y. (1982). Maximum Likelihood Reconstruction for Emission Tomography. IEEE Trans. Med. Imaging MI-1 :113-121.

[23] Lange K. And Carson R. (1984). EM reconstruction algorithms for emission and transmission tomography. J. Comput. Assist. Tomogr. 8: 306-316.

[24] Miller, M. I., D. L. Snyder and M. T.R. (1985). "Maximum-Likelihood reconstruction for Single-Photon Emission Computed-Tomography." IEEE Transactions on Nuclear Science: 769-778.

[25] Hudson H.M. and Larkin R.S. (1994) Accelerated image reconstruction using ordered subsets of projection data. IEEE Tr. Med. Imaging 13: 601-609.

[26] "Analytic and iterative reconstruction algorithms in SPECT." Journal of Nuclear Medicine 43(10): 1343-1358.

[27] Lange, K. (1990). "Convergence of Em Image-Reconstruction Algorithms with Gibbs Smoothing." IEEE Transactions on Medical Imaging 9(4): 439-446

[28] Lalush, D. S. and B. M. W. Tsui (1992). "Simulation Evaluation of Gibbs Prior Distributions for Use in Maximum a-Posteriori Spect Reconstructions." IEEE Transactions on Medical Imaging 11(2): 267-275.

[29] Hebert, T. J. and R. Leahy (1992). "Statistic-Based Map Image-Reconstruction from Poisson Data Using Gibbs Priors." IEEE Transactions on Signal Processing 40(9): 2290-2303.

[30] Alenius, S. and U. Ruotsalainen (2002). "Generalization of median root prior reconstruction." IEEE Transactions on Medical Imaging 21(11): 1413-1420.

[31] Alenius, S. and U. Ruotsalainen (1997). "Bayesian image reconstruction for emission tomography based on median root prior." European Journal of Nuclear Medicine 24(3): 258- 265.

[32] Alenius, S., U. Ruotsalainen and J. Astola (1998). "Using local median as the location of the prior distribution in iterative emission tomography image reconstruction." IEEE Transactions on Nuclear Science 45(6): 3097-3104.

[33] Seret, A. and M. Defrise (2004). "la tomoscintigraphie avec gamma-camera commerciale munie d'un collimateur sténopé: aspects techniques et méthodes de reconstruction." Médecine nucléaire - Imagerie fonctionnelle et métabilique 28: 493-506.

[34] Ferreira T, Rasband W. Image J Program. Available from: https://imagej.nih.gov/ij/download.html. [Last accessed on 2018 Aug].

[35] Jaszczak RJ, Greer KL, Floyd CE Jr., Harris CC, Coleman RE. Improved SPECT quantification using compensation for scattered photons. J Nucl Med 1984; 25:893900.

[36] Ichihara T, Ogawa K, Motomura N, Kubo A, Hashimoto S. Compton scatter compensation using the triple-energy window method for single- and dual-isotope SPECT. J Nucl Med 1993; 34:22162221

[37] Ogawa K, Harata Y, Ichihara T, Kubo A, Hashimoto S. A practical method for position-dependent Compton-scatter correction in single photon emission CT. IEEE Trans Med Imaging 1991; 10:408412.

[38] Evaluation of six scatter correction methods based on spectral analysis in (99m)Tc SPECT imaging using SIMIND Monte Carlo simulation.

[39] Ljungberg M, King MA, Hademenos GJ, Strand SE. Comparison of four scatter correction methods using Monte Carlo simulated source distributions. J Nucl Med 1994; 35:143151.

[40] De Nijs R, Holm S, Thomsen G, Ziebell M, Svarer C. Experimental determination of the weighting factor for the energy window subtractionbased downscatter correction for I-123 in brain SPECT studies. J Med Phys 2010; 35:215222

[41] Pretorius PH, van Rensburg AJ, van Aswegen A, Lötter MG, Serfontein et.al. The channel ratio method of scatter correction for radionuclide image quantitation . J Nucl Med. 1993 Feb;34(2):330-5.

[42] van der Have F, Ivashchenko O, Goorden MC, Ramakers RM, Beekman FJ. High-resolution clustered pinhole (131) Iodine SPECT imaging in mice. Nucl Med Biol 2016;43:506-11.

[43] Kocher DC. Radioactive Decay Data Tables: A Handbook of Decay Data for Application to Radiation Dosimetry and Radiological Assessment. DOE/TIC-11026. Springfeld, VA: National Technical Information Service, U.S. Department of Energy; 1981. p. 133-4.

[44] Autret D, Bitar A, Ferrer L, Lisbona A, Bardiès M. Monte Carlo modeling of gamma cameras for I-131 imaging in targeted radiotherapy. Cancer Biother Radiopharm 2005;20:77-84.

[45] Dewaraja YK, Ljungberg M, Koral KF. Characterization of scatter and penetration using Monte Carlo simulation in 131I imaging. J Nucl Med 2000;41:123-30.

[46] Rault E, Vandenberghe S, Van Holen R, De Beenhouwer J, Staelens S, Lemahieu I, et al. Comparison of image quality of different iodine isotopes (I-123, I-124, and I-131). Cancer Biother Radiopharm 2007;22:423-30.

[47] Kojima A, Gotoh K, Shimamoto M, Hasegawa K, Okada S. Iodine-131 imaging using 284 keV photons with a small animal CZT-SPECT system dedicated to low-medium-energy photon detection. Ann Nucl Med 2016;30:169-75.

[48] Lee YS, Kim JS, Kim KM, Lim SM, Hee-Joung K. Determination of energy windows for the triple energy window scatter correction method in I-131 on a Siemens SYMBIA gamma camera: A GATE simulation study. Sissa Medialab 2015;10:1-8.

[49] Dewaraja Y, Li J, Koral K. Quantitative 131I SPECT with triple energy window Compton scatter correction. IEEE Trans Nucl Sci 1998;45:3109.

[50] Bong JK, Son HK, Lee JD, Kim HJ. Improved scatter correction for SPECT images: A Monte Carlo study. IEEE Trans Nucl Sci 2005;52:1263.

[51] Cao Z, Qian L. A triple-head SPECT system with parallel-hole collimators of different acceptance angles. Int J Med Inform 1997;46:145-57.

[52] Paganelli G, Sansovini M, Ambrosetti A, Severi S, Monti M, Scarpi E, et al. 177 ludotaoctreotate radionuclide therapy of advanced gastrointestinal neuroendocrine tumors: Results from a phase II study. Eur J Nucl Med Mol Imaging 2014;41:184551.

[53] Romer A, Seiler D, Marincek N, Brunner P, Koller MT, Ng QK, et al. Somatostatinbased radiopeptide therapy with [177LuDOTA]TOC versus [90YDOTA]TOC in neuroendocrine tumours. Eur J Nucl Med Mol Imaging 2014;41:21422.

[54] Ezziddin S, Khalaf F, Vanezi M, Haslerud T, Mayer K, Al Zreiqat A, et al. Outcome of peptide receptor radionuclide therapy with 177Luoctreotate in advanced grade 1/2 pancreatic neuroendocrine tumours. Eur J Nucl Med Mol Imaging 2014;41:92533.

[55] van der Zwan WA, Bodei L, MuellerBrand J, de Herder WW, Kvols LK, Kwekkeboom DJ. GEPNETs update: Radionuclide therapy in neuroendocrine tumors. Eur J Endocrinol 2015;172:R18.

[56] Ilan E, Sandström M, Wassberg C, Sundin A, GarskeRomán U, Eriksson B, et al. Dose response of pancreatic neuroendocrine tumors treated with peptide receptor radionuclide therapy using 177LuDOTATATE. J Nucl Med 2015;56:17782.

[57] Bodei L, Cremonesi M, Grana CM, Fazio N, Iodice S, Baio SM, et al. Peptide receptor radionuclide therapy with źLuDOTATATE: The IEO phase III study. Eur J Nucl Med Mol Imaging 2011;38:212535.

[58] He B, Nikolopoulou A, Osborne J, Vallabhajosula S, Vallabhajosula S, Goldsmith S. Quantitative SPECT imaging with Lu 177: A physical phantom evaluation. J Nucl Med 2012;53:12407.

[59] de Nijs R, Lagerburg V, Klausen TL, Holm S. Improving quantitative dosimetry in (177) LuDOTATATE SPECT by energy windowbased scatter corrections. Nucl Med Commun 2014;35:52233.

[60] Mezzenga E, DErrico V, DArienzo M, Strigari L, Panagiota K, Matteucci F, et al. Quantitative accuracy of 177Lu SPECT imaging for molecular radiotherapy. PLoS One 2017;12:e0182888.

[61] Stigbrand T et al 2008 Targeted Radionuclide Tumor Therapy (New York: Springer)

[62] Nag S et al. Recommendations for radioembolization of hepatic malignancies using yttrium-90 microspherebrachytherapy: a consensus panel report from the Radioembolization Brachytherapy Oncology Consortium Int.J. Radiat. Oncol 2007;68:1323.

[63] Rong. X.. Frey. E.C. A collimator optimization method for quantitative imaging: application to Y-90 bremsstrahlung SPECT. Med. Phys2013;40:082504.

[64] Rong. X..Ghaly. M.. Frey. E.C. Optimization of energy window for 90Ybremsstrahlung SPECT imaging for detection tasks using the ideal observerwith model-mismatch. Med. Phys2013;40:062502.

[65] Rong.X.. Du.Y.. Frey. E.C. A method for energy window optimization for quantitative tasks that includes the effects of model-mismatch on bias: application to Y-90 bremsstrahlung SPECT imaging. Phys. Med. Biol 2012 ; 57:3711.

[66] Heard S. Flux G D. Guy M J and Ott R J. Photon source kernels for Monte Carlo simulation of bremsstrahlung imaging Eur. J. Nucl. Med 2004;31:S403

[67] Shen S.Denardo G L. Yuan A N. Denardo D A and Denardo S J. Planar gamma-camera imaging and quantitationof Y-90 bremsstrahlung J. Nucl. Med 1994;35:13819.

[68] Yue J. Mauxion T. Reyes DK. Lodge MA. Hobbs RF et al .Comparison of quantitative Y-90 SPECT and non-time-of-flight PET imaging in post-therapy radioembolization of liver cancer.Med Phys. 2016 Oct;43(10):5779.

[69] Elschot M. Vermolen B. Lam M. de Keizer B. Bosch MVD et al. Quantitative comparison of PET and SPECT for imaging the yttrium-90 microsphere distribution after liver radioembolization. J Nucl Med May 2012;53:103.

[70] De Vries DJ. Moore S. Approximation of hexagonal holes by square holes in Monte Carlo simulation of gamma-camera collimation. IEEE TransNucl Sci. 2002;49(5):2186-95.

[71] Yeong CH. Abdullah BJ. Ng KH. Chung LY. Goh KL. Sarji SA. et al. Production and first use of 153SmCl3-ion exchange resin capsule formulation for assessing gastrointestinal motility. Appl Radiat Isot. 2012;70:450-5.

[72] Iagaru AH. Mittra E. Colletti PM. and Jadvar H. Bone-Targeted Imaging and Radionuclide Therapy in Prostate Cancer. J Nucl Med. 2016;57:19S-24S.

[73] Zohreh Naseri. R. Jalilian A. Nemati Kharat A. Bahrami-Samani A and Ghannadi-Maragheh M. Production. quality control and biological evaluation of 153Sm-TTHMP as a possible bone palliation agent. Iran J Nucl Med. 2011;19:60-8.

[74] Ramachandran K. Kathiresan. Begum B and Rangarajan. Comparison of Tc-99m MDP and Sm-153 EDTMP bone scan. Indian J Nuc Med 2011;26:163-4.

[75] Hashikin NA. Yeong CH. Abdullah BJ. Ng KH. Chung LY. Dahalan R et al. Neutron Activated Samarium-153 Microparticles for Transarterial Radioembolization of Liver Tumour with Post Procedure Imaging Capabilities. PLoS One. 2015;10:e0138106

[76] Lee YS. Kim JS. Kim KM. Lim SM and Kim HJ. Determination of energy windows for the triple energy window scatter correction method in I-131 on a Siemens SYMBIA gamma camera: a GATE simulation study. J Inst. 2015;15:10:1-8.

[77] Takayama T. Ichihara T. Motomura N and Ogawa K. Determination of Energy Window Width and Position for Scintigraphic Imaging Using Different Energy Resolution Detection with the 'Triple Energy Window (TEW) Scatter Compensation Method IEEE. Kaku Igaku. 1998;35:51-9.

[78] Changizi V. Takavar A. Babakhani A and Sohrabi M. Scatter correction for heart SPECT images using TEW method. J Appl Clin Med Phys. 2008;9:136-40.

[79] DewarajaY.K. Li J. and Koral K. Quantitative 131I SPECT with triple energy window Compton scatter correction. IEEE Trans Nucl Sc. 1998;45:3109 14.

[80] Fujioka H. Inoue T. Ishimaru Y. Akamune A. Murase K. Tanada S and al. Compton scatter correction using the triple energy window (TEW) method in conventional single photon emission computed tomography without TEW acquisition hardware. Ka Iga.1997; 34:251-8.

[81] Ogawa K. Simulation study of triple-energy-window scatter correction in combined TI-201. Tc-99m SPECT. Ann Nucl Med. 1994; 8:277-81.

[82] Asgari A. Ashoor M. Sohrabpour M. et al. Evaluation of various energy windows at different radionuclides for scatter and attenuation correction in nuclear medicine. Ann Nucl Med. 2015;29:375-83.

[83] Kim KM. Varrone A. Watabe H. Shidahara M. Fujita M. Innis RB et al. Contribution of scatter and attenuation compensation to SPECT images of nonuniformly distributed brain activities. J Nucl Med. 2003;44:512-9.

[84] Ogawa K. Harata Y. Ichihara T. Kubo A. Hashimoto S. A practical method for position-dependent Compton-scatter correction in single photon emission CT. IEEE Trans Med Imaging. 1991;10:408-12.

[85] Bong JK. Son HK . Lee JD and Kim HJ. Improved scatter correction for SPECT images: A Monte Carlo study. IEEE Trans Nucl Sc. 2005; 52:1263-70.

[86] Toossi BMT. Islamian PJ. Momennezhad M. Ljungberg M and Naseri SH. SIMIND Monte Carlo simulation of a single photon emission CT. J Med Phys. 2010;35:42-7.

[87] Azarm A. Islamian JP. Mahmoudian B and Gharepapagh E. The Effect of Parallel-hole Collimator Material on Image and Functional Parameters in SPECT Imaging : A SIMIND Monte Carlo Study. World J Nucl Med. 2015;14:160-4.

[88] Vicente EM. Lodge MA. Rowe SP. Wahl RL and Frey EC. Simplifying volumes-of-interest (VOIs) definition in quantitative SPECT : Beyond manual definition of 3D whole-organ VOIs. Med Phys. 2017;44:1707-17.

[89] Rafati M. Rouhani H. Bitarafan-Rajabi A. Noori-Asl M and al. Assessment of the scatter correction procedures in single photon emission computed tomography imaging using simulation and clinical study J Cancer Res Ther. 2017;13:936-942.

[90] SHA ALehyani. Application of single photon emission computed tomography (SPECT) parameters for bone scintigraphy. J King Saud Univ - Sc. 2009;21:109-17

[91] Asl MN. Sadremomtaz A and Bitarafan-Rajabi A. Evaluation of six scatter correction methods based on spectral analysis in Tc SPECT imaging using SIMIND Monte Carlo simulation. J Med Phys. 2013 Oct;38:189-97.

[92] Dewaraja YK. Ljungberg M and Koral KF. Characterization of scatter and penetration using Monte Carlo simulation in 131I imaging. J Nucl Med. 2000;41:123-30

ROYAUME DU MAROC

Université Mohammed V
- RABAT -

جامعة محمد الخامس
– الرباط –

Faculté des sciences
كلية العلوم

CENTRE D'ETUDES DOCTORALES - SCIENCES ET TECHNOLOGIES

Résumé

Les simulations de Monte Carlo sont actuellement considérées en imagerie de médecine nucléaire comme un outil pour concevoir et optimiser la caméra à scintillation et les systèmes SPECT, ainsi que pour évaluer algorithmes de reconstruction et méthodes de correction pour dégrader les effets physiques. Parmi les de nombreux simulateurs disponibles, aucun d'entre eux n'est considéré comme un standard en imagerie médicale nucléaire. Dans cette thèse, nous avons utilisé le code de simulation de Monte Carlo, SIMIND, qui décrit une caméra SPECT standard et peut facilement être modifié pour presque n'importe quel type de calcul rencontré en imagerie SPECT. SIMIND a été validé dans SPECT en modélisant des gamma caméras, en comparant les résultats obtenus avec des simulations SIMIND avec des données expérimentales. SIMIND comprend une modélisation complète des interactions des collimateurs, ce qui est essentiel lorsque des émetteurs de photons de plus haute énergie sont simulés. Notre objectif dans ce travail de thèse était d'évaluer et de déterminer les paramètres d'imagerie optimaux en imagerie SPECT, et également d'évaluer la méthode TEW, au moyen de la simulation de Monte Carlo. Une méthode largement utilisée pour la correction de la diffusion est la soustraction d'images formées à l'aide de fenêtres d'énergie dans la région des photopointes. Les paramètres utilisés pour la comparaison des différents paramètres de fenêtre et collimateurs incluent; résolution spatiale, sensibilité, contraste de l'image, rapports diffusion / total (STR). Nous avons évalué les paramètres d'imagerie pour l'I-131 en utilisant la simulation de Monte Carlo. Nous avons démontré que, dans I-131 SPECT, la diffusion et la pénétration du collimateur sont significatives et nos résultats montrent que, le petit angle d'acceptation a un effet majeur sur la qualité de l'image en imagerie I-131 SPECT. En outre, un certain nombre de paramètres de fenêtre d'énergie et de collimateur différents pour les isotopes I-131, Lu-177, Y-90 sont étudiés en utilisant des simulations de Monte Carlo avec le code SIMIND. De plus, nous évaluons les fractions de photons diffusés et déterminons les fenêtres optimales de sous-énergie et d'énergie principale pour la mise en œuvre de la méthode de correction TEW en imagerie Sm-153.

Mots-clés: tomographie par émission monophotonique (SPECT), imagerie nucléaire, Monte Simulation de Carlo, SIMIND, sensibilité, résolution spatiale, photon diffusé

Abstract

Monte Carlo simulations are currently considered in nuclear medicine imaging as a powerful tool to design and optimize the scintillation camera and SPECT systems, and also to assess reconstruction algorithms and correction methods for degrading physical effects. Among the many simulators available, none of them is considered as a standard in nuclear medical imaging. In this thesis we have used the Monte Carlo simulation code, SIMIND, which describes a standard SPECT camera and can easily be modified for almost any type of calculation encountered in SPECT imaging. SIMIND was validated in SPECT by modeling gamma cameras, by comparing the results obtained with SIMIND simulations with experimental data. SIMIND includes complete modeling of collimator interactions, which is essential when higher energy photon emitters are simulated. Our objective in this thesis work was to evaluate and determine the optimal imaging parameters in SPECT imaging, and also evaluate of TEW method, by the means of Monte Carlo simulation. A widely used method for scatter correction is subtraction of images formed using energy windows in the region of the photopeaks. Parameters used for comparison of the different window settings and collimators include; spatial resolution, sensitivity, image contrast, scatter to total ratios (STR). We have evaluated the imaging parameters for I-131 using Monte Carlo simulation. We demonstrated that, in I-131 SPECT, the collimator scatter and penetration are significant and our results show that, the small acceptance angle has a major effect on the image quality in I-131 SPECT imaging. In addition, a number of different energy window settings and collimator for the isotopes I-131, Lu-177, Y-90 are investigated using Monte Carlo simulations with the code SIMIND. Also, we assess the scattered photon fractions and determined the optimal sub- and main-energy windows for the implementation of TEW correction method in Sm-153 imaging.

Keywords: *single-photon emission computed tomography (SPECT), nuclear imaging, Monte Carlo simulation, SIMIND, sensitivity, spatial resolution, scattered photon*

Année Universitaire : 2019-2020